

POLITECNICO DI TORINO

**Corso di Laurea Magistrale in
INGEGNERIA ENERGETICA e NUCLEARE**



MSc thesis

**Measurements and Monte Carlo simulations with
miniature neutron detectors for flux characterization in
the SUR-100 zero power reactor**

Supervisors

Prof. Sandra Dulla

Dr. Vincent Pierre Lamirand

Candidate

Edoardo Luciano Brunetto

October 2020

This page is intentionally left blank.

Abstract

An advanced neutron detection system for highly localized in-core measurements developed in the Laboratory for Reactor Physics and System Behaviour (LRS) at École polytechnique fédérale de Lausanne (EPFL) it is used to characterize the neutron flux of the SUR 100 zero-power reactor of the Institut für Kernenergetik und Energiesysteme (IKE) operated at the University of Stuttgart. The small size of its experimental channels requires the use of miniature detectors for a proper characterization of the neutron flux profiles, not achievable with conventional detection techniques.

An experimental campaign is carried out in the IKE laboratory by means of an academic collaboration established with the EPFL-LRS. Miniature neutron detectors are disposed in different arrangements in order to achieve high spatial resolution measurements of the neutron flux profiles in the experimental channels of the reactor. The detection system is extensively tested in the EPFL facilities as a preparatory activity for the experimental campaign.

Part of the work is dedicated to adapt an existing Monte Carlo model of the reactor to the three-dimensional neutron transport code Serpent2. Neutron transport simulations have been run both before and after the campaign, to prepare the experimental activities and to verify their results with comparisons against the computations.

A good level of agreement is found between computational and experimental results, demonstrating the goodness of the converted Monte Carlo model and the excellent acquisition capabilities on small scale of the miniature detectors. In light of the obtained results, an accurate characterization of the thermal neutron flux profiles within the experimental channels of the SUR 100 reactor is achieved.

Acknowledgements

This page is dedicated to thank all the people who have supported me in writing this thesis, which has been carried out simultaneously with the outbreak and spread of the COVID-19 pandemic. Without the help of these people, this work would not have been possible.

I would first like to express my deepest appreciation to my EPFL supervisor, Dr. Vincent Lamirand, to whom I extend my gratitude for his invaluable guidance throughout this project. I want to thank you for your support and for all the enriching opportunities I was given to carry out this thesis.

A great thank to my supervisor at Politecnico di Torino, Prof. Sandra Dulla, who has always been available in providing help when needed and without whom this thesis abroad would not have been feasible.

I would like to acknowledge all the people at the Laboratory for Reactor Physics and Systems Behaviour at EPFL for their wonderful collaboration. The time spent with you in and out of the office has been very precious to me. A special thank goes to Fanny Vitullo, who provided me with encouragement and patience all along this project. I am deeply indebted with you for your untiring help, but I am sure that a couple of beers will fix it.

I would like to extend my sincere thanks to Prof. Jörg Starflinger and all the people at the Institute of Nuclear Technology and Energy Systems of the University of Stuttgart. Your helpful collaboration was instrumental in the success of the experimental campaign and extremely constructive for my educational growth.

I am extremely grateful to all the friends with whom I shared this path and who provided me help in unimaginable ways. A huge thank to the people I have lived with, to those who gave me a place to stay when I didn't have one and to the good old friends who have been with me for as long as I can recall.

The biggest thanks goes to my family, always supportive in giving me the privilege to pursue my dreams, even when they keep me distant from home. Your unconditional love is what drives me to give my best.

Torino, October 2020

E. L. B.

Ringraziamenti

Questa pagina è volta a ringraziare tutte le persone che mi hanno sostenuto nella stesura di questa tesi, realizzata in concomitanza con lo scoppio e la diffusione della pandemia di COVID-19. Senza il loro sostegno, il compimento di questo lavoro non sarebbe stata possibile.

Vorrei prima di tutto esprimere il mio più profondo apprezzamento al mio relatore all'EPFL, il Dr. Vincent Lamirand, al quale va la mia gratitudine per la preziosa supervisione di questo progetto. Grazie per il suo sostegno e per tutte le opportunità di arricchimento che mi sono state date nel realizzare questa tesi.

Un grande ringraziamento al mio relatore del Politecnico di Torino, la Prof.ssa Sandra Dulla, sempre disponibile a fornire aiuto in caso di necessità e senza la quale questa tesi all'estero non sarebbe stata possibile.

Vorrei ringraziare tutte le persone del Laboratory for Reactor Physics and Systems Behaviour all'EPFL per la loro meravigliosa collaborazione. Il tempo trascorso con voi dentro e fuori dall'ufficio è stato molto prezioso per me. Un ringraziamento speciale va a Fanny Vitullo, che mi ha dato incoraggiamento e supporto durante tutto questo progetto. Mi sento profondamente in debito con te per il tuo instancabile aiuto, ma sono certo che un paio di birre sistemeranno tutto.

Ringrazio di cuore il Prof. Jörg Starflinger e tutte le persone dell'Institute of Nuclear Technology and Energy Systems dell'Università di Stoccarda. La vostra collaborazione è stata determinante per il successo della campagna sperimentale ed estremamente costruttiva per la mia crescita educativa.

Sono estremamente grato a tutti gli amici con cui ho condiviso questo cammino e che mi hanno aiutato in modi inimmaginabili. Un grande ringraziamento alle persone con cui ho vissuto, a coloro che mi hanno dato un posto in cui stare quando non ne avevo uno e ai buoni vecchi amici che mi sono vicini da quando ne ho memoria.

Il ringraziamento più grande va alla mia famiglia, sempre solidale nel darmi il privilegio di inseguire i miei sogni, anche quando questi mi allontanano da casa. Il vostro amore incondizionato è ciò che mi spinge a dare il mio meglio.

Torino, Ottobre 2020

E. L. B.

Contents

Abstract	i
Acknowledgements	ii
Contents	iv
List of Figures	vi
List of Tables	ix
Nomenclature	x
1 Introduction	1
1.1 Design of the SUR 100 reactor	2
1.1.1 Reactor core	3
1.1.2 Neutron source	4
1.1.3 Graphite reflector	4
1.1.4 Inner reactor vessel	5
1.1.5 Control plates	6
1.1.6 Reactor shielding	7
1.1.7 Experimental channels	8
1.1.8 Reactor monitors	9
1.1.9 Cavity beneath the core	9
1.2 Miniature neutron detector description	10
1.2.1 Detection principle	11
1.2.2 Standard signal processing	12
1.3 Scope and outline of the thesis	14
2 Monte Carlo modeling and simulation of the SUR 100 reactor	16
2.1 Description of the Serpent2 model	16
2.1.1 Geometry and materials	16
2.1.2 Model enhancement	17
2.2 Run parameters	19
2.2.1 k-eigenvalue criticality source method	19
2.2.2 Inactive cycles determination	20
2.2.3 Cross section libraries	20
2.2.4 Source rate normalization	22
2.3 Reactor criticality computation	22
2.3.1 Reactivity curve	23
2.3.2 Impact of cross section library on reactivity	24

2.4	Model validation	25
2.4.1	Average thermal flux in the experimental channel I	26
2.4.2	Average thermal flux in the core	27
2.5	In-core flux perturbation analysis	27
2.6	Design simulations for the experimental campaign	28
2.6.1	Neutron thermal flux distribution in experimental channel I	29
2.6.2	Effect of tangential channels on flux distribution in channel I	29
2.6.3	Vertical gradient in thermal neutron flux inside experimental channel I	30
2.6.4	Neutron thermal flux distribution tangential channels	31
3	Testing and characterization of the miniature neutron detection system	33
3.1	Experimental setup	34
3.1.1	Detectors configuration	34
3.1.2	Read-out electronics	35
3.2	Low Threshold curves	38
3.3	Linearity response in CROCUS	39
3.4	Shutdown transient acquisition	39
3.5	Calibration in the CARROUSEL facility	40
4	SUR 100 experimental campaign	41
4.1	Aim of the campaign	41
4.2	Experimental setup	42
4.3	Preliminary verifications	43
4.4	Neutron thermal flux profile along channel I	44
4.4.1	Profile measurement	45
4.4.2	Comparison with simulations	46
4.4.3	Comparison with activation profile	47
4.5	Neutron thermal flux profile along channel II	50
4.6	Vertical gradient in thermal neutron flux across channel I diameter	51
4.7	Radial gradient in thermal neutron flux across channel II diameter	52
4.8	Control plate calibration	53
4.8.1	Reactor dynamics	54
4.8.2	Reactivity computation	54
5	Conclusions	57
	Appendices	59
A	Radiation safety assessment	60
A.1	Simulation setup	60
A.2	Neutrons dose rate	61
A.3	Gamma dose rate	62
A.4	Results	63
B	Serpent2 SUR 100 model	65
	Bibliography	69

List of Figures

1.1	Pictures of the reactor hall in the 60's (left) [1] and nowadays (right).	2
1.2	Vertical (left) and horizontal (right) cuts of the SUR 100 reactor [1].	3
1.3	Scheme of the core dimensions (left) and its components (right) [1].	4
1.4	Schematics of the inner (left) and outer (right) components of the graphite reflector [1].	5
1.5	Side and bottom view of the inner reactor vessel [1].	6
1.6	Picture of a control plate (left) and scheme of its drive mechanism (right) [1]. . .	6
1.7	Scheme of lead shielding and "thermal column".	7
1.8	Vertical cut highlighting the LUPOLEN shielding (left) and picture of its composition (right) [1].	8
1.9	Depiction of four out of the five experimental channels of SUR 100.	9
1.10	Picture of the three detectors of SUR100 [1].	10
1.11	Horizontal cut of SUR 100 at the level of the detector housing [1].	10
1.12	Picture of the cavity beneath the core [1]	10
1.13	Picture of the miniature fiber detector. As the protective Aluminum cap is removed, the scintillator screen is visible (in white).	11
1.14	Scheme of the front-end of the detector.	11
1.15	Cross section of the (n, α) reaction for ${}^6\text{LiF}$ according to the ENDF/B-VII.0 library [9].	11
1.16	Schematic of a standard read-out electronics for miniature fiber-coupled detector. In correspondance of the main components are reported the respective output signals.	12
1.17	Scheme of an Avalanche photodiode [12].	13
1.18	Picture of a Silicon Photomultiplier from Hamamatsu [13]	13
1.19	Example of output signals from the preamplifier in persistence mode. The scales are 1.00 V/div and 20 ns/div.	13
1.20	Example of output signals from the first discriminator (red) and from the amplifier (black).	14
2.1	Vertical cuts through the core obtained with the Serpent2 model.	17
2.2	Horizontal cut through the reactor with focus on the core zone.	18
2.3	Vertical cut of SUR 100 with the added concrete shielding (left) and example of movement of the lower core sections and the control plates (right).	18
2.4	Source distribution convergence study with 10^4 neutrons per cycle.	21
2.5	Source distribution convergence study with $2 \cdot 10^4$ neutrons per cycle.	21
2.6	Effect of the inclusion of Thermal Scattering Libraries on the reactivity of SUR 100.	22
2.7	Difference in reactivity arising from not including Thermal Scattering Libraries.	22
2.8	Scheme of the core start-up procedure.	23

2.9	Reactivity of the system as a function of the height of CP2.	24
2.10	Comparison among different cross section libraries in reactivity computations. .	25
2.11	(a): Average thermal flux in channel I. (b): Depiction of the virtual detector used for the calculation.	26
2.12	(a): Average thermal flux in the reactor core. (b): Depiction of the virtual detector used for the calculation.	27
2.13	Thermal flux map of the core region with the control plates in the criticality position.	28
2.14	Relative differences in flux caused by the movement of control plate 2.	28
2.15	Radial distribution of thermal neutron flux in the experimental channel I. Statistical error on the computed data is below 1% in the center of the core.	29
2.16	Assessment on the perturbative effect of the tangential channels on the thermal neutron flux distribution along channel I. Statistical error on the computed data is below 1% in the center of the core.	30
2.17	Schematic of the modeling of the smeared virtual track-length detectors in Serpent2.	30
2.18	Normalized vertical gradients in reaction rates across channel I as computed with Serpent2.	31
2.19	Distribution of thermal neutron fluxes along the tangential channels. The shaded area in the plots represent the statistical uncertainty of the computed values, which is below 1 % in the core center region.	32
3.1	Picture of the CROCUS core with the experimental instrumentation inserted in the NW control tube for the testing of the detection system.	33
3.2	Picture of the front-end of the detector. The scintillator is visible as the aluminum cap is here removed.	35
3.3	Scheme of the aluminum cap.	35
3.4	Scheme of the positioning of the three fibers in the NW control tube of CROCUS.	35
3.5	Scheme of the read-out electronics used for the testing.	36
3.6	Picture of the SiPM aluminum tubes (on the left) connected to the PCBs (on the right).	36
3.7	Preamplifier + First discriminator PCB designed by the technical division of LRS.	37
3.8	Signals in output from different stages of the read-out electronics chain.	37
3.9	LT curves for each of the three detectors used in the testing.	38
3.10	Linearity curves for each of the three detectors used in the testing.	39
3.11	Dynamic measurement of the shutdown transient in CROCUS.	40
4.1	Aluminum positioner used for the experimental campaign in SUR 100.	42
4.2	Different positioning of the detectors inside the experimental channels of SUR 100.	42
4.3	LT curves measured in the SUR 100 reactor.	43
4.4	Linearity curves measured in SUR 100 for the three neutron detectors.	44
4.5	Simplified schemes of the profile measurements inside channel I (left) and channel II (right). The red lines indicate the spatial range in which measurements are performed.	44
4.6	Count rate distribution measured by fiber 1 in experimental channel I.	45
4.7	Symmetry check on the measured count rate profile along channel I.	45
4.8	Comparison of experimental count rates against ${}^6\text{Li}$ reaction rates predicted by simulations along experimental channel I.	46
4.9	Scheme of the holder used for the activation experiment.	47
4.10	Decay path of the Mn-56 nuclides through different excited states of Fe-56 [23].	48
4.11	Comparison of the activation profile with measurements of miniature detector.	48
4.12	Comparison of the simulated results with and without activation holder.	49

4.13	Comparison of the activation profile with Serpent2 computed results.	49
4.14	C/E-1 values for the comparison of the activation profile with Serpent2 computed results.	50
4.15	Comparison between experimental and simulated results for the thermal neutron flux distribution in tangential channel II.	50
4.16	Detectors configuration for the vertical gradient measurement.	51
4.17	Simulated and experimental data for axial reaction rate gradient in experimental channel I.	52
4.18	Detectors configuration for the radial gradient measurement.	52
4.19	Simulated and experimental data for radial reaction rate gradient in experimental channel II.	53
4.20	Counts recorded by fiber 2 during the reactor periods experiment. The detector is maintained in the center of channel II and used as a power monitor.	53
4.21	Linear fitting of the monitor data for the reactivity experiment.	55
4.22	Comparison between simulation and experimental data for the control plate 2 reactivity calibration.	56
A.1	Virtual detectors used for the dose rate assessment.	60
A.2	Horizontal (a) and vertical (b) view of the importance mesh used for the calculations.	61
A.3	Neutron flux distribution around the reactor concrete shielding.	62
A.4	Neutron flux to dose rate conversion factors [26]	62
A.5	Mesh plot for the Gamma dose rate distribution around the shielding of SUR 100.	63
A.6	Dose rate distribution around SUR 100.	64
A.7	Dose rate distribution around SUR 100 compared with legal limits.	64

List of Tables

2.1	Summary table of the experimental data used for the validation of the Serpent2 model. Data are provided by the IKE laboratory.	25
2.2	Default 2 groups energy binning - Serpent2.	26
3.1	Results of the detectors calibration in the CARROUSEL facility.	40
4.1	SUR 100 configurations for the reactor periods experiment.	54
4.2	Kinetic parameters used for the reactivity computations of the SUR 100 reactor. .	55
4.3	Summary table of the reactivity experiment in SUR 100.	56

Nomenclature

Institutions

- EPA* U.S. Environmental Protection Agency
EPFL École polytechnique fédérale de Lausanne
IKE Institut für Kernenergetik und Energiesysteme
NRC U.S. Nuclear Regulatory Commission
PSI Paul Scherrer Institut

Physical Symbols

- β Delayed neutron fraction
 Λ Average prompt neutrons life-time
 λ Decay constant
 ω Inverse stable reactor period
 Φ Neutron flux
 ρ Reactivity
 $A(t)$ Activity
 C_i Concentration of the i-th group of delayed precursors
 DR Dominance ratio
 F Fission operator
 k Multiplication factor
 k_{eff} Effective Multiplication factor
 L Neutron leakage operator
 $n(t)$ Neutron population
 S Neutron scattering operator
 T Neutron collision operator
 $T_{1/2}$ Half life

Other Symbols

APD Avalanche Photodiode

C\E – 1 Relative discrepancy between computed and experimental results

CP1 Cadmium control plate 1

CP2 Cadmium control plate 2

FPGA Field Programmable Gate Array

GA Gaussian Amplifier

LT Low Threshold

PCB Printed Circuit Board

pcm Per cent mille

SCA Single Channel Analyzer

SiPM Silicon Photomultiplier

1 Introduction

The Siemens SUR 100 experimental facility [1] is a zero-power thermal reactor operated by the Institut für Kernenergetik und Energiesysteme (IKE) at the University of Stuttgart. The reactor, which is used mainly for educational purposes, is provided with several experimental channels for the insertion of detectors and nuclear instrumentation.

Over the years, no studies have been carried out on the neutron thermal flux distribution within the reactor channels, exception made for a teaching experiment with the use of Manganese activation samples. For this reason, an academic collaboration between the IKE and the Laboratory for Reactor Physics and System Behaviour (LRS) at the École polytechnique fédérale de Lausanne (EPFL) has been established. The objective of the collaboration was to perform high spatial resolution measurements to characterize the neutron flux distribution inside the experimental channels of the reactor and to compare the measurement results with Monte Carlo simulations.

An innovative miniature detector developed by the EPFL-LRS in collaboration with the Paul Scherrer Institut (PSI) [2] has been employed for the task at hand. Three units of the fiber-coupled scintillator detector were used in different arrangements to optimize the flux characterization of the experimental channels of the reactor. Several tests have been conducted in the CROCUS facility at EPFL prior to the experimental campaign, in order to assess the working principle of the miniature detectors.

The purpose of the highly localized measurements in SUR 100 was to acquire a detailed characterization of the neutron thermal flux distributions within the experimental channels of the reactor, which would not be achievable with other kind of detectors. Compared to the previously used activation techniques, the use of miniature detectors brings multiple advantages. Their small size results in a neutron flux perturbation lower than any other conventional detector and allows for measurements with high spatial discretization. In addition, their high sensitivity, combined with a low production cost and the possibility for parallel detection, paves the way to accurate measurements of reaction rates gradients on small spatial scales [3].

As a support for the experimental activities, extensive use of Monte Carlo simulations has been made for the present work. A preexisting MCNP [4] model of the reactor has been converted into Serpent2 [5] syntax and used to run particle transport simulations. Monte Carlo simulations have been performed to design the experiments for the experimental campaign, and then repeated to compare their results to the acquired measurements.

1.1 Design of the SUR 100 reactor

The Siemens Training Reactor SUR 100 is a thermal zero-power reactor built in 1964 and located in the university of Stuttgart. It is used for educational and research purposes by the Institut für Kernenergetik und Energiesysteme (IKE). The reactor has a maximum thermal power output of 1 W, with a nominal power of 100 mW. It is equipped with a homogeneous core, composed of solid cylindrical slabs of moderator with fuel particles dispersed inside. The core is provided with a lifting mechanism which can move axially the lower core section away from the upper one. The core halves are separated for the shutdown and brought together for the startup of the reactor. The reactivity regulation is performed with two cadmium control plates, which are steered into the core from below. The reactor is provided with various experimental channels, that allow the insertion of nuclear instrumentation into the core or in its proximity. SUR 100 is operated from the control desk visible in Fig. 1.1.

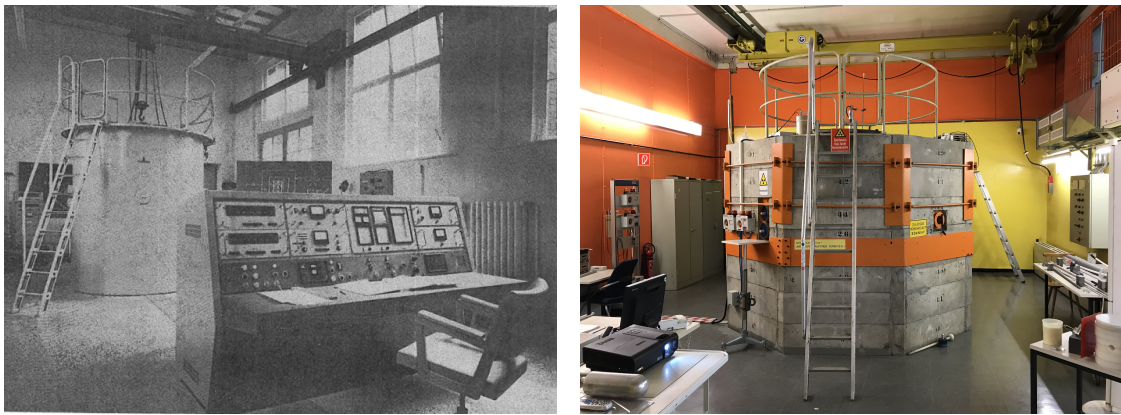


Figure 1.1: Pictures of the reactor hall in the 60's (left) [1] and nowadays (right).

The main components of the reactor, which are schematically depicted in Fig. 1.2, are hereafter listed:

1. Reactor core;
2. Inner reactor vessel;
3. Graphite reflector:
 - (a) Inner reflector;
 - (b) Outer reflector;
4. Lead shielding;
5. Base plate;
6. Reactor vessel;
7. Core lifting device;
8. Control units:
 - (a) Drive system;
 - (b) Control plate;
9. Axial thermal shielding;
10. Experimental channels;
11. Neutron detectors;
12. Cavity beneath the core;

13. Shielding.

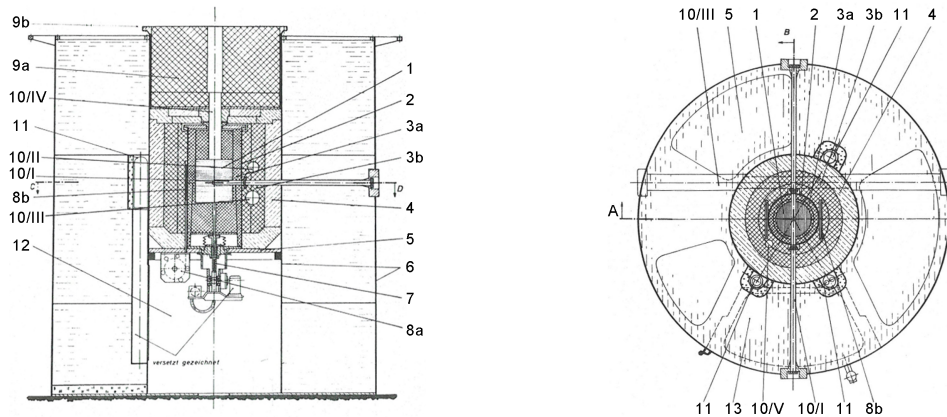


Figure 1.2: Vertical (left) and horizontal (right) cuts of the SUR 100 reactor [1].

Details and characteristics of each component are provided in the following sections.

1.1.1 Reactor core

The reactor core of SUR 100 is composed of several superposed cylindrical slabs made out of a homogeneous mixture of fuel and moderator. The moderator is solid polyethylene (PE), while powder of triuranium octoxide U_3O_8 , also known as "Yellowcake", is deployed as fuel with an enrichment of approximately 20% of U-235. The granulometry of the fuel powder is fine enough to consider the core material completely homogeneous, as no grain boundaries are visible inside the core slabs [1]. Fuel and moderator together constitute a solid homogeneous mixture with a density of 1.25 g/cm^3 and a U-235 content of 60 mg/cm^3 . The moderator has a density of 0.93 g/cm^3 at $20 \text{ }^\circ\text{C}$, with a variation of 1% due to temperature change of $17 \text{ }^\circ\text{C}$ [6].

The core consists of a cylinder with a height of 242 mm and a diameter of 240 mm, when the two core halves are assembled. As can be observed in Fig. 1.3, the slabs composing the core have a thickness which decreases along the z-direction. The reason behind this lies in the need of being able to adjust the core height during the so called "approach-to-critical experiment". Indeed, in the course of the installation phase of the reactor, the said experiment has been carried over to determine the correct height of the core to bring the reactor to criticality. The "core construction kit" allowed to adjust the height of the core in the range 22.7-27.5 cm, in steps of 1 mm. Since 1964, when the core height was fixed at 24.2 cm, the core dimension have been maintained unchanged.

As depicted in Fig. 1.3, the core has a central through cavity of cylindrical shape, used to insert nuclear instrumentation, samples and sample holders named Experimental Channel I. The channel passes along a diameter of the core and it is located at the interface between the upper and the lower core section. Indeed, while the upper core half is fixed, the lower core section is movable and can be shifted vertically generating a maximum displacement of 45 mm. The movement of the lower core half does not imply a movement of the experimental channel, which remains fixed at its position.

The core halves separation is actuated for the reactor shutdown, as it represent a very efficient way to insert negative reactivity. The core lifting mechanism (also depicted in Fig. 1.3) allows to move the lower core section together with the lower part of the inner graphite reflector. For the start-up, the drive mechanism actuates a displacement of the lower core section at

a velocity of 8 mm per minute [6], while in case of a safety shutdown the lower core section is slid downwards by effect of gravity.

The core is encompassed by a 20 cm thick graphite reflector in the radial direction, with the function of reducing the neutron leakage.

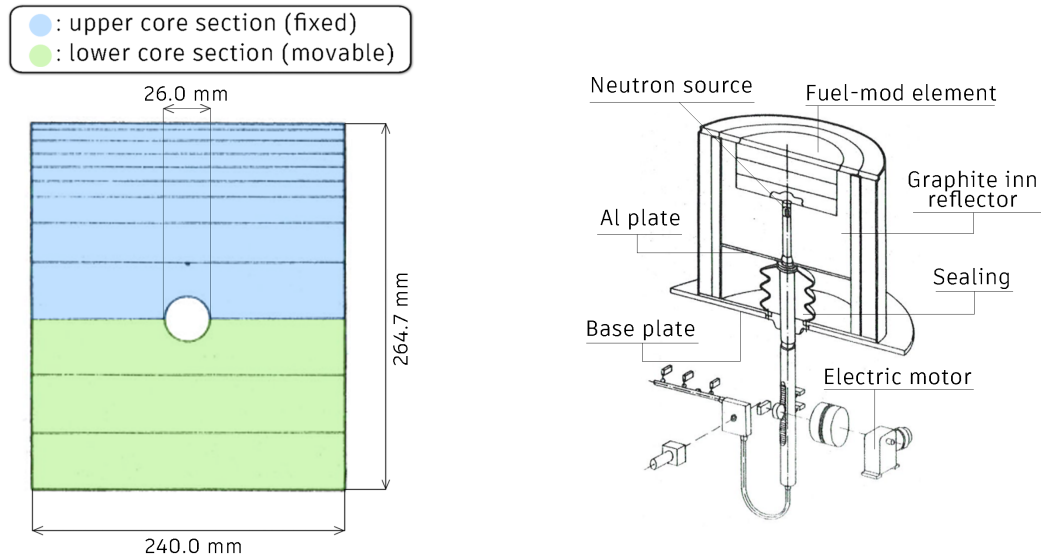


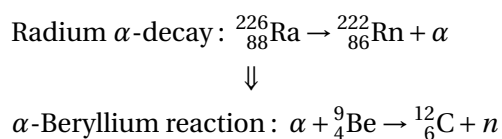
Figure 1.3: Scheme of the core dimensions (left) and its components (right) [1].

1.1.2 Neutron source

As there is no intrinsic source, the reactor is equipped with an external Ra-Be neutron source to initiate the fission reaction chain. An apposite driving system is capable to extend and retract the neutron source for the reactor start-up. The source could be positioned in three different ways:

1. The source is inserted in a recess in the lowest fuel-moderator plate, so it is in the closest position to the reactor core;
2. The source is extracted from the core and located at the level of the base plate;
3. The source is below the level of the base plate (position only reached in case of removal of the neutron source).

The neutron source is a common Ra-Be source, which generates neutrons through an (α, n) reaction of the Beryllium particles, while the α particle is produced by nuclear decay of the Radium. The reactions are summarized hereafter.



1.1.3 Graphite reflector

The reactor core is enclosed in a graphite reflector, which improves the neutron economy of the system by reflecting back into the core region a relevant part of the neutrons that would

leak from the volume in which the fissile material is contained. The reflector, which has a radial thickness of about 20 cm, is composed of two different elements: the inner reflector and the outer reflector. The reason behind this subdivision lies in the capability of motion of the lower core section. Indeed, when the core halves are separated by lowering the bottom section of the core, the inner reflector must support the movement by moving downward as well. A more detailed description of the component is provided in the following lines.

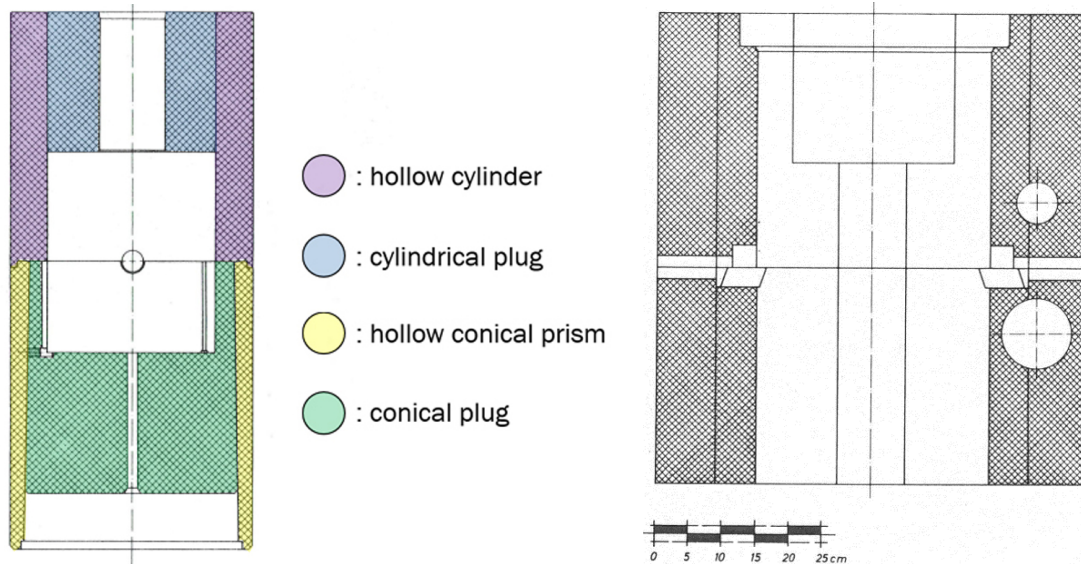


Figure 1.4: Schematics of the inner (left) and outer (right) components of the graphite reflector [1].

Inner Graphite Reflector. The inner graphite reflector is the first component in direct contact with the core, and beyond its primary function it serves also as a support for the lower core section. Indeed, when the core halves separation is actuated, the movable portion of the inner reflector moves together with the lower core section to support its movement. The detailed scheme of Fig. 1.4 shows the structure of the inner reflector, which is made up of an hollow cylinder and a cylindrical plug for the upper section, and two analogues conical components for the lower section. The vertical hole above the core is the cavity for the Experimental Channel IV. Since the inner reflector is capable to contain a core of a maximum height of 28 cm, the axial gap between the uppermost fuel-moderator plate of the core and the inner reflector surface is partially filled with a pure polyethylene plate. The inner reflector is enclosed, together with the reactor core, in a gas-tight aluminum container able to contain the gases produced by fission reactions, named inner reactor vessel.

Outer Graphite Reflector. The outer reflector is made of two concentric hollow cylinders, which together have a radial thickness of about 15 cm. Unlike the inner one, the outer reflector is fixed and is not provided with movable parts. Two experimental channels (II and III) pass through the outer reflector tangentially with respect to the core (see Fig. 1.4). A more detailed description of the experimental channels is given in Sec.1.1.7.

1.1.4 Inner reactor vessel

The inner reactor vessel encloses the inner part of the graphite reflector, together with the core, in a gas-tight manner. In such a way, all the fission gases produced by fission reactions are contained in order to avoid the spread of radioactivity in the surroundings of the reactor. The inner reactor vessel, made out of aluminum, is provided with several accesses (see Fig. 1.5).

Two channels pass through the vessel : one from above (IV) and one from the lateral surface (I). The bottom end of the vessel is welded and it is provided with a circular opening in the centre to allow the core and control plates lifting mechanisms to have access to the core. As depicted in the figure, the top of the vessel is closed by means of a plate connected with a flange.

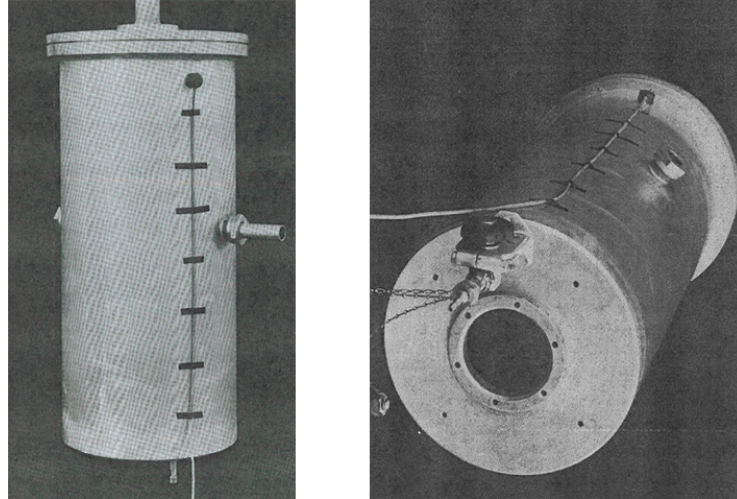


Figure 1.5: Side and bottom view of the inner reactor vessel [1].

1.1.5 Control plates

Two control plates made of cadmium serve to control the reactor behaviour. Their active part, which is a rectangular cadmium foil, has a height of 29 cm, a width of 25 cm and a thickness of 3 mm. The cadmium foil of the control plates is coated with an aluminum layer, which prevent the risk of abrasion. Both the plates are inserted from below through drive mechanism represented in Fig. 1.6. It consists in a geared motor driving a drum via a two stage gear and an electromagnetic disk clutch. The control plate is driven into an aluminum guide and connected to the drum by a steel belt spring.

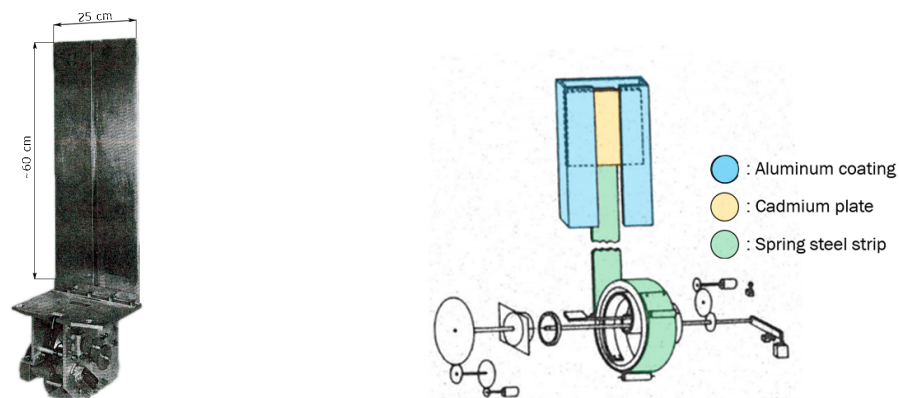


Figure 1.6: Picture of a control plate (left) and scheme of its drive mechanism (right) [1].

The control plates have an axial stroke of 250 mm, and they can be completely inserted in about 200 ms from their end position. The velocity of insertion of the control plates, and therefore their insertion time, can be adjusted by changing the pretension of the spiral spring lying in the drum. For the reactor start-up, once the two core section are merged together, the control plate 1 is completely withdrawn while the control plate 2 is used to reach criticality. According to the information obtained via personal communication with the IKE laboratory, the

criticality is reached when the control plate 2 is lowered down to a range between 185 and 195 mm from its inserted position. The position of the two control plates with respect to the core center is given in the horizontal cut of Fig. 1.11.

1.1.6 Reactor shielding

The SUR 100 reactor is provided by many layers for radiation shielding, both in radial and axial directions, to prevent neutron and gamma radiation from exceeding the limits imposed by regulatory bodies. The radial shielding consists of (from the inside to the outside):

- 10 cm of lead shielding;
- 60 cm of plastic granulate enriched with Boron (LUPOLEN);
- 30 cm of concrete shielding, which represent the ultimate shield for the radiation produced in the core.

On the other hand, the axial shielding comprises 10 cm of lead, 55 cm of graphite and a Boron-enriched Polyethylene slab of 10 for the section above the core, while the section below the core is simply shielded with 10 cm of lead. A more detailed description of the shielding components is provided in the following paragraphs.

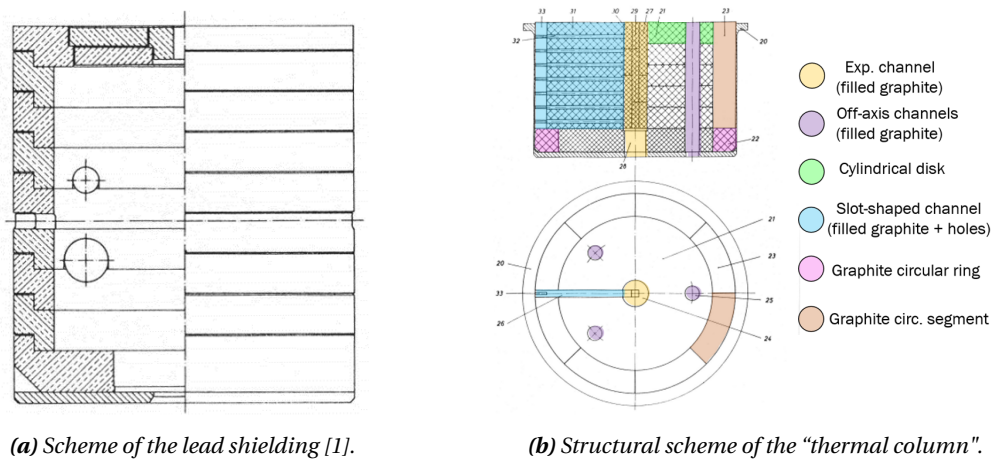


Figure 1.7: Scheme of lead shielding and "thermal column".

Lead shielding. It is made out of eight superposed lead rings and a top cover lid, and it surrounds the outer graphite reflector on all sides for a thickness of 10 cm. All the rings are coated in a protective layer of reinforced steel, which gives structural solidity and prevent the formation of cracks. As shown in Fig. 1.7a, the component is provided with four accesses for the experimental channels (two tangential, one axial and one radial through the core). The circular opening of the bottoming ring allows the drive mechanisms for the lifting of control plates and lower core section to have the necessary operational space. The cylindrical recess created by the bottoming opening and the base plate on which the lead shielding rests serves as a housing for the bottom of the inner vessel. Despite its lack of structural stability, lead is widely used in radiation shielding for its high atomic number ($Z=82$) and high density (11.35 g/cm^3) which allow for the attenuation of photons by photoelectric effect, Compton scattering and pair production.

Graphite axial shielding. The reactor is provided with a graphite axial shielding, which lies on top of the lead shielding cover lid. It has a height of 55 cm, and it is named "thermal col-

umn" due to its capability of thermalizing neutrons. In principle, both height and the diameter of the thermal column can be adjusted, being it composed of several parts assembled together. Nevertheless, its geometry has remained unchanged since 1969. A scheme of the various components is given in Fig. 1.7b. The thick layer of graphite and its high scattering cross section for neutrons, minimize the probability of leakage of neutrons in the axial direction.

LUPOLEN shielding. The LUPOLEN shielding constitute a 60 cm thick plastic granulate layer enriched with Boron (13 %) to enhance the neutron absorption. It is located at the interface with the lead shielding, and it was inserted only in a second phase in the reactor geometry. Indeed, the original design of SUR 100 used to include a layer of acid boric water solution (with 5% boron concentration) instead of the LUPOLEN shielding. Most likely, the way easier management of the plastic material with respect to the water solution was a key factor in contributing to substitute the original shielding, which could have been problematic for issues connected to water leakage and/or evaporation. A picture of the plastic granulate enriched with boron is visible in Fig. 1.8.

Concrete shielding. The concrete shielding is the outermost shielding barrier and it is visible from the external side of the reactor. It is about 30 cm thick and it is not in direct contact with the LUPOLEN shielding, given the presence of about 20 cm of air gap between the two. On the external surface of the concrete shielding are flanged the access ports to the horizontal channels (Experimental channels I, II and III). A metal ladder is attached to the outside of the concrete to give the SUR 100 operators access to the top of the reactor (see Fig. 1.1).

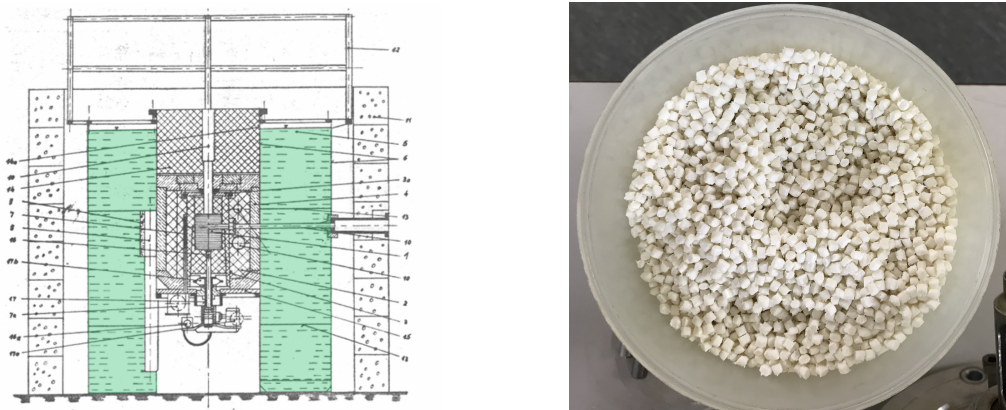


Figure 1.8: Vertical cut highlighting the LUPOLEN shielding (left) and picture of its composition (right) [1].

1.1.7 Experimental channels

Being a training reactor, SUR 100 is well equipped with various experimental channels, used to insert into or close to the core nuclear instrumentation such as detectors or activation samples. Channels are used also for the insertion of moderating elements inside the core, such as polyethylene plugs, that enhance the neutron thermalization in the core region.

SUR 100 has a total of five channels, of which only three are currently available for experimental purposes. They are named as follow:

- Experimental channel I : it is a central cylindrical channel that runs through the whole reactor, passing for the core center and determining the separation interface between the core halves. It has a diameter of 26 mm in its narrow section and it is gas-tight from the core;

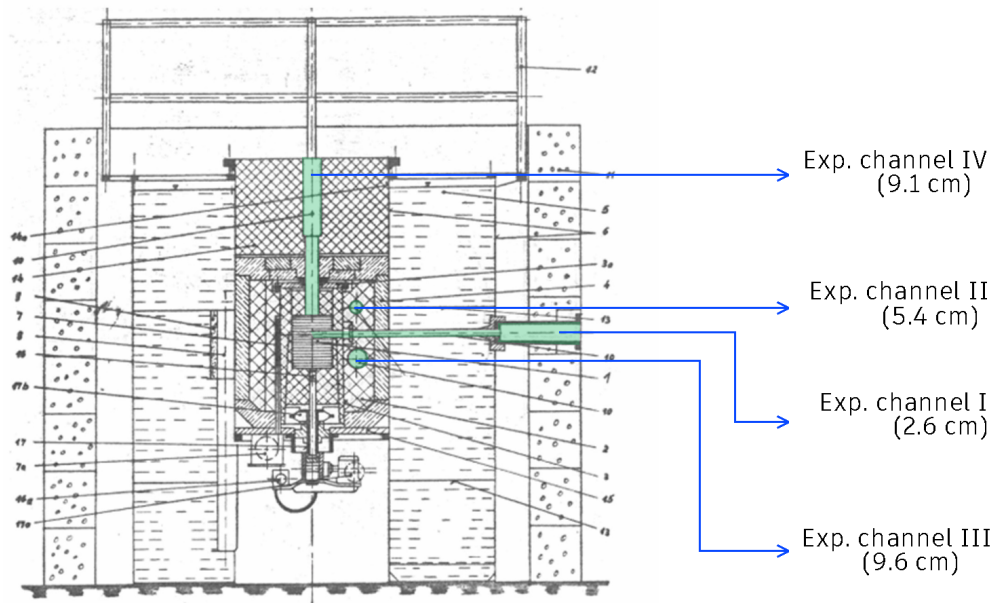


Figure 1.9: Depiction of four out of the five experimental channels of SUR 100.

- Experimental channel II : it is a tangential cylindrical channel penetrates the outer graphite reflector horizontally. It is located above the level of the experimental channel I and it has a width of 54 mm;
- Experimental channel III : it is a tangential channel in the outer graphite reflector, similar to the experimental channel II. The difference lies in its bigger diameter (96 mm) and in its location beneath the level of the experimental channel I.
- Experimental channel IV : it is a vertical channel which could give access to the top plate of the core. It has a diameter of 96 mm in the narrow section and it is inaccessible due to its filling with graphite.
- Experimental channel V : it is a vertical channel visible in the horizontal cut of Fig. 1.2, and it is inaccessible as well. It has a diameter of 51 mm and it is filled with reflector material.

To summarize, out of the five experimental channels of SUR 100, only three are actually available for experimental purposes, and they are the channels I, II and III.

1.1.8 Reactor monitors

The reactor is equipped with four neutron detectors used as power monitors, located in three different cavities as shown in Fig. 1.11. They consist of two ionization chambers operated in current mode (one of which with compensation for gamma radiation and logarithmic amplification), and two BF_3 counters operated as Geiger-Muller tubes. A total of five preamplifiers are deployed: one for each BF_3 counter, one for the uncompensated ionization chamber and two for the compensated one. The detectors are inserted vertically into cylindrical housings made of polyethylene, which serves as moderator and reflector for thermal neutrons.

1.1.9 Cavity beneath the core

The reactor door depicted in Fig. 1.11 leads to a cavity below the level of the core, which allows access to the drive mechanism of the control plates and the lower core section, the neutron

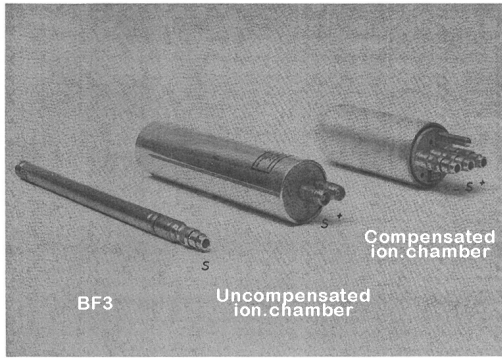


Figure 1.10: Picture of the three detectors of SUR100 [1].

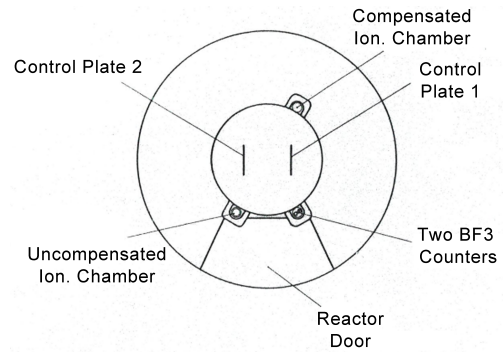


Figure 1.11: Horizontal cut of SUR 100 at the level of the detector housing [1].

source and the neutron detectors instrumentation.

In the picture of Fig. 1.12 are visible the drive mechanism for both the control plates on the sides, and the one for the lower core section in the center.

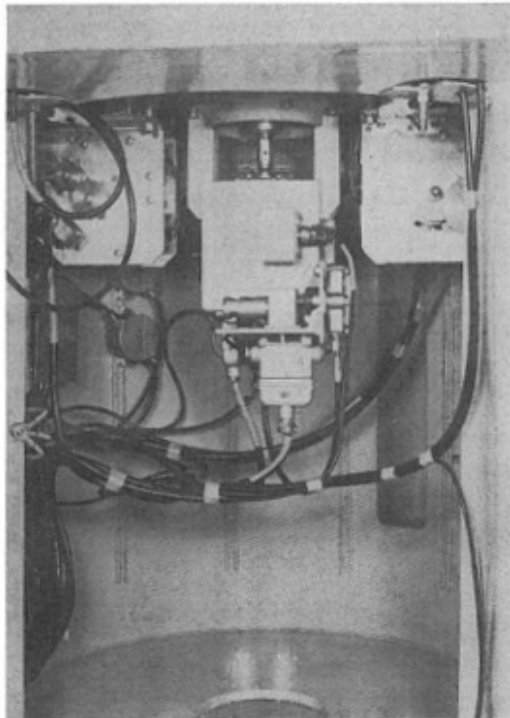


Figure 1.12: Picture of the cavity beneath the core [1]

1.2 Miniature neutron detector description

A miniature fiber-coupled scintillator for in-core neutron detection has been developed in the Laboratory for Reactor Physics and Systems Behaviour (LRS) at EPFL in collaboration with the Paul Scherrer Institut (PSI) [2]. Its miniature dimensions allow for very localized measurements, while neutron sensitivity remains conserved. Indeed, through past experiments the detector has revealed improved performances with respect to others in-core detecting devices,

by showing a sensitivity one order of magnitude higher than a miniature fission chamber or a sCVD diamond detector [7]. The low production cost and the easy parallelization capabilities make this design appealing for core mapping of the neutrons thermal flux.



Figure 1.13: Picture of the miniature fiber detector. As the protective Aluminum cap is removed, the scintillator screen is visible (in white).

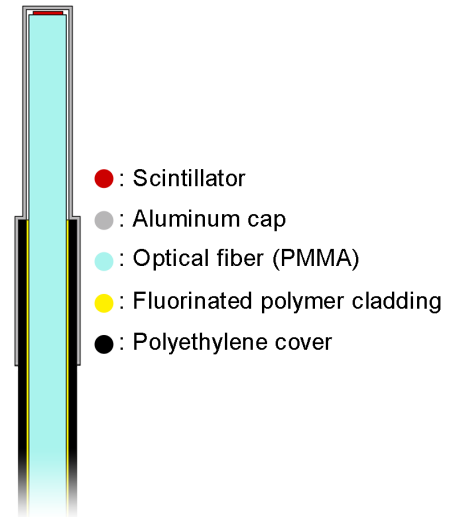


Figure 1.14: Scheme of the front-end of the detector.

1.2.1 Detection principle

The neutron sensitive area of the detector is a scintillator screen of approximately 1 mm^2 (see Fig. 1.13), obtained from a flat sheet produced by Scintacor [8]. The scintillator is constituted by an inorganic crystal, namely zinc sulphide doped with silver $\text{ZnS}(\text{Ag})$, mixed with ^6LiF in the mass ratio 2:1.

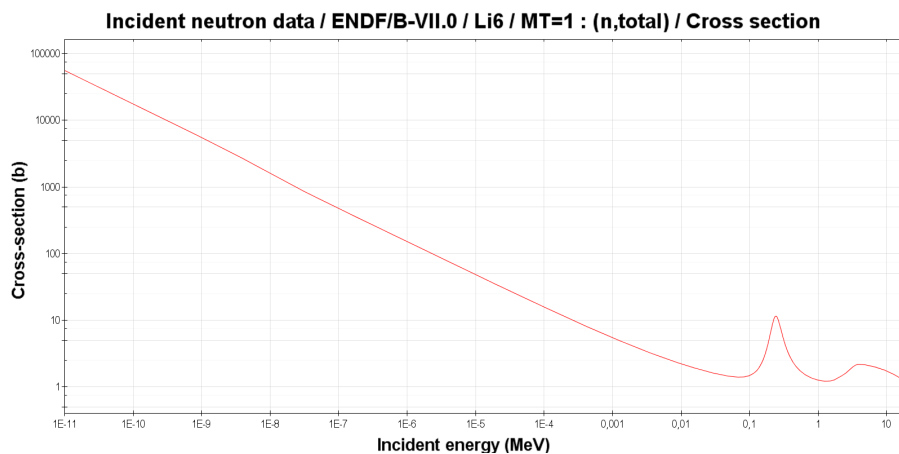
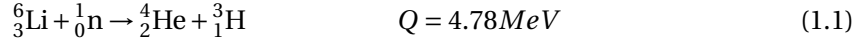


Figure 1.15: Cross section of the (n, α) reaction for ^6LiF according to the ENDF/B-VII.0 library [9].

The neutrons interact with the scintillator in a two step process, which consist of conver-

sion and scintillation.



The conversion of the incoming neutrons in charged particles is performed by the (n, α) reaction of the ${}^6\text{Li}$ atoms as described by Eq. 1.1. As can be inferred by looking at Fig. 1.15, this detector is designed for the detection of thermal neutrons, as the cross section of the (n, α) reaction of lithium is negligible for energies in the fast region of the spectrum. The α particle and the Tritium arising from the reaction are able to excite the ZnS molecules of the crystal, which after de-excitation emit visible light in the blue frequency of the spectrum by luminescence. Through this two-step process, the incoming neutron radiation is converted to a light signal.

A plastic optical fiber produced by ESKA [10] is then coupled to the scintillator screen by means of an optical grease produced by St-Gobain [11] to minimize light losses. The photons produced in the scintillation events are guided to the read-out electronics through an optical fiber with a polymethyl methacrylate (PMMA) cylindrical core. The core, with an average diameter of 1.96 mm, is coated in a 0.04 mm thick fluorinated polymer cladding. The photons guiding inside the fiber is guaranteed by the lower refractive index of the cladding, which enables their total internal refraction. An additional 1 mm plastic protection wraps around the fiber over its entire length to prevent the risk of damage. A schematic view of the structural composition of the detector is provided in Fig. 1.14.

1.2.2 Standard signal processing

With aim of increasing the readability of the signals arising from neutrons interactions, the light photons produced by the scintillator screen need to be converted into a current signal and then processed apposite electronics. An example of a standard analog detection chain setup used for the miniature neutron detector, depicted in Fig. 1.16, is detailed in the following paragraphs.

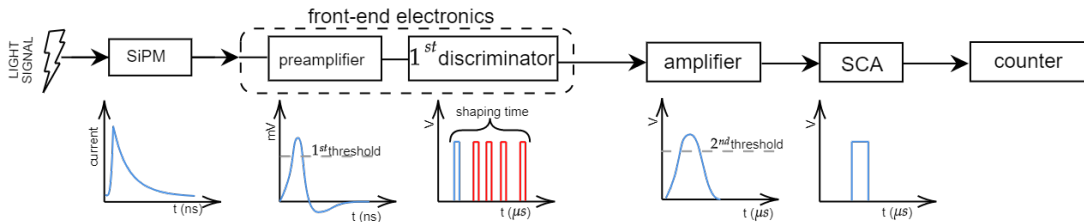


Figure 1.16: Schematic of a standard read-out electronics for miniature fiber-coupled detector. In correspondance of the main components are reported the respective output signals.

Silicon Photomultiplier A Silicon Photomultiplier (SiPM) consists of an array of small avalanche photodiodes (APDs), with dimensions in the order of tens of μm (see Fig. 1.18).

The single APD consists is a semiconductor detector working in Geiger mode that converts incoming photons into electrons by means of photoelectric effect. The amount of charge generated in a single event is amplified through an avalanche process that occurs at high values of the bias voltage. In Fig. 1.17, is schematized a light photon entering in the p+ region of the APD, which is kept as thin as possible to promote the passage of photons. Once in the π region, which constitute most of the photodiode, the photon can interact by creating an electron-hole pair. The electron is driven to the right in a region of high electric field, where it creates additional electron-holes pairs with the result of amplifying the current signal. Gains in the order of few hundreds (per APD) are commonly achieved [12]. Due to its high sensitivity to visible

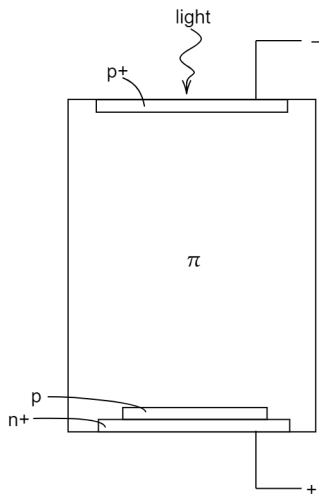


Figure 1.17: Scheme of an Avalanche photodiode [12].

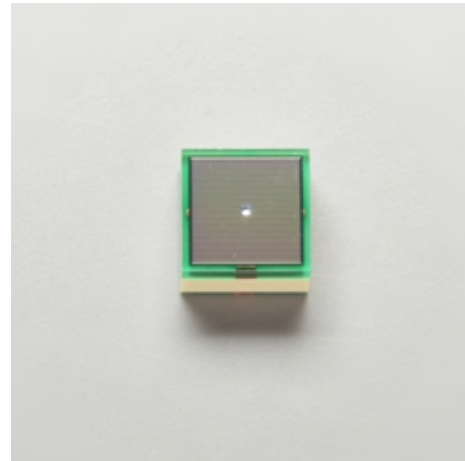


Figure 1.18: Picture of a Silicon Photomultiplier from Hamamatsu [13]

light, the SiPM must be kept in the dark to minimise background noise signals. For the same reason, the coupling with the end of the fiber carrying the light signal must also be properly tight. The signal in current generated by the SiPM, which has an amplitude dependant on the bias voltage applied and a length in the range of few tens of nanoseconds, is then processed through a preamplifier.

Front-end electronics The front end electronics consists in a component which convert the current pulse from the SiPM into a voltage signal, which is the preamplifier, and of a first system to discriminate the signals, i.e. the discriminator. The amplitude of the signal exiting from the preamplifier can assume only discrete values, as it derives from the proportionality of the number of APDs triggered with the coincidence of a scintillation event, while every photodiode generate the same amount of charges regardless of the number of photons it is hit from [7]. In the picture of Fig. 1.19, where some output signals from preamplifier are represented, three discrete amplitudes are recorded accordingly to the number of cells of APDs triggered by the incoming photons.

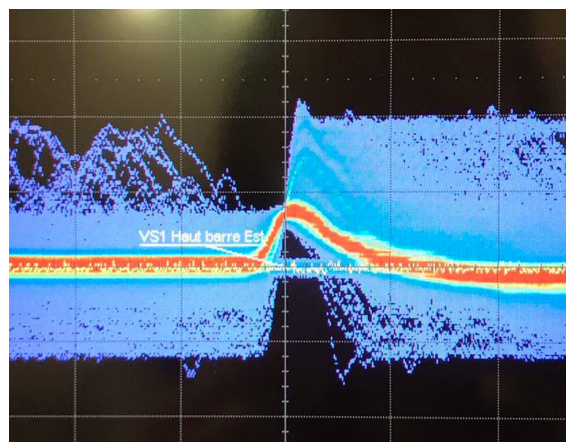


Figure 1.19: Example of output signals from the preamplifier in persistence mode. The scales are 1.00 V/div and 20 ns/div.

The analysis of the output signals allows also to determine the level for the first discrimina-

tion stage. Indeed, to cut most of the background noise it is possible to distinguish the signals according to their amplitude in voltage. After a threshold level has been chosen, the discriminator produces a square voltage signal only if the input pulse exceeded the predefined minimum level. In this way, all the signals lower than the threshold are classified as “noise” and then discarded by the acquisition system. If a neutron is detected with the described setup, a very dense train of square pulses is generated by the front-end electronics as a result of the big number of photons generated in the scintillation event.

Gaussian amplifier The square pulses generated by the first discriminator are then integrated in time by means of a Gaussian amplifier. Thus, it produces a signal with an amplitude proportional to the occurrence rate of the input signal produced by the first discrimination stage. By doing this, a few Volts high signal is generated in case of a dense train of pulses occurring in a preset time interval. On the other hand, if a random square pulse arises from the first discrimination stage, the height of the resulting signal is much lower. An example of the output signal from the amplifier, together with one from the first discriminator, is given in Fig. 1.20. The shaping time, which is representative of the interval of time over which pulses are integrated, can be manually selected and have an influence of the dead time of the detector.

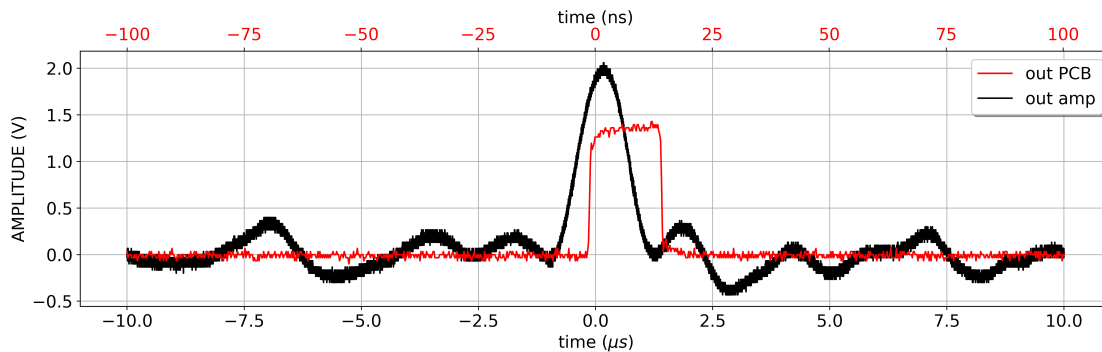


Figure 1.20: Example of output signals from the first discriminator (red) and from the amplifier (black).

Single channel analyzer (SCA) and counter The output signal from the amplifier is then processed through a second discriminator stage, performed by the SCA. The SCA produces a square pulse only if the input signal is higher than a preselected threshold. While the first discrimination level is determined by analyzing the signal amplitude, the second discrimination level is inferred from a Low Threshold curve, which description is given in Sec.3.2. The pulses in output from the SCA are then read from a counter, which keeps score of the number of detected neutron events.

1.3 Scope and outline of the thesis

This report summarizes the work carried over in the framework of a master’s thesis project in the spring semester of 2020 at EPFL-LRS laboratory. The two general objectives of the project, consisting of both experimental and computational activities, are :

- The characterization of the neutron flux of the experimental zero-power reactor SUR 100 operated by the Institut für Kernenergetik und Energiesysteme (IKE) of Stuttgart through experiments with miniature neutron detectors;
- The comparison of the experimental data with Monte Carlo simulations carried out with the Serpent2 particle transport code [5].

The synergy of the two objectives is supposed to lead to an accurate description of the neutron flux profiles inside the experimental channels of the SUR 100 experimental reactor and to further confirmations of the goodness of the computational Serpent2 model used for the work at hand.

Besides from the introductory sight on the scope of the work presented in this Chapter 1, the document is structured as described in the following lines:

- Chapter 2 describes the main features of the computational Monte Carlo model of SUR 100 converted for the Serpent2 transport code and analyzes the primary results obtained from the simulations carried out in view of the experimental campaign;
- Chapter 3 details the tests on the experimental instrumentation carried over in the LRS facilities as a preparatory activity to design the experimental campaign in the SUR 100 reactor;
- Chapter 4 reports the experimental activities performed in the framework of the campaign in Stuttgart. The main results are discussed and compared with computational data obtained through Serpent2 calculations adapted to the real measurements conditions;
- Chapter 5 summarizes the conclusions drawn from the experimental evidences obtained from the master's thesis project.

In the Appendices of the present document, a study on the neutron and gamma dose rate delivered in the surroundings of the SUR 100 concrete shielding (see Appendix A) and an example of the Serpent2 input file used to run the calculations for the work at hand (see Appendix B) are included.

2 Monte Carlo modeling and simulation of the SUR 100 reactor

The present chapter is dedicated to the description of the computational model of SUR 100 used to perform Monte Carlo calculations for the work at hand. A discussion for the selection of suitable run parameters is included in the content of the chapter, together with multiple calculations performed as a preparatory activity for the experimental campaign. The choices for geometry details and materials used for the reactor modeling are discussed together with the modifications introduced to enhance the usability of the model.

The code of choice for the simulations is Serpent-2.1.31 [5], a multi-purpose three dimensional continuous-energy particle transport code, developed at VTT Technical Research Centre of Finland [14]. Given that a preexisting MCNP [4] model of the reactor was made available from the IKE laboratory, its conversion to a suitable input was necessary in order to run the model with Serpent2, which was preferred for licensing reasons mainly, being it publicly distributed by the OECD/NEA Data Bank and RSICC (Radiation Safety Information Computational Center) since 2009 [14]. The converted Serpent2 model for the SUR 100 reactor is made available in Appendix B.

The Monte Carlo simulations performed for this project have the twofold objective of designing the experiments for the Stuttgart campaign and comparing their results with the computational ones.

2.1 Description of the Serpent2 model

The Serpent2 model hereafter presented results from the conversion of an already existent MCNP input. As frequently happens, a certain level of approximation with respect to reality is accepted when building a computational model. Despite this, the assumptions made for the modeling of SUR 100 are careful not to have a significant impact on the physical parameters of interest for this work.

2.1.1 Geometry and materials

All the geometrical details of the reactor have been taken from the existing MCNP model, which was used as a reference. The converted model is therefore totally in agreement with the reference one, and lies under the same assumptions. The main simplifications of the computational model concern:

- The absence of all the drive mechanisms shown in Fig. 1.12, as they are not impacting the neutron economy in a relevant way;

- The absence of the experimental channel 10/V, being it filled with Graphite and therefore considered part of the reflector;
- The absence of the detector housings and the detectors themselves, since deemed non-impacting for the studies performed in this work because of their distance from the experimental channels;
- The absence of the aluminum coating of control plates, since they are assumed to not perturb significantly the neutron flux in the thermal range of interest.

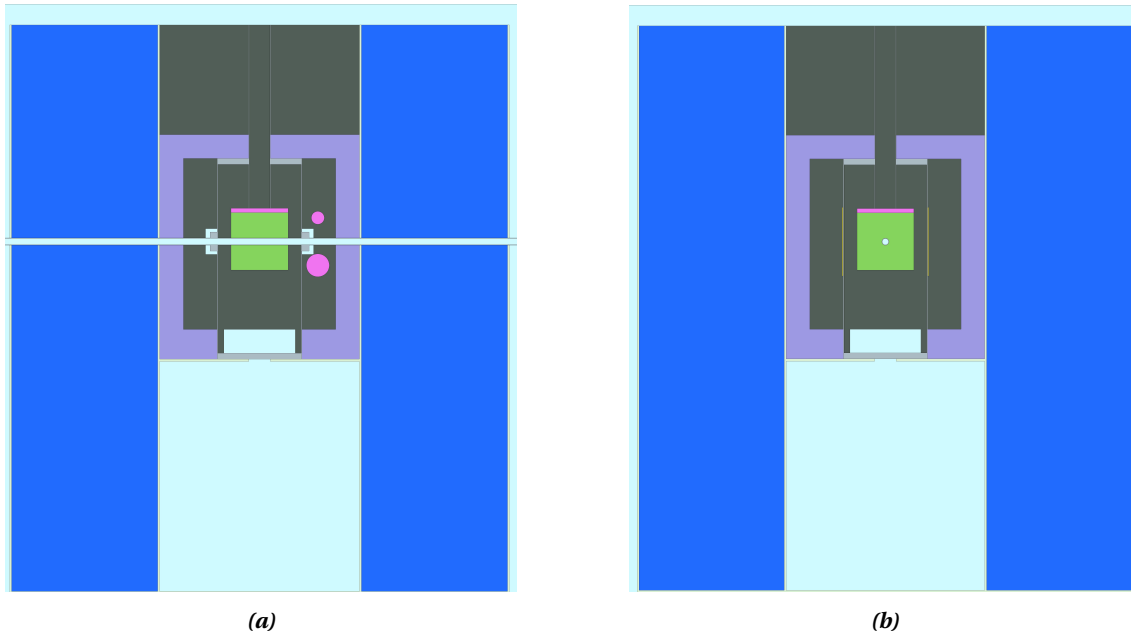


Figure 2.1: Vertical cuts through the core obtained with the Serpent2 model.

The MCNP model has been used as a reference also for the materials constituting the various component of the model. To double-check the validity of the materials compositions, a comparison with a “Compendium of Material Composition Data for Radiation Transport Modeling” [15] is performed, and a substantial agreement is found. The temperature at which the neutron cross sections of the elements are taken is 293 K, with differences of few Kelvins in dependence of the availability of data in the cross section library, often provided at 300 K.

In Fig. 2.1 and 2.2, which show plots produced by Serpent2, the geometry of the reactor together with the material distribution is represented. In both the figures it is possible to notice the absence of concrete shielding, which was implemented in the model after its conversion from the MCNP model. Both materials compositions and geometry dimensions of the model are affected by their relative uncertainties, since it is unrealistic to think of them as perfectly overlapping with reality. Unfortunately, these uncertainties are very difficult to estimate and propagate, even if it is necessary to take note of their existence.

2.1.2 Model enhancement

To improve its usability and its level of accuracy, the computational model has been adapted with minor modifications beyond its bare conversion from the MCNP language. The main adjustments to the model, consisting mostly in minor modifications, are listed hereafter.

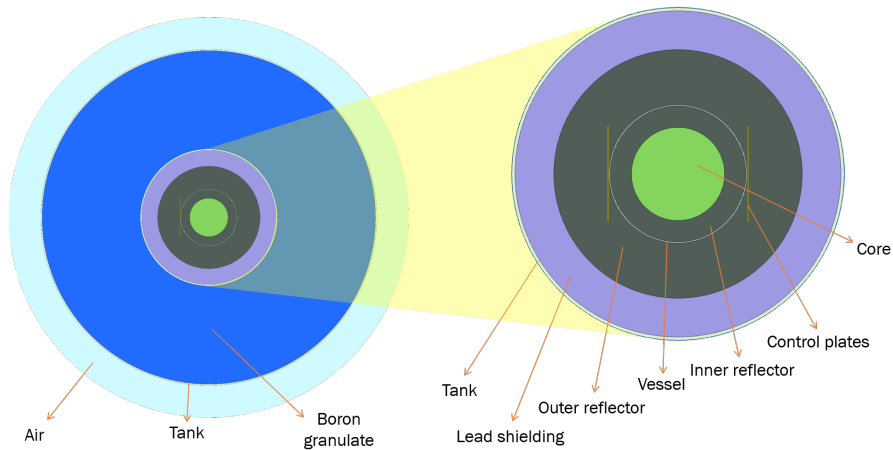


Figure 2.2: Horizontal cut through the reactor with focus on the core zone.

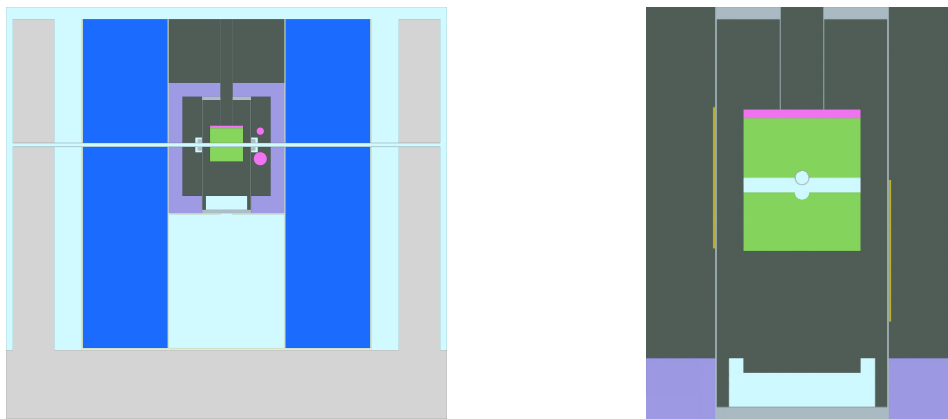


Figure 2.3: Vertical cut of SUR 100 with the added concrete shielding (left) and example of movement of the lower core sections and the control plates (right).

Concrete shielding. Despite its absence in the model provided by IKE, the concrete shielding has been modeled in Serpent2. Although the presence of the outermost layer of the shielding might not affect the neutronics in the center of the core, it is key for eventual radiation protection studies (e.g estimation of dose rate delivered to the operators). While the geometric dimensions of the concrete shielding have been taken from the official documentation from Siemens [1], its composition has been assumed. Indeed, the composition provided by the MCNP material compendium has been used, assuming the concrete to be “regular concrete” [15]. The concrete shielding has been shaped with a cylindrical shape, being this a simplification motivated by the absence of geometrical data on the real octagonal shape of the component at the time of the modeling procedure.

Movable core section and control plates. To facilitate the modeling task of moving the control plates and the lower core section in different positions, the model is provided with a dedicated cell for each of the aforementioned components. This, together with the use of the `trans` command of Serpent2, enables to easily displace the elements without the need of a significant revision of the surfaces definition. It also paves the way to the usage of apposite scripts to automatize the calculations. Thanks to these enhancements, the two control plates can be steered independently in the range $[0, -250]$ mm and the lower core section (together with the lower section of the inner reflector) can be moved within the interval $[0, -45]$ mm.

2.2 Run parameters

This section is dedicated to the description of the main run parameters needed to set up a calculation with a Monte Carlo code. The focus is maintained on the particular nature of the problem at hand, by describing and motivating the choices made to run the neutron transport simulations with Serpent2.

2.2.1 k-eigenvalue criticality source method

In principle, Serpent2 gives the possibility to run a simulation in two different methods: the external source method or the k-eigenvalue criticality source method. With the first option, the neutrons are started from a user-defined distribution, and therefore it is used in sub-critical and non-multiplying systems. On the other hand, with the second option (which is the default calculation mode in Serpent2) the simulations are run in cycles, and the source distribution of a given cycle corresponds to the fission reaction distribution of the previous cycle. This last option, is therefore deployed with systems able to auto-sustain themselves from the neutronic point of view (so called "critical"). In the present work all the simulations are run in the k-eigenvalue criticality source mode, at which one could refer also briefly as "criticality mode". The criticality mode deeply relies on the well-known mathematics algorithm known as "Power iteration method", of which mention is made in the following lines.

Power iteration method. The power iteration method allows to easily find a solution for eigenvalue problems by starting from an initial arbitrary guess of neutron source or neutron flux. It is deduced starting from the compact formulation of Boltzmann neutron transport equation:

$$(L + T)\phi = S\phi + \frac{1}{k_{eff}}F\phi \quad (2.1)$$

where: L is the neutron leakage operator, T is the neutron collision operator, ϕ is the angular neutron flux for given position and energy, S is the neutron scattering operator and F is the fission operator. With a rearrangement of Eq. 2.1:

$$\phi^{(n+1)} = \frac{1}{k_{eff}^{(n)}}(L + T - S)^{-1}F\phi^{(n)} \quad (2.2)$$

and the assumption that fission neutrons of the previous generation n become source particles of the following generation $n + 1$:

$$\frac{1}{k_{eff}^{(n)}}\langle F\phi^{(n)} \rangle = \frac{1}{k_{eff}^{(n+1)}}\langle F\phi^{(n+1)} \rangle \quad (2.3)$$

which can be rearranged in:

$$k_{eff}^{(n+1)} = k_{eff}^{(n)} \frac{\langle F\phi^{(n+1)} \rangle}{\langle F\phi^{(n)} \rangle} \quad (2.4)$$

one can obtain the two equations that describe the method (Eq. 2.2 and 2.4)¹ [16].

To summarize, the criticality mode implies the simulation to be run in iterations, with the source distribution of each cycle coming from the fission reaction distribution of the previous cycle. Both the number of cycles and the number of simulated neutrons per cycle are a choice of the user, and depend on the level of accuracy that one aims to reach. As can be expected, to start a simulation in criticality mode, an initial distribution is needed. For this reason, a guess is made on the initial fission source distribution, and the code is run for a number of cycle which is enough to let the distribution converge. This preliminary cycles are called "inactive cycles", and their determination is described in Sec.2.2.2.

¹In Eq. 2.4 the diamond brackets stands for integration over the system space.

2.2.2 Inactive cycles determination

As previously stated, obtaining results free of contamination from the initial guess in k - eigenvalues problems requires a certain number of iterations to let the initial distribution source to converge. Therefore, it is useful to determine the minimum number of cycles needed for this convergence to happen, which is the minimum number of inactive cycles accepted for the results to be reliable.

It has been demonstrated [17] that assessing the convergence by analyzing only the behaviour of k_{eff} may lead to erroneous conclusions, particularly in problems with a high dominance ratio (DR). Since the Boltzmann equation has a series of eigenvectors ϕ_i , with a set of descending eigenvalues k_i , any flux distribution can be decomposed in a linear combination:

$$\phi = \sum_{i=0}^{\infty} a_i \phi_i \quad (2.5)$$

where a_i are coefficients obtained from integration of $\phi \cdot \phi_i$ over whole phase space. The dominance ratio DR is defined as the ratio between the second and the first eigenvalue of a given system:

$$DR = \frac{k_1}{k_0} = \frac{k_1}{k_{eff}}. \quad (2.6)$$

Since the higher order components of flux from Eq. 2.5 decay quickly in the iterative procedure, at a generic step n the flux could be approximated using only the two first components of the series. Moreover, the k_{eff} convergence in the power iteration is much faster than the neutron source convergence for high DR problems ($DR \rightarrow 1$). Another issue related to the evaluation of the convergence by looking only at the k_{eff} behaviour is due to the statistical noise inherent in the random walks of neutron in each generation, which cause the oscillations in the evaluation of the multiplication factor for different generations. For the above mentioned reasons another parameter is used to assess the convergence of the fission distribution, namely the Shannon Entropy.

Shannon Entropy. Shannon entropy is a well-known concept from information theory that allows to evaluate the convergence of the fission source distribution just from the knowledge of a single number [17]. When the Shannon entropy converge to a single steady state value, the source distribution can be said to be stationary. To compute Shannon entropy in Serpent2, a 3D grid encompassing the core has been introduced. In order to see the effects of the number of neutrons per cycle, two different simulations are run, and the results are summarized in Fig. 2.4 and 2.5.

As can be noted from the results, no relevant changes are observed with a different number of neutrons per cycle, besides from the slightly faster convergence of the Shannon entropy in the case with $2 \cdot 10^4$ neutrons per cycle. As a matter of fact, an estimate around 150 inactive cycles is deemed to be appropriate for the problem at hand.

2.2.3 Cross section libraries

For what concerns the neutron data libraries, all the computational results shown in the document at hand are obtained by running Serpent2 simulations with the use of the ENDF/B-VII.0 library [9]. Other cross sections libraries are used for comparative purposes, such as JEFF-3.1.1 [18] or JEFF-3.2 [19].

To include the information about the scattering of neutrons at thermal energies with Hydrogen bound in molecules such as Water or Polyethylene, also the Thermal Scattering Law

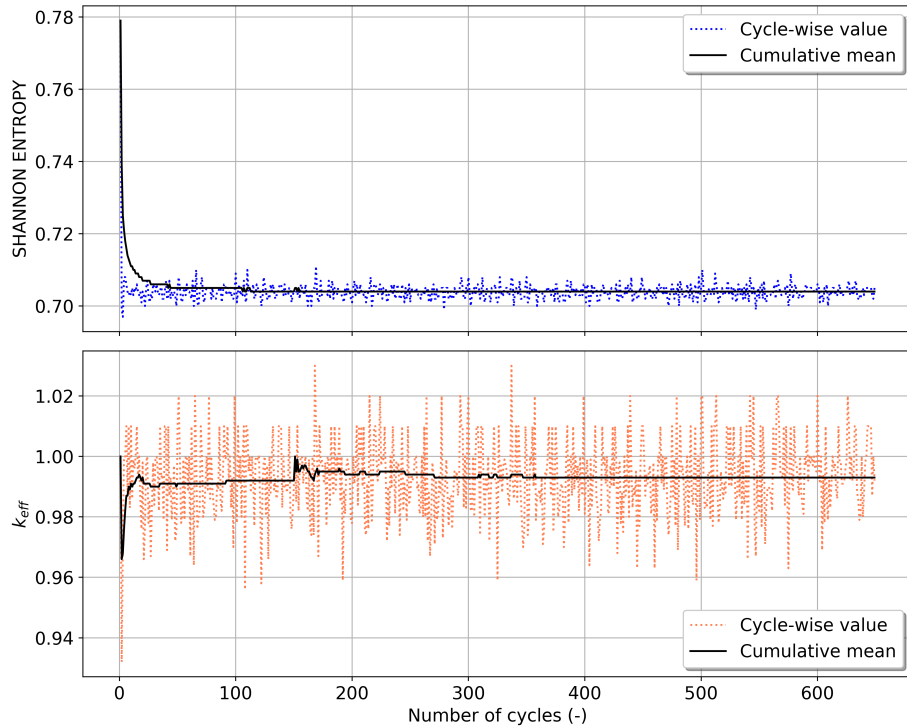


Figure 2.4: Source distribution convergence study with 10^4 neutrons per cycle.

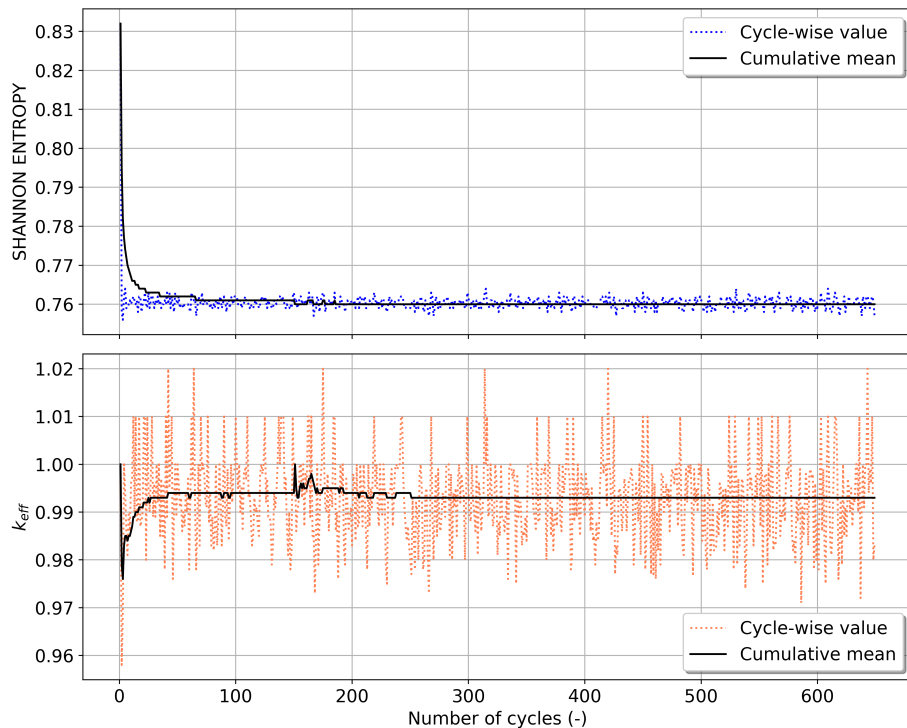


Figure 2.5: Source distribution convergence study with $2 \cdot 10^4$ neutrons per cycle.

(TSL) data have been implemented for the ENDF/B-VII.0 library. To highlight their impact on the reactivity of the system, in Fig. 2.6 are shown the results of one of the first calculations performed with the Serpent2 model. In the plot are depicted the values of computed reactivity of SUR 100 as a function of the position of the control plate 2 (further details on this calculation are available in Sec.2.3). The set of simulations is repeated twice, in order to assess the impact of using or not the thermal scattering libraries.

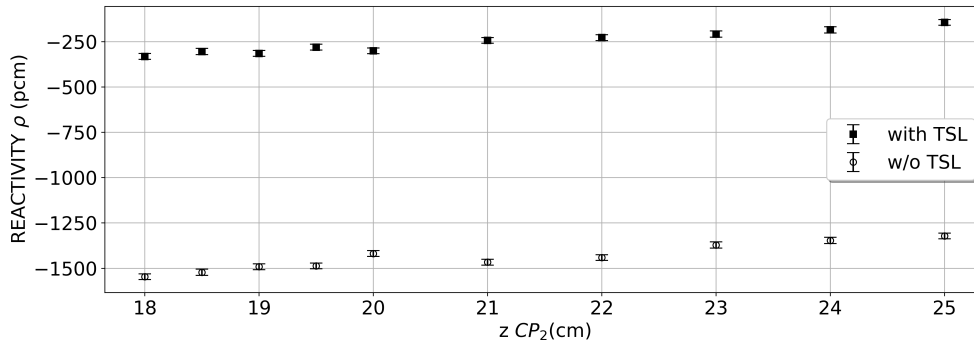


Figure 2.6: Effect of the inclusion of Thermal Scattering Libraries on the reactivity of SUR 100.

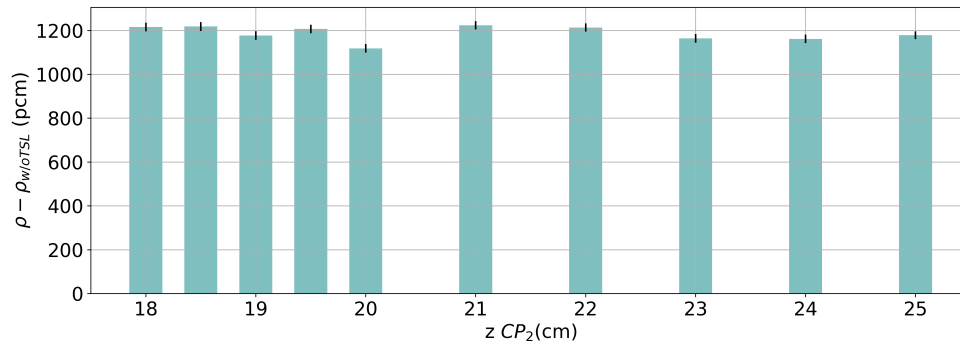


Figure 2.7: Difference in reactivity arising from not including Thermal Scattering Libraries.

The graphic visualisation of the difference in reactivity of Fig. 2.7 prove that not including Thermal Scattering libraries causes a significant k_{eff} underestimation of 1200 pcm, and therefore must be avoided.

2.2.4 Source rate normalization

When running a Monte Carlo simulations, normalization of the source rate is needed to relate reaction rate estimates to a user-given parameter. Among the several options for source rate normalization provided by Serpent2, in the work at hand all the computational results are obtained by normalizing the source rate by the total fission power of the SUR 100 reactor. In this particular case, a value of 0.1 W has been selected for the normalization, since it represents the nominal power at which the reactor is normally operated.

2.3 Reactor criticality computation

Determining the conditions at which a nuclear reactor reaches the criticality is fundamental for its safe operation. To reproduce the critical configuration of SUR 100, the developed computational model has been run, in order to simulate the nominal operational conditions of the reactor. Although it is often very difficult to obtain absolute estimations on the critical level with Monte Carlo simulations, the results remain valid if properly calibrated with experimental data. In this section are shown the main results obtained from Monte Carlo simulations, run with the objective of characterizing the critical configuration of the SUR 100 reactor.

2.3.1 Reactivity curve

Before starting with the analysis of the reactivity variation with the movement of the absorbing Cadmium plates inside the outer Graphite reflector, better is to recall the procedure with which the reactor is brought to criticality. The routine, which requires a few minutes to be carried over, takes place in three steps (see Fig. 2.8):

1. The lower core section, together with the lower part of the inner Graphite reflector, is moved upwards to close the 45 mm gap with the upper core section. The two Cadmium control plates are completely inserted inside the Aluminum coating.
2. The control plate 1 is progressively lowered to its end position, which is 250 mm lower than its inserted position.
3. The control plate 2 is then steered by monitoring the k_{eff} of the reactor, until the criticality is reached. In SUR 100, a $k_{eff}=1$ is achieved by placing the control plate 2 in a position from -185 to -195 mm from its inserted position², in dependence of various parameters that can affect reactivity (presence of instrumentation inside the experimental channels, temperature of the environment, etc).

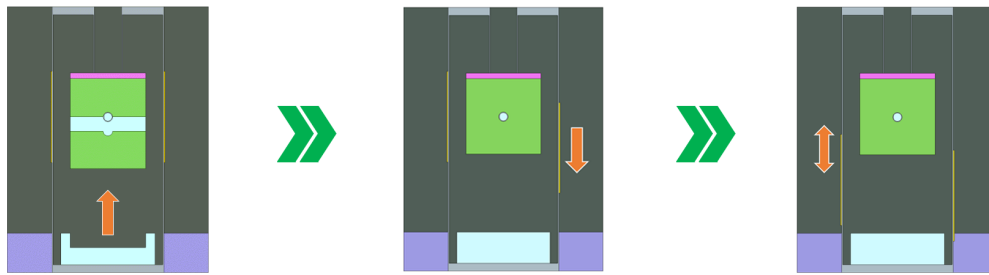


Figure 2.8: Scheme of the core start-up procedure.

By setting the SUR 100 geometry in the third step of the startup procedure, a series of simulations was carried over for different heights of the control plate 2. The process, that was automatized by means of an apposite shell script, gave as a result the value of the multiplication factor of the system for each of the configurations calculated. Thus, having a k_{eff} value for each height of the control plate 2, allowed to compute the reactivity of the system in each step through its definition:

$$\rho = \frac{k_{eff} - 1}{k_{eff}}. \quad (2.7)$$

The reactivity points recorded at different elevations of the control plate 2 are shown in Fig. 2.9.

As it is clearly shown in the plot, the reactivity of SUR 100 computed for the positions of the control plate 2 in the range [-185,-195] mm is well below the critical level. Indeed, a significant reactivity shortage of about 300 pcm results from the calculations. Furthermore, even with the complete lowering of the control plate to 2 its end position, the computed reactivity is about 150 pcm below criticality.

Such a result could not be representative of the real conditions in which SUR 100 is operated, and thus some unconsidered factors should be playing a role in generating this kind of discrepancy. Indeed, the origin of this inconsistency can be found in three different uncertainty sources:

²The position of the control plates is calculated using as their “inserted” position as the zero. When the CP are totally inserted their tip is located 5 mm above the top surface of the polyethylene slab lying on the core.

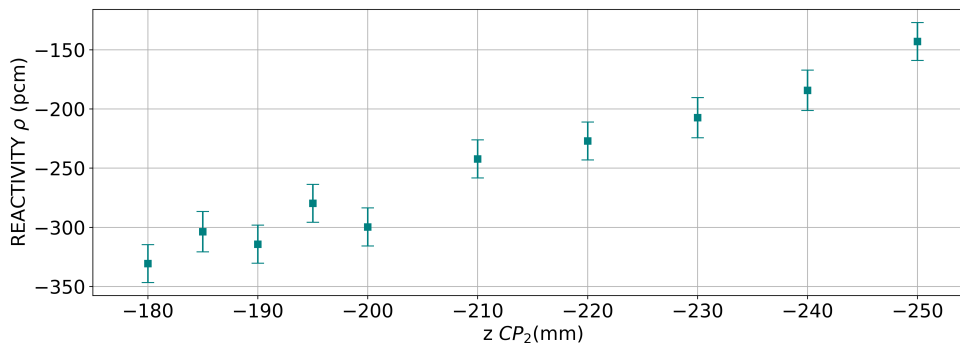


Figure 2.9: Reactivity of the system as a function of the height of CP2.

- Geometrical uncertainties: the actual geometry of the reactor could be slightly different with respect to the one of the computational model, and the results might be biased for geometrical reasons.
- Material properties uncertainties: the actual density and composition of each material cannot be identical of that of the modeled materials, a discrepancy is reasonably expected. To give an example, the air and the concrete composition were implemented taking as reference the MCNP compendium, which is not representative of the reality of the SUR-100 reactor. Also the material-related uncertainties cannot be evaluated quantitatively, but are surely present.
- Cross section uncertainty : the nuclear data that gives information about the probability of interaction of neutrons with matter are affected by uncertainties.

While acknowledging the presence of geometrical and material uncertainties, it is not possible to compute a numerical assessment on their entity. On the contrary, a rough evaluation on the discrepancy in the result generated by the use of a specific cross section library is possible (see below, Sec.2.3.2).

2.3.2 Impact of cross section library on reactivity

A set of Serpent2 simulations is carried over in order to assess the entity of the impact that cross sections uncertainties have on the reactivity calculations. A comparison between three different libraries is conducted by computing the reactivity level of the system with the Serpent2 model of SUR 100 in its critical configuration. All the run parameters and the features all the model are maintained constant during the comparison, while only the cross section library is varied. In addition, the Thermal Scattering libraries for Polyethylene are not included in this comparison, since they are not embedded by default in the standard libraries.

In Fig. 2.10, where is depicted the comparison among JEFF-3.1.1, JEFF-3.2 and ENDF/B-VII, a substantial agreement between the results produced by JEFF-3.1.1 and JEFF-3.2 is found. On the other hand, if ENDF/B-VII is used, a discrepancy of about 60 pcm arises with respect to the results provided by the JEFF libraries. Such a difference in reactivity is surely significant in biasing the simulated results, but alone is not enough to justify the the 300 pcm shortage in reactivity resulting from calculations. However, together with the aforementioned other sources of uncertainty (geometry and materials), it could reasonably motivate the lower reactivity as computed with Serpent2.

That said, it is important to underline the well-known difficulty in getting absolute evaluation on the reactivity with Monte Carlo transport codes. Even though is not always trivial to

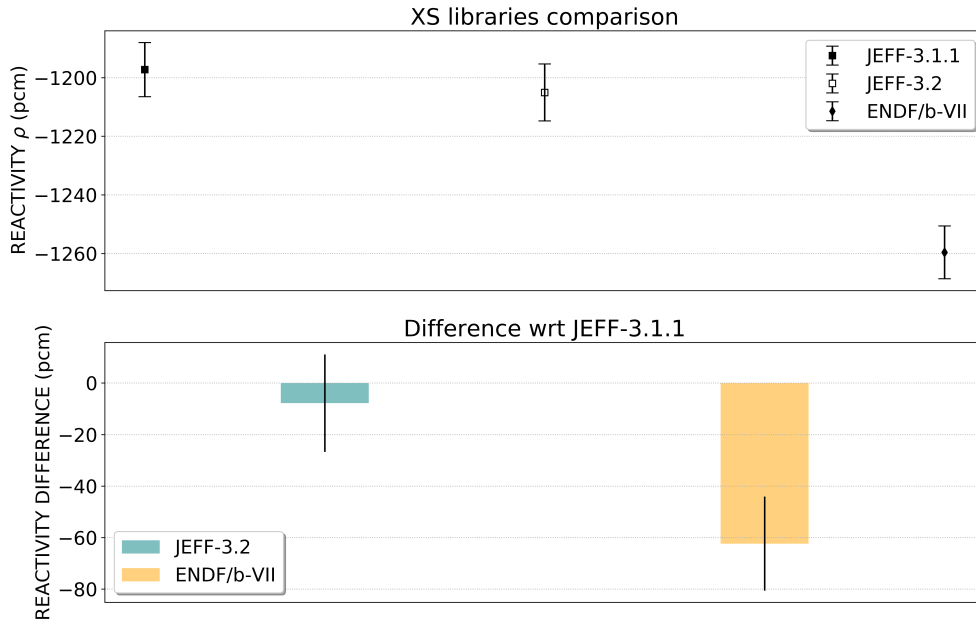


Figure 2.10: Comparison among different cross section libraries in reactivity computations.

obtain the exact value of reactivity of a system in a given configuration, the simulated results remain useful after a proper calibration with experimental data and they still can be used for relative comparison.

2.4 Model validation

This section presents the comparative analysis of the computational results obtained through the Serpent2 model of SUR 100 with some of the experimental results provided by IKE laboratory. The goal of this comparison is to demonstrate the reliability of the computational model in predicting the values of neutron flux of the SUR 100 reactor. To accomplish the objective, some of the experimental data measured by IKE (see Tab. 2.1) are computationally reproduced to perform the comparison.

Table 2.1: Summary table of the experimental data used for the validation of the Serpent2 model. Data are provided by the IKE laboratory.

Experimental data provided by IKE	
Average thermal neutron flux in exp.channel I	$5.6 \cdot 10^6 \text{ cm}^{-2} \text{ s}^{-1}$
Average thermal neutron flux in the core	$4.01 \cdot 10^6 \text{ cm}^{-2} \text{ s}^{-1}$
Maximum thermal neutron flux in core center	$7.1 \cdot 10^6 \text{ cm}^{-2} \text{ s}^{-1}$
Thermal neutron flux at the boundary core/reflector	$2.6 \cdot 10^6 \text{ cm}^{-2} \text{ s}^{-1}$
Thermal neutron flux at the boundary reflector/lead	$3.2 \cdot 10^5 \text{ cm}^{-2} \text{ s}^{-1}$

In computing the results with which the experimental data are compared, a broad use of virtual detectors is made, as they represent a useful tool in every particle transport code. The use of virtual detectors is indeed wide spread in neutronics studies to tally the neutrons reactions in different zones of a reactor. As they score the neutrons interactions in a specific volume

included in the original geometry of the model, the results are not perturbed by effect of self-shielding and flux perturbation due to the presence of a real detector. In case of miniature detectors, being the self-shielding negligible the use of virtual detectors gives results in good approximation with respect to reality. On the other hand, if heavy perturbing detectors are used, the Monte Carlo results obtained with virtual tallies are useful to evaluate the correction factor needed to obtain the unperturbed flux from the detector reading. The main validation results are shown in the following subsections.

Table 2.2: Default 2 groups energy binning - Serpent2.

Serpent2 default 2-groups	E_{min} (MeV)	E_{max} (MeV)
Thermal group	0	$6.25 \cdot 10^{-7}$
Fast group	$6.25 \cdot 10^{-7}$	∞

2.4.1 Average thermal flux in the experimental channel I

The average thermal flux in central experimental channel I is computed with Serpent2 by means of a single-cell virtual detector. The geometry of the virtual detector is chosen to be a square-based prism with a base of 4 cm^2 concentric to the channel. As shown in Fig. 2.11b, it is extended along the core diameter. By means of the ene card of Serpent2, an energy grid was implemented with the detector to discriminate the neutrons according to their energy. The default 2-groups energy grid of Serpent2 (see Tab. 2.2) is used to differentiate between thermal and fast flux. The calculation is carried over for the critical configuration of the reactor, having the control plate 2 lowered to -190 mm and the control plate 1 at its end position.

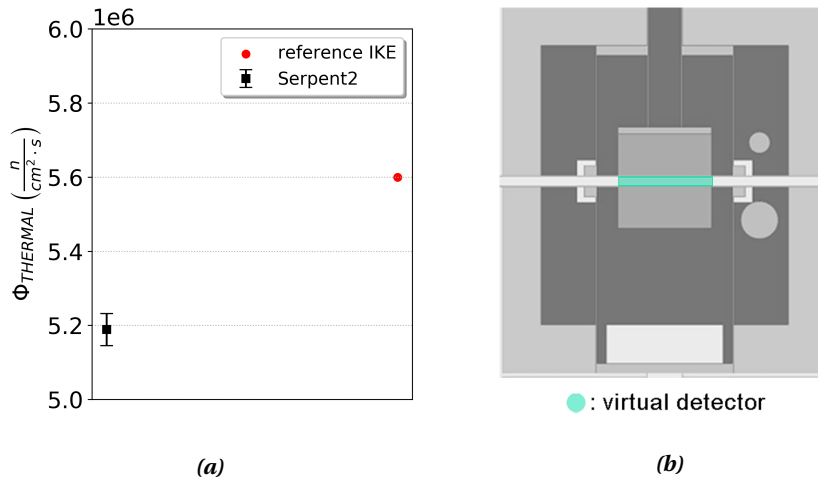


Figure 2.11: (a): Average thermal flux in channel I. (b): Depiction of the virtual detector used for the calculation.

As depicted in Fig. 2.11a, if the calculated results are compared with the reference value provided by IKE, an agreement in the order of magnitude is found, with a difference of -7%. Since the reference data has been provided without its error, it is not possible to determine whether the computed results are in the range of the uncertainty of the experimental one. Nevertheless, it is deemed satisfactory to acknowledge that the Serpent2 computed values can predict the order of magnitude of the experimental data.

2.4.2 Average thermal flux in the core

Another calculation for validation purpose is carried over by computing the average thermal neutron flux in the reactor core. In Serpent2, the task is simplified by using a cylindrical virtual detector encompassing the core volume. Once the same energy grid shown in Tab. 2.2 is applied to the detector, the average thermal flux in the core is computed. Once again, the Monte Carlo simulation is run for the critical configuration of the reactor. As shown in Fig. 2.12, the computed values predict the experimental data, being in the same order of magnitude. Indeed, the overestimation's worth of the computed results is +8%.

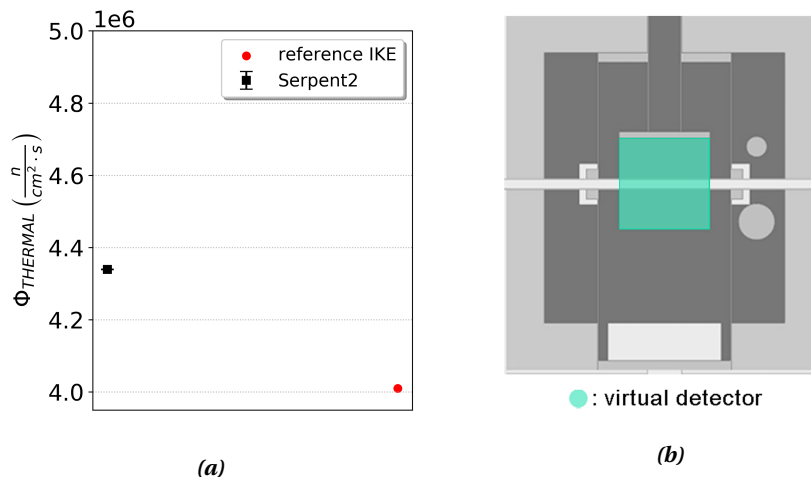


Figure 2.12: (a): Average thermal flux in the reactor core. (b): Depiction of the virtual detector used for the calculation.

2.5 In-core flux perturbation analysis

This section shows the results of a set of calculations performed with Serpent2 to better understand and characterize eventual flux perturbations due to the movement of the Cadmium control plates. The study is focused mainly in the zone of the reactor core and the experimental channel I, to estimate if the movement of the control plates could affect any measurements which takes place in the channel.

To properly study the variation of the thermal neutron flux within the core, a 3D mesh virtual detector is modeled. A total of 60x60 in the x-y plane are defined at a z-level corresponding to the position of the experimental channel. Then, by applying the usual default 2-groups energy grid embedded in Serpent2 (see Tab. 2.2), the thermal neutron flux is tallied in every cell to obtain a flux mapping of the core region. The computation is repeated for different positions of the control plate 2 (CP2), which is moved at different heights. The accuracy of the simulations is chosen to guarantee statistical uncertainties lower than 1 %.

In the 3D plot of Fig. 2.13, which depicts the thermal flux distribution in the core when the control plates are positioned in the critical configuration, it is possible to see a depression of the flux in correspondence of the zone of the experimental channel I. This discontinuity is caused by the filling of the channel, which being air causes a local drop in the neutron population. In addition, also the statistical errors of the computed results inside the central channel are influenced by the presence of air, because of its lower density with respect to the core material.

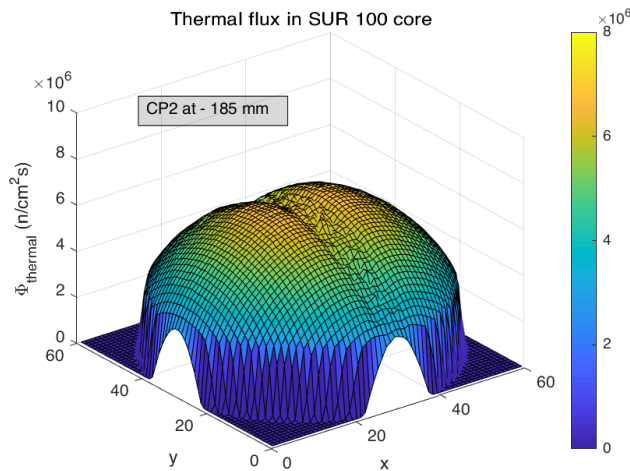


Figure 2.13: Thermal flux map of the core region with the control plates in the criticality position.

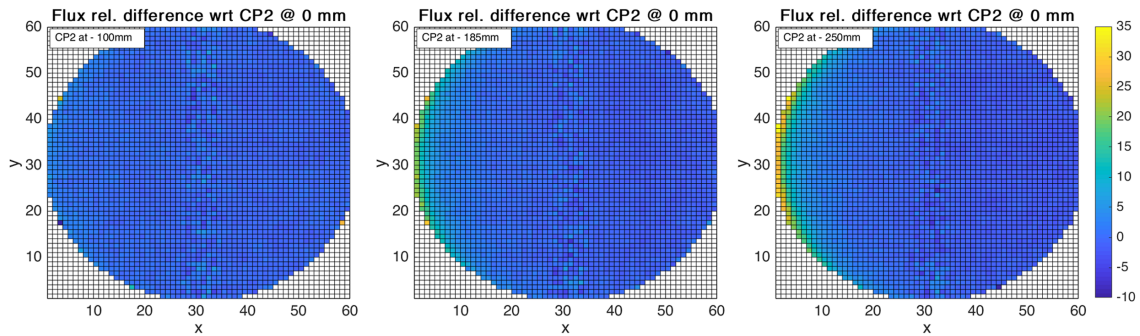


Figure 2.14: Relative differences in flux caused by the movement of control plate 2.

To investigate the perturbation caused by the control plate movement on the in-core flux distribution, a set of calculations are run in order to simulate the start-up procedure. While the control plate 1 is maintained completely extracted, the control plate 2 is progressively removed up to its end position. At every step, the thermal flux map in the core is computed to assess its variation. The results are computed in terms of relative difference with respect to the configuration in which the control plate 1 is at 0 mm and the control plate 2 is at -250 mm.

As can be observed from the evolution of the flux variation map (see Fig. 2.14), the movement of CP2 induces a localized increase in thermal flux, which increases by 30% with the complete extraction of the plate. This perturbation is limited at the core zone directly facing the control plate, and it does not influence the thermal flux within the central experimental channel. This assessment was fundamental in order to understand whether there was possibility to detect any flux perturbation in the central experimental channel caused by the movement of the absorber plates. In fact, the study proves that no information on the plates movement are retrieved by looking at the neutron flux behavior inside the central experimental channel.

2.6 Design simulations for the experimental campaign

A set of Serpent2 calculation was performed as a preliminary step for the experimental campaign, to assess the more interesting aspects to be investigated during the measurements phase. Of course, some of the important details for the reactor configuration (i.e. filling of the channels, power level, critical position of control plates) were in this instance reasonably guessed,

as they were not given before and they depends upon the specific conditions in which the experiment are carried out.

2.6.1 Neutron thermal flux distribution in experimental channel I

A Serpent2 simulation with multiple detectors is run to retrieve the radial neutron flux distribution inside the experimental channel I. The thermal flux is tallied in 500 positions along the channel with the same energy grid reported in Tab. 2.2. The result, which is shown in Fig. 2.15, is computed for the critical configuration of the reactor (i.e. CP1 : -250 mm, CP2 : -190 mm).

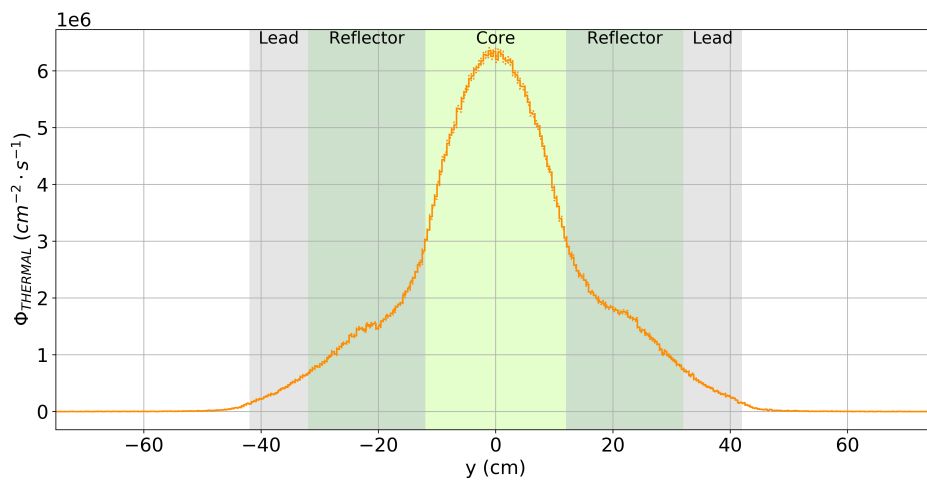


Figure 2.15: Radial distribution of thermal neutron flux in the experimental channel I. Statistical error on the computed data is below 1% in the center of the core.

As it is illustrated in Fig. 2.15, the values of thermal flux inside the experimental channel I are in the same order of magnitude of the reference ones of Tab. 2.1. The effect of graphite on the flux shape is clearly visible in the distribution, where the neutron population locally increases in correspondence of the reflector zone, due to the higher scattering cross section of the material.

An asymmetry can be noticed at the right of the core center, where the flux is 10% higher with respect to the left side. This could be justified with an increase in moderation caused by the presence of the polyethylene filling of the experimental channels II and III (i.e. the cells depicted in magenta in Fig. 2.1a). Further verification on the effect of the presence of the tangential channels are therefore of interest for the work at hand, and are conducted in the following section (Sec. 2.6.2).

2.6.2 Effect of tangential channels on flux distribution in channel I

An additional Serpent2 simulation is run to better investigate the perturbation effects of tangential channels on the flux distribution along the central channel I. The same model used to compute the thermal flux distribution inside the experimental channel I is modified by removing both tangential channels II and III, and replacing the space occupied by them with the materials crossed by the channels themselves.

The computational results, depicted in Fig. 2.16, show a local perturbation in the radial distribution due to the presence of the channels. The local increase of the thermal neutron population is caused by the presence of the polyethylene filling of the tangential channels, which

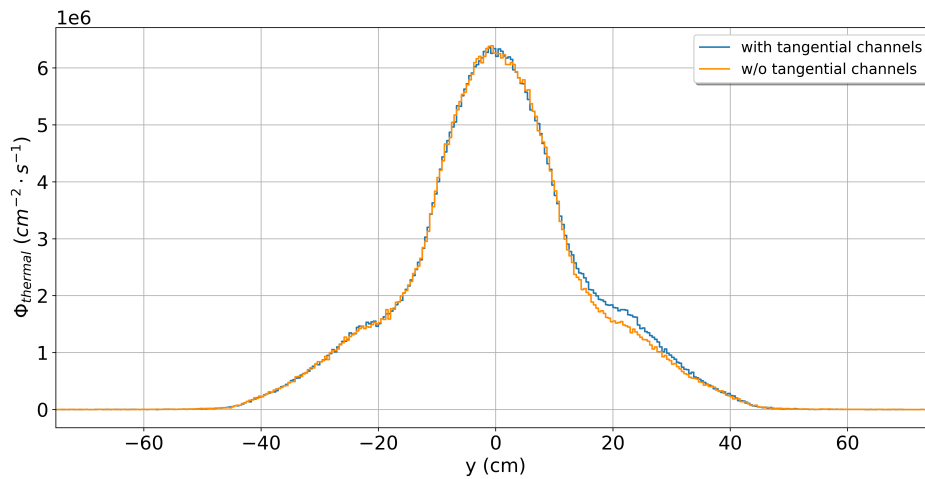


Figure 2.16: Assessment on the perturbative effect of the tangential channels on the thermal neutron flux distribution along channel I. Statistical error on the computed data is below 1% in the center of the core.

adds moderation to the system. The increase in thermal neutron flux is worth 20% with respect to the case without channels. The above mentioned asymmetry found in the radial distribution profile can therefore be explained with the perturbation introduced by the two tangential channels. The statistical uncertainties of the simulated data are omitted in the plot because of their negligible worth, and correspond to less than 1% in the zone of the core center.

2.6.3 Vertical gradient in thermal neutron flux inside experimental channel I

With the purpose of verifying the presence of a vertical gradient in the thermal neutron flux across the experimental channel I, a set of Serpent2 simulations is run. The aim of the simulations was that of explore the possibility of measuring an axial gradient in flux with the insertion of three miniature detectors along the diameter of the experimental channel I.

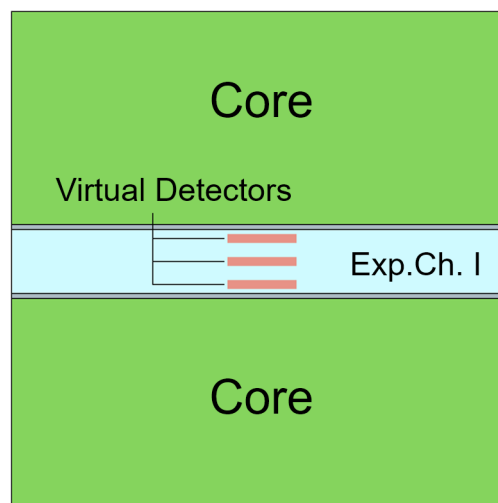


Figure 2.17: Schematic of the modeling of the smeared virtual track-length detectors in Serpent2.

To reduce the computational cost of the simulations, the scintillators are not modeled with

their real size in Serpent2. In fact, virtual track length detectors smeared on bigger volumes are used to achieve a higher accuracy in less computational time. On the other hand, the price to pay by using smeared detectors is the loss of punctual information, since the results obtained with this method are average values over all the detector volume. Bearing this in mind, for the scope of the preparatory simulations here discussed the use of smeared detectors is deemed appropriate.

The virtual detectors deployed for the simulations, which had the same area of the real scintillator screen with a thickness of 2 cm, were placed in the core center along a vertical diameter of the channel. A schematic of how the detector were modeled in Serpent2 is given in Fig. 2.17. Being a preliminary assessment, no holder for the detectors were modeled to eliminate eventual perturbations. The simulations were performed for different degree of aperture of the core gap, with an increasing distance from 0 to 45 mm, which correspond to the maximum core halves separation.

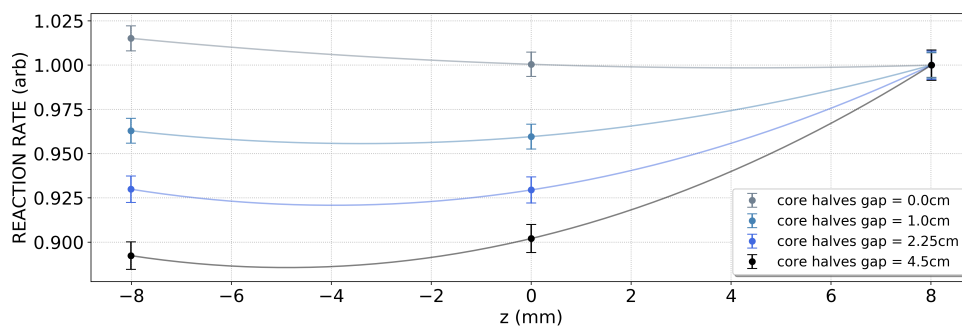


Figure 2.18: Normalized vertical gradients in reaction rates across channel I as computed with Serpent2.

As it is seen in Fig. 2.18 the gradient in reaction rate becomes steeper for bigger displacements of the core halves, due to the increasing amount of air between the bottoming detector and the lower core section. These results prove that the gradient in reaction rate of the neutrons with the lithium of the scintillator screens is almost flat when the core sections are merged together, i.e. when the reactor is in operation. As a matter of fact, the vertical gradient in thermal neutron flux across the diameter of the experimental channel I is small enough to make it very difficult its measurement with the miniature detectors.

2.6.4 Neutron thermal flux distribution tangential channels

Multiple virtual detectors are modeled inside the two tangential channels of SUR 100, namely experimental channel II and III, to calculate the thermal neutron flux distribution along their length. For both the channels, the flux was tallied in 500 positions from -104.2 cm to +104.2 cm, which represent the internal boundaries of the steel tank. The dimensions of the virtual detectors were chosen accordingly to the different diameters of the two channels. For the experimental channel II, i.e. the smaller one, 500 square based prisms of $\sim 10 \text{ cm}^3$ were used, while for the experimental channel III 500 prisms with the volume increased up to $\sim 34 \text{ cm}^3$ were selected. To perform this calculation, the polyethylene filling of the two channel was removed and replaced with air. As shown in Fig. 2.19, the thermal flux distribution has a similar shape in the two channels, with values in the same order of magnitude. As it can be expected, the reflector's effect on the flux shape is no more visible here as it was in Fig. 2.15.

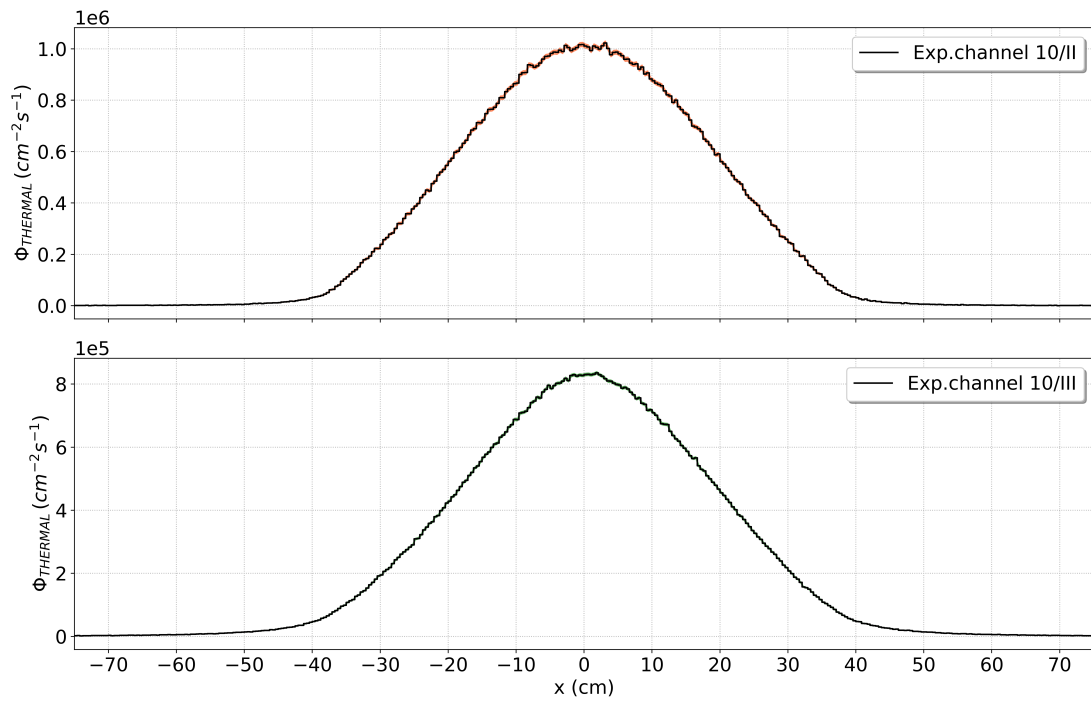


Figure 2.19: Distribution of thermal neutron fluxes along the tangential channels. The shaded area in the plots represent the statistical uncertainty of the computed values, which is below 1 % in the core center region.

3 Testing and characterization of the miniature neutron detection system

As a preliminary step to the experimental campaign in the SUR 100 reactor, the experimental instrumentation was previously tested in CROCUS, a two-zone, uranium-fuelled light water moderated reactor operated by the Laboratory for Reactor Physics and Systems Behaviour (LRS) at EPFL. The reactor core is 1 m high with a diameter of 60 cm, being occupied by an inner uranium oxide region enriched to 1.806% and an outer uranium metal region enriched to 0.947% (both visible in Fig. 3.1). The reactor is controlled by adjusting the level of the moderator, which consists of demineralized light water, or by inserting two B₄C absorber control rods.



Figure 3.1: Picture of the CROCUS core with the experimental instrumentation inserted in the NW control tube for the testing of the detection system.

The objective of the testing was to characterize the miniature detectors in a well-known reference reactor, with low technological uncertainties in terms of materials and geometry. The characterization of the detection system aimed to define the operating parameters and the limitations of the miniature detectors in terms of performances. The tests were particularly focused on the specific objectives listed hereafter:

1. Definition of the Low Threshold (LT) curves of the detectors in CROCUS, in order to de-

- termine a suitable discrimination voltage to cut the background noise;
2. Testing the linear response of the detectors with the power increase of CROCUS;
 3. Testing the dynamic acquisition capabilities of the detection system by recording shut-down transients in CROCUS.
 4. Relative calibration of the miniature detectors by comparison of their count rates under identical conditions in the CARROUSEL facility;

Each of the aforementioned tests, together with a detailed description of the experimental setup, is duly described in the following sections.

3.1 Experimental setup

The experimental instrumentation deployed for the testing in CROCUS consisted in a multiple acquisition neutron detection system, able to collect data from three different neutron detectors at the same time. Indeed, the system allows to locate miniature detectors in several in-core positions without perturbing excessively the local flux. Three of the fiber-coupled scintillators described in [7] have been used as detectors, with minor modifications with respect to the initial design. The read-out electronics used for the signal processing consisted in a mixed digital-analogic acquisition system, able to process in parallel the signals coming from the different detectors.

3.1.1 Detectors configuration

Three miniature neutron detectors have been built appositely for the test, starting from the widely tested prototype described in [2]. Few minor modifications have been implemented in the new design, concerning the scintillator dimensions and the protective aluminum cap. In the first instance, the Scintacor ND2:1 scintillator screen [8] of the prototype has been replaced by an identical one with larger thickness visible in Fig. 3.2. Indeed, the three new detectors are provided with a 280 μm thick scintillator screen (80 μm thicker with respect to the previous one), with a diameter of 1.1 mm. The reason behind the change is mainly due to the availability of three scintillator screens of similar dimensions. In addition, having scintillators with a larger volume allow to increase the number of counts scored by the detector, which can be useful for low power applications such as those for the SUR 100 campaign. Another design improvement for the new detectors regards the aluminum cap, which has been reshaped in a new two-diameters configuration to improve the coupling with the fiber (see Fig. 3.3).

The three miniature detector were positioned altogether in the North-West control tube of CROCUS, in the low-enriched (0.947%) fuel zone of the reactor. A plastic holder mechanically coupled to an aluminum tube, already used in a previous experiment [3], is used to hold the detectors in place. The three detectors have been positioned as schematized in Fig. 3.4, with an angular spacing of 90°. The plastic holder is positioned in the NW control tube of CROCUS such that Fiber 1 and Fiber 3 are aligned along the radius of the reactor. The uncertainty on the azimuthal positioning of the fibers is considered to be 2.5° worth.

The holder tube is provided with a movable plastic element, which allows to position the detectors at several axial heights. For this experiment, the holder was positioned such that the tips of the aluminum caps are located (50 ± 0.1) cm from the bottom of the fuel elements.



Figure 3.2: Picture of the front-end of the detector. The scintillator is visible as the aluminum cap is here removed.

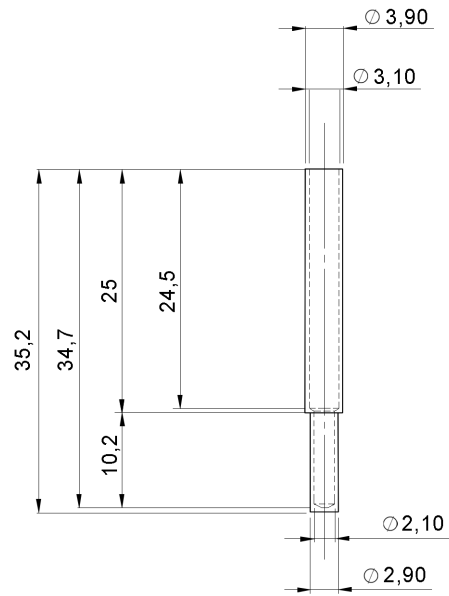


Figure 3.3: Scheme of the aluminum cap.

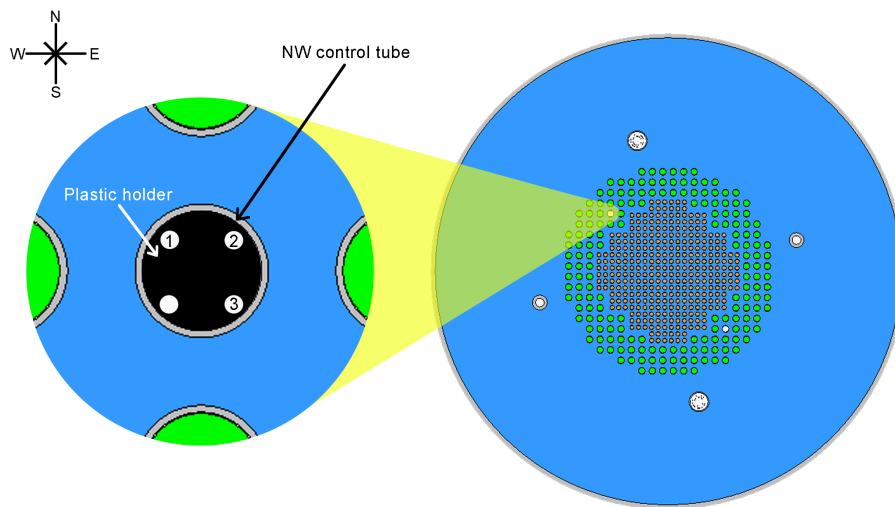


Figure 3.4: Scheme of the positioning of the three fibers in the NW control tube of CROCUS.

3.1.2 Read-out electronics

The mixed read-out electronics used for the tests is schematized in Fig. 3.5, and consists of both commercial and in-house components, designed at LRS. The function of the read-out system is that of processing the light signal produced by the scintillator in case of interaction with neutrons, by making it more easily readable through its conversion and amplification. An accurate description of the components used for the testing activities is given in the following paragraphs.

Silicon Photomultiplier A Silicon Photomultiplier (SiPM) is a solid state photodetector composed of a matrix of Avalanche Photodiodes (APDs) working in Geiger region. The SiPM receives the light photons generated by the scintillator screen in the interaction with neutrons

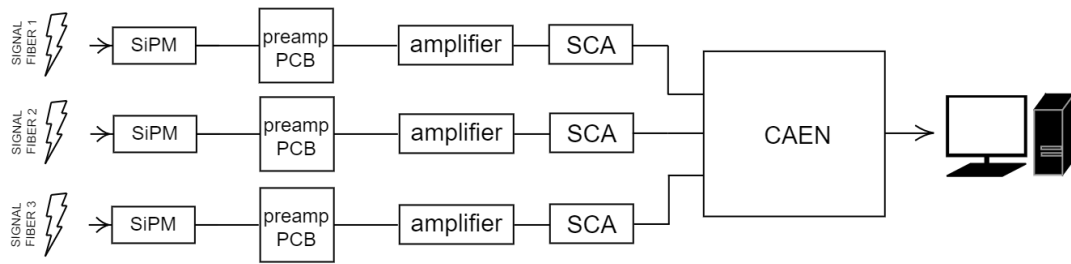


Figure 3.5: Scheme of the read-out electronics used for the testing.

and produces tension pulses. The amplitude of the pulses, which is discrete, depends on the number of APDs triggered by the incoming photons and on the bias voltage applied to the SiPM. The correct value for the bias voltage, determined by looking at the output signal of the SiPM, was chosen to be 56.5 V. The SiPM, which has to be kept in dark to be shielded from background light, was enclosed in a manufactured aluminum tube (see Fig. 3.6).

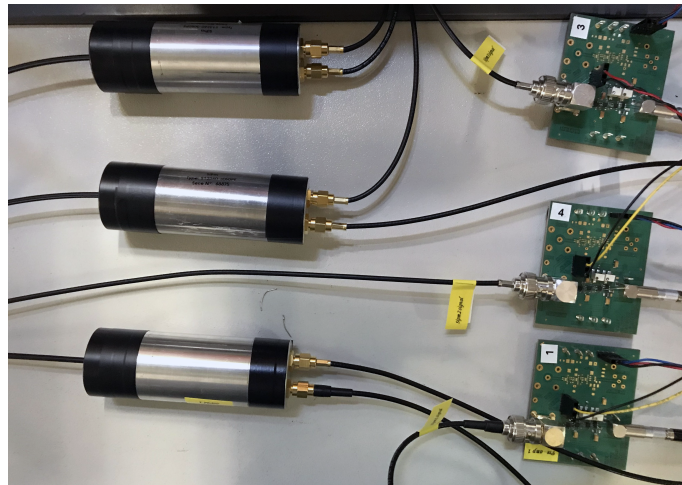


Figure 3.6: Picture of the SiPM aluminum tubes (on the left) connected to the PCBs (on the right).

Preamplifier + first discriminator PCB The Printed Circuit Board (PCB) manufactured by the technical division of the LRS laboratory consists in a preamplifier and a first discriminator. Its function is to amplify the voltage signals coming from the SiPM and to discriminate them by cutting-out those whose amplitude is lower than a manually selected threshold. The offset level of the signal is manually adjustable by turning the apposite screw shown in Fig. 3.7 until the output signal (visualized through an oscilloscope) has his minimum in correspondense of the zero. The threshold level is instead tuned analyzing the signal in output from the amplifier stage of the PCB (visualized in the oscilloscope through a probe). Given the discrete nature of the signal in output from the SiPM, also the pre-amplified signals show discrete amplitudes. In the work at hand, it was selected the value of 1.6 V to cut-off lower signals, enlarging the linear operational range of the detectors. The PCB preamplifiers needs to be powered by two voltage supplies, of 2.5 V (for the amplification stages) and 3.3 V (for the discriminator stage).

Gaussian amplifier The output signal from the preamplifier is then processed through a CANBERRA 2022 Gaussian Amplifier. The component integrates over time the square pulses coming from the preamplifier and produces a voltage signal of few volts. The amplitude of the signal depends on the density of the train of square pulses from the PCB. If background photons in-

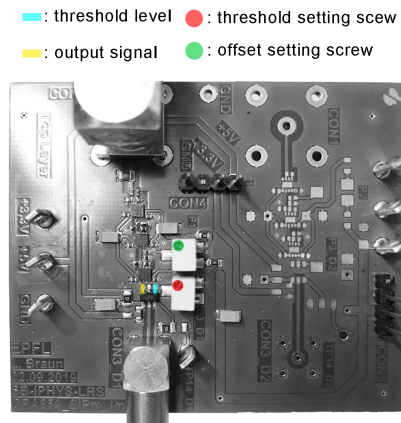


Figure 3.7: Preamplifier + First discriminator PCB designed by the technical division of LRS.

interact with the detector, and the signal generated by the SiPM is high enough to pass through the first discriminator stage, a single square pulse is generated by the preamplifier. On the contrary, if a neutron interaction happens, a high-density train of pulses is generated (see Fig. 3.8). The amplitude of the signal depends also on the gain, which can be selected manually together with the integration time (“shaping time”). For the tests at hand, a shaping time of $0.5 \mu\text{s}$, a coarse gain of 10 and a fine gain of 0.3 were used. With these settings, an amplified signal of $1.3 \mu\text{s}$ width and 1 V amplitude is generated for a neutron interaction.

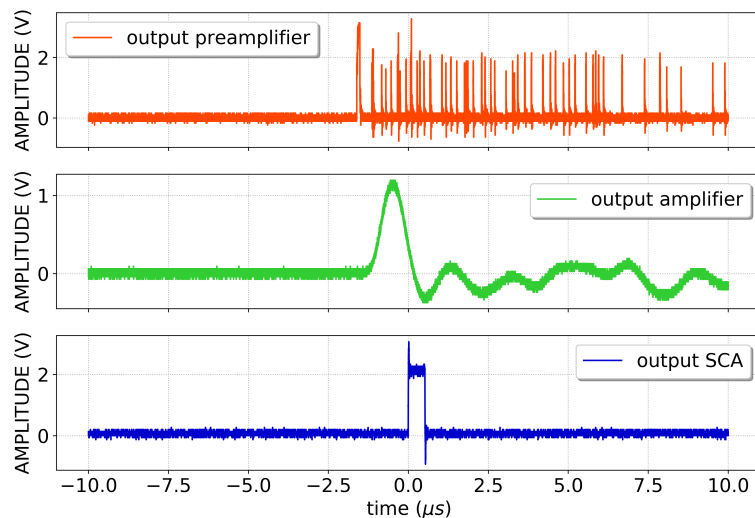


Figure 3.8: Signals in output from different stages of the read-out electronics chain.

Single Channel Amplifier (SCA) A CANBERRA 2030 SCA was used to perform the second discrimination stage on the output signal from the amplifier. The SCA produces a square pulse (see Fig. 3.8) only if the input signal is higher than a manually set threshold. The determination of the Threshold level is performed by building the Low Threshold curve (see Sec.3.2).

Digital multichannel counter In the present work, the count of the square pulses produced by the SCA corresponding to the number of detected neutron events, is performed by a Field Programmable Gate Array (FPGA) produced by CAEN [20] used in this framework as a multichannel digital counter. The settings of the digital counter can be adjusted in dependence of

the time scale of the phenomenon that one wants to observe. It is indeed possible to configure the counter for “fast” transient by reducing the acquisition time of the events count. This possibility enhance the deployability of the system also for recording of shutdown or start-up transients. In addition, by means of the CAEN system the parallel acquisition of three different channels is much more straightforward with respect of having three different analog counters.

3.2 Low Threshold curves

The first of the tests in the CROCUS reactor was carried over to define the correct discrimination level for the Single Channel Analyzer, which is determined through the construction of the so-called Low Threshold, or LT, curves. An LT curve is obtained by recording the variation of the count rates of the detectors while the threshold level of the SCA is varied.

In the case at hand, all the detectors were positioned in the NW control tube of CROCUS as shown in Fig. 3.4. While the reactor was maintained critical at a power of around 130 mW, different measurements were executed by varying the level of threshold voltage in the range from 0 up to 1 V. Given the physiological oscillations of the reactor power level in time, its power history has been recorded during the measurements by two ex-core monitor fission chambers (named in the work at hand as Monitor I and II). To eliminate effects of variation in counts caused by oscillations in power, the measured count rates for each value of the SCA threshold level are normalized by the average number of counts recorded by the monitors during each respective measurement. The results are shown in Fig. 3.9.

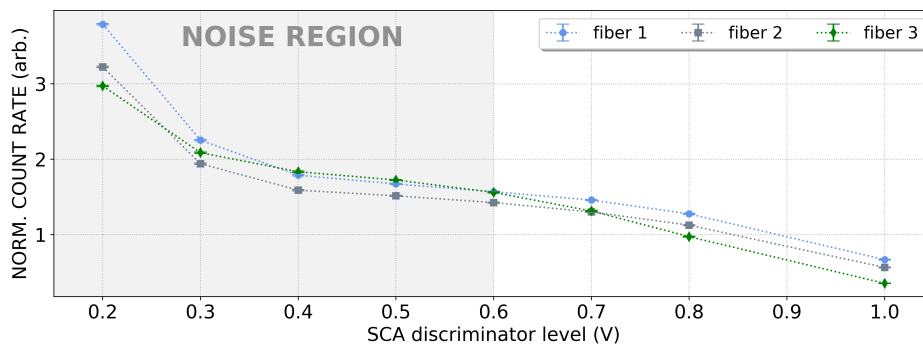


Figure 3.9: LT curves for each of the three detectors used in the testing.

While increasing the threshold level, the count rates of the three detectors are observed to decrease down to a point in which all the background noise signals are excluded, as they are not high enough to exceed the threshold. This value is selected to be the optimal level for the SCA threshold, since it allows to exclude the unwanted background noise from the acquisition. On the other hand, if the threshold is further increased the count rates of the detectors drop dramatically, as the discrimination level becomes too high to be reached by the amplitude of the signal caused by neutrons. Therefore, based on the results obtained with this test, a value of 0.6 V is deemed to be appropriate for the second discrimination stage.

As it is seen from Fig. 3.9, the three miniature detectors show different count rates. The differences in counting are caused by two factors. The first one is the location of the three detectors, which being in three different positions measure three different level of neutron flux, as demonstrated in [3]. In addition, the difference in count rates is caused also by the different sizes of the scintillator screens of the three miniature detector. Indeed, as shown in Sec.3.5, even minimal discrepancies in the scintillators dimensions cause relevant changes in the acquisition capabilities of the detectors.

3.3 Linearity response in CROCUS

The linearity of a detector is related to its capability to provide an output proportional to the received radiation rate. It is then fundamental to define the operational limits within which the miniature detectors are able to provide a linear response.

To accomplish this task, different measurements are performed in CROCUS while increasing the reactor power to several levels. At each power step, the count rate is recorded for each fiber by using the detection system shown in Fig. 3.5. The actual reactor power level of each measurement was retrieved from the counts recorded by the two monitor fission chambers, through calibration factors measured in a previous work [21]. In this way, the power evolution can be averaged in time to determine a single power level for each measurement. The results of the linearity tests, which are computed considering the power reading of the monitor I, are shown in Fig. 3.10.

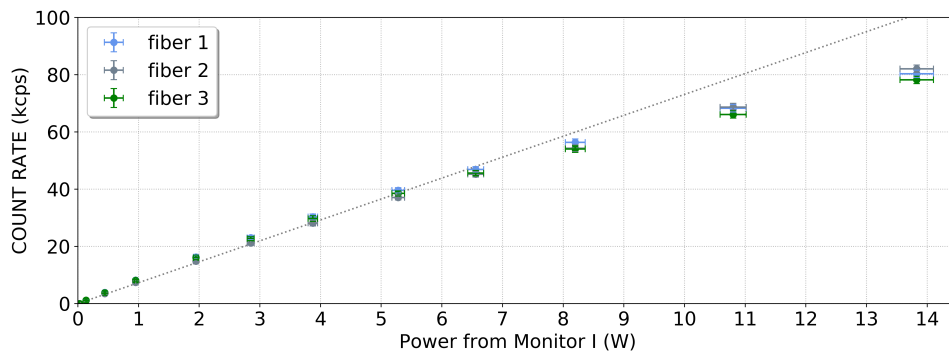


Figure 3.10: Linearity curves for each of the three detectors used in the testing.

The experimental results prove that the linearity of the three detector is ensured up to a power of about 6.5 W corresponding to a count rate of about (46 ± 1.0) kcps for the miniature neutron detectors. Beyond this point, the departure from linearity of the count rates begins due to dead-time effects of the three detectors.

3.4 Shutdown transient acquisition

To test the dynamic response of the detectors during a transient, the shutdown of CROCUS is recorded. By configuring the CAEN digital counter through the PC, the acquisition time of the system was reduced down to 10 ms, in order to be able to observe the decrease in count rate with a proper time discretization. A measure is performed while the reactor is shut down from an initial power of 5.6 W.

The results are shown in Fig. 3.11, in which are compared the data acquired by the miniature detector named “fiber 1” against those recorded through the monitor fission chamber 1. As depicted, through the fiber-coupled scintillators is possible to obtain a very detailed characterization of the shutdown transient in time. Indeed, by means of the digital counting device, it is possible to increase the acquisition rate up to values which are satisfactory for the investigation of time-dependent phenomena on such a fast time scale.

The oscillations of decreasing amplitude following the power drop are caused by local perturbation of water in CROCUS, since the shutdown is performed by removing the moderating material (i.e. water) from inside the core.

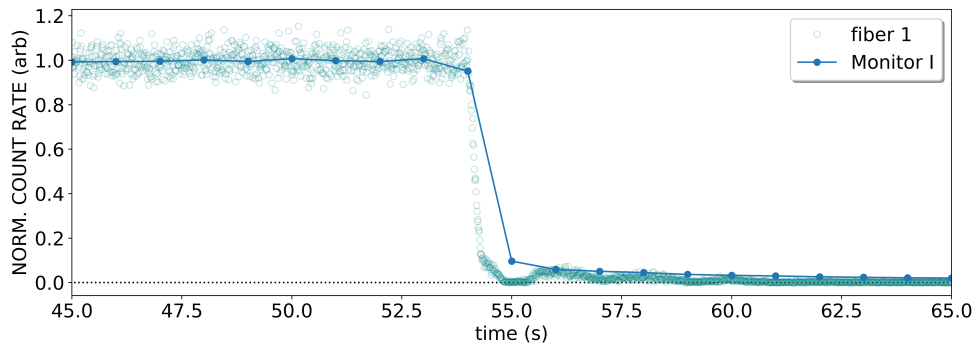


Figure 3.11: Dynamic measurement of the shutdown transient in CROCUS.

3.5 Calibration in the CARROUSEL facility

From the plots of Fig. 3.9 and Fig. 3.10 it is clearly noticeable a difference in count rates for the three miniature detectors. As already mentioned above, this discrepancy is caused by the different locations of the three detectors and the different scintillator sizes. As can be seen in the picture of Fig. 1.13, the scintillator shape is not regular and can differ from one detector to the others. Even small discrepancy in scintillator can cause discrepancies in the photons yield and therefore discrepancies in the number of counts. To isolate the effect of the scintillator size on the count rate and to assess quantitatively its impact a test in the CARROUSEL facility is performed.

CARROUSEL consists in a PuBe neutron source immersed in a large tank of water, used in LRS both for detectors characterization and teaching purposes. Through apposite instrumentation, detectors can be placed in the water tank at different distances from the center, where the neutron source is located.

For the test at hand, the detectors are positioned 12 cm far from the radioactive source, and maintained in position for the time needed to collect results deemed statistically significant (≈ 2 hours to obtain a relative error on the number of counts $< 0.3\%$). The test is repeated three times, using only one detector at once.

Table 3.1: Results of the detectors calibration in the CARROUSEL facility.

	Count Rate (s^{-1})	% wrt Fiber 1
Fiber 1	15.18 ± 0.04	-
Fiber 2	12.24 ± 0.03	$80.6 \pm 0.3\%$
Fiber 3	13.90 ± 0.03	$91.6 \pm 0.3\%$

The results of the comparison, which are summarized in Tab. 3.1, show that a difference is present between the acquisitions of the three detectors, as the fiber 2 and 3 measure a count rate respectively 19.4 and 8.4 % lower than the fiber 1. A possible motivation behind this could be the difference in the geometry of the scintillators. Indeed, given their very small dimension, even a tiny variation in the shape can cause a different sensitivity in their interaction with neutrons. Thanks to this verification, if a measurement of the reaction rate gradient is made, the outcome could be corrected according to the relative difference in counting on the three detectors.

4 SUR 100 experimental campaign

An experimental campaign for the SUR 100 reactor was scheduled by means of an academic collaboration established between the LRS laboratory at EPFL and the IKE laboratory at University of Stuttgart. The campaign, which took place in the week between July 13th and July 17th 2020, was focused on the testing of the miniature detectors in a different experimental reactor and on the characterization of its neutron thermal flux distributions in locations of interest.

The use of the miniature detectors for the measurements within the channels of the SUR 100 reactor was deemed particularly of interest. Indeed, the miniature dimensions of the detectors developed at EPFL allowed measurements not easily achievable with standard-size detectors. The main issue connected with the use of conventional neutron detectors concern their dimensions, since most of them have an active volume too large to allow for high-spatial resolution measurements, and therefore not suitable for neutron flux profile characterization in experimental reactors.

4.1 Aim of the campaign

The objectives of the experimental campaign mainly concerned the thermal flux characterization of the SUR 100 reactor through the use of miniature detectors in innovative arrangements. Steady-state and dynamic measurements were carried over in order to characterize the thermal neutron flux of the reactor and its response to reactivity insertion.

More in detail, the goals of the experimental campaign were:

- Measurement of the radial thermal neutron flux profile along the central experimental channel I and its comparison with neutron activation measurements;
- Measurement of the thermal neutron flux profile along the tangential channel II;
- Measurement of the gradient in thermal neutron flux across the diameter of the experimental channel I (vertically) and II (horizontally);
- Measurement of the reactor periods due to the extraction of the control plate 2 and retrieval of the reactivity curve;

All the measurements carried over during the campaign were meant to be compared with Serpent2 results, to assess the validity of the developed model.

4.2 Experimental setup

The same experimental setup used for the CROCUS testing (described in Chap.3) was deployed for the SUR 100 campaign. Dealing with different experimental channels, only the mechanical holder used to keep the fibers in position was substituted.

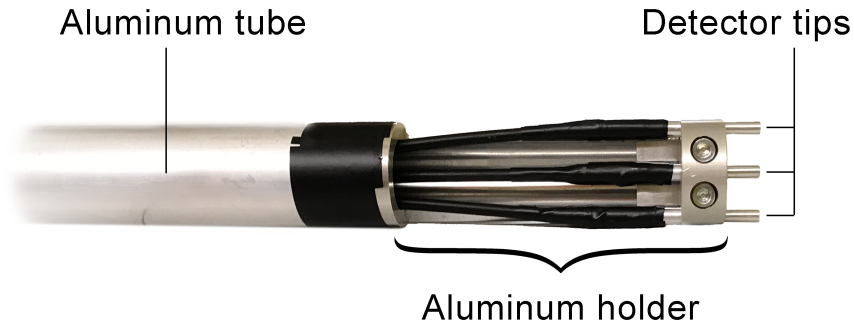


Figure 4.1: Aluminum positioner used for the experimental campaign in SUR 100.

An apposite Aluminum holder was manufactured by the technical division of the LRS laboratory. The front-end of the holder (see Fig. 4.1) has a diameter of 26 mm, i.e. the same of the internal diameter of the experimental channel I within the technological tolerance limits, and it is provided with three housings for the detectors tips. Given the difference in diameter of the experimental channels, the diameter of the holding tube had the possibility to be adapted to a larger diameter (54 mm) by means of apposite aluminum spacer rings. The tube was equipped with a manufactured ruler, that was taped on the aluminum surface in order to determine the detectors' position inside the channels. The choice of aluminum for the holding equipment was straightforward, given its small influence on thermal neutron flux, its availability and its low neutron absorption cross section and rapid decay of the induced activity [22].

In order to move the detectors along the experimental channels, the front-end holder was mechanically coupled to a graduated aluminum tube manufactured by the IKE laboratory. The tube was equipped with a handle that allowed to adjust the angular orientation of the detectors inside the experimental channels. Depending on the experiment, the tube was slid into the channels with one of the possible configurations shown in Fig. 4.2. The number of the detectors used was varied in dependence of the needs of each experiment. In most of the experiments, one of the miniature detectors (fiber 2) is removed from the holder and used for power monitoring. Further details on how the measurements were performed are given in the dedicated section of each experiment of this chapter.

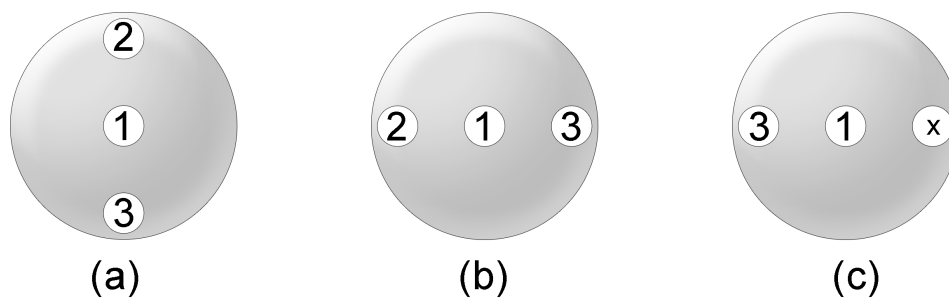


Figure 4.2: Different positioning of the detectors inside the experimental channels of SUR 100.

Given that the movement of the detectors was performed manually at different positions

inside the experimental channels of SUR 100, all the experimental results are affected by positioning uncertainties. In addition, another uncertainty source was represented by the graduated ruler of the aluminum tube. It is therefore reasonable to take into account the positioning errors altogether in a unique uncertainty, worth $\Delta x = 2$ mm.

4.3 Preliminary verifications

The first measurements performed in SUR 100 were meant to verify the correct functioning of the detectors in terms of configuration of the read-out electronics. To perform the test, the Low Threshold curves and the Linearity curves are retrieved for the three detectors in the same way they were measured in CROCUS (see Chap.3). The results of the verification are shown in the following paragraphs.

Low Threshold curves As already done in CROCUS, the LT curves are retrieved also in SUR 100. The three detectors, positioned altogether by means of the Aluminum holder in the experimental channel I in correspondence of the core center, are aligned vertically in the configuration (a) schematized in Fig. 4.2 (i.e. fiber 1 at the center, fibers 2 on top and fibers 3 at the bottom). Several SCA threshold levels are tested, and for each one the count rate measured by the three detectors is recorded. To minimize the influence of physiological power fluctuations on the results, the count rates obtained are then normalized by the sum of counts recorded by one of the monitor detectors of SUR 100 in the interval of time of each measurement. A threshold value of 0.6 V is chosen to be optimal for the configuration at hand, since all the noise region is cut-off from the signal (as shown in Fig. 4.3).

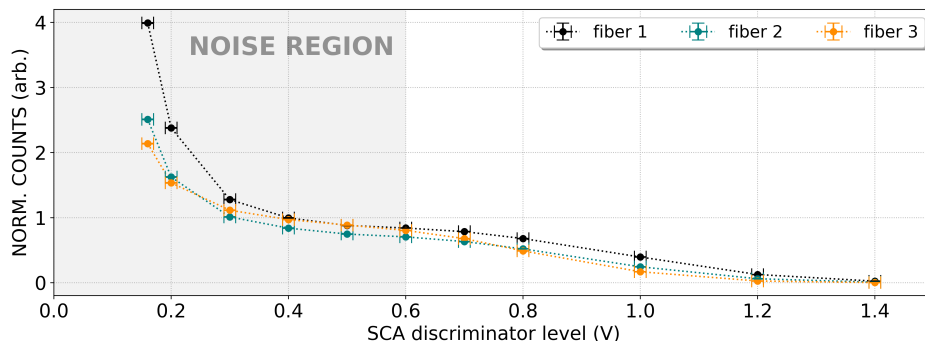


Figure 4.3: LT curves measured in the SUR 100 reactor.

The threshold level of choice it is consistent to the one resulting from the testing in CROCUS before the experimental campaign.

Linearity response check The linearity of response of the miniature detectors, already tested in CROCUS, is checked again in SUR 100. Maintaining the detectors in the same configuration used for the LT curves, i.e. configuration (a) of the holder positioned in the core center, measurements are performed with the reactor critical at different power levels from 4 to 340 mW. The three miniature detectors did not show saturation effects, being the maximum count rate measured about 20 kcps lower then the critical linear limit tested in CROCUS (see Fig. 3.10).

As Fig. 4.4 shows, the linear interpolation of the experimental data reveals that the linear response of the detectors is guaranteed for all the power levels, exception made for the first two low-power measurements. Since a loss of linearity could not be explained at such low powers (4 and 23 mW), the explanation of this non-linearity should be found in the monitor power reading, which could be erroneous for the first two points recorded by the measurements.

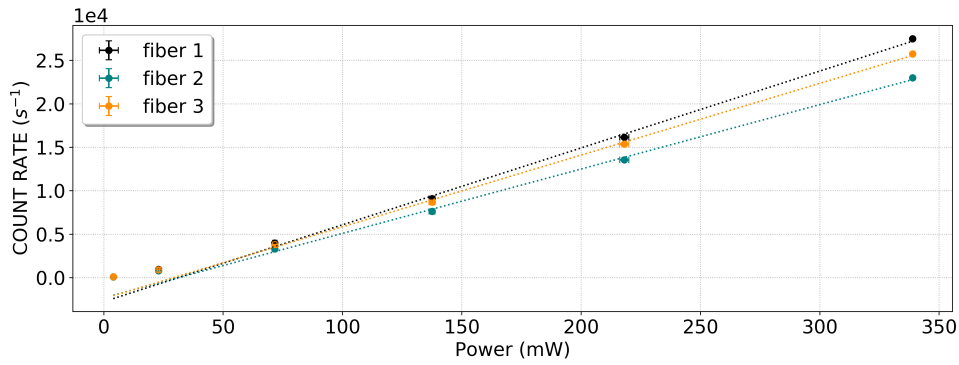


Figure 4.4: Linearity curves measured in SUR 100 for the three neutron detectors.

In any case, since the operational level of SUR 100 at which all experiments are carried out is on much higher powers, this low power effect is not considered an issue for the objectives of the campaign. Moreover, given that the testing of the linear response of the detectors in the CROCUS facility has demonstrated good results (see Sec. 3.3), the linearity of the detectors is assumed to be proved.

4.4 Neutron thermal flux profile along channel I

Given the difficulty to fit conventional neutrons detector inside small orifices, in the case of the central experimental channel of SUR 100 the miniature detectors were considered particularly suitable to measure the thermal neutron flux profile along its length. Indeed, the only measurements available for the thermal neutron flux inside the central channel in SUR 100 were obtained through the activation of Mn-56 samples (see Sec.4.4.3). Such kind of measurements are inherently affected by flux disturbance effects and do not allow to retrieve the correct neutron distribution within the experimental channels without the use of correction factors. To demonstrate their effectiveness in measuring the flux profile distribution in the central experimental channel of SUR 100, the results obtained with the miniature detectors are shown and compared with the ones obtained through neutron activation technique.

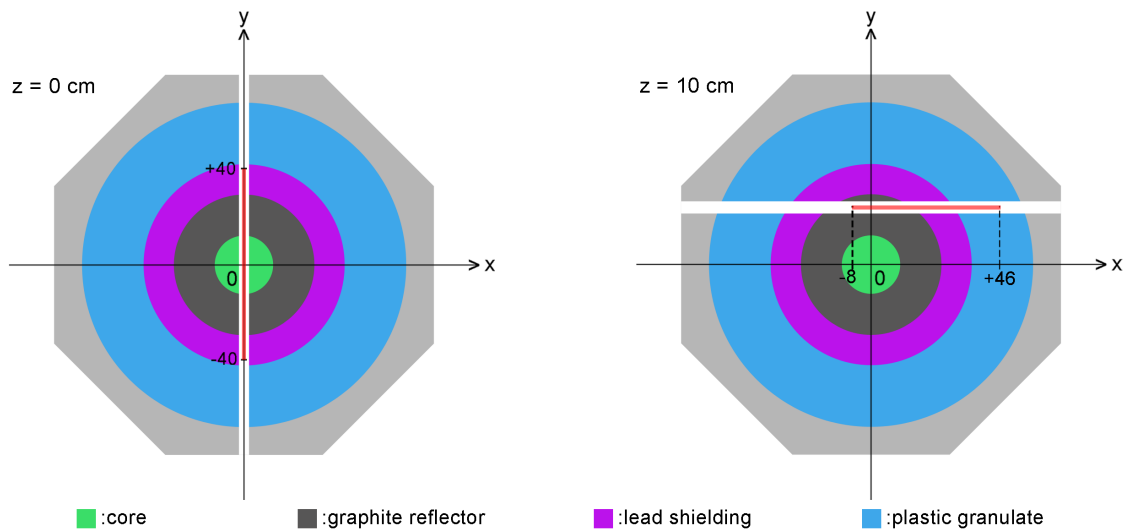


Figure 4.5: Simplified schemes of the profile measurements inside channel I (left) and channel II (right). The red lines indicate the spatial range in which measurements are performed.

4.4.1 Profile measurement

The goal of the measurement was to score the count rate recorded by the miniature detectors at several positions inside the central experimental channel, in order to retrieve the shape of the thermal flux.

To accomplish the objective, the miniature detectors named “fiber 1” and “fiber 3” are positioned inside the channel through the aluminum tube in the configuration (c) of Fig. 4.2, while the “fiber 2” is maintained at a fixed position along the whole duration of the measurements in the tangential channel II to be used as a power monitor. Thus, the two detectors in the central channels are moved along its length to retrieve the reaction rates at several positions. An explanatory scheme of how the measurement was performed is provided in Fig. 4.5.

Count rates are recorded at several positions in a spatial range between -40 and +40 cm far from the core center, for the time necessary to have statistical errors in the order of 0.1%. Further details on the method with which errors on the measured data are computed are given at the end of this subsection in the dedicated paragraph. The results of the measurements recorded by “fiber 1” are depicted in Fig. 4.6. The count rates recorded by the detector are normalized twice. A first normalization, performed dividing the counts of the “fiber 1” by the reading of the monitor “fiber 2”, is meant to reduce the sensitivity of the measurements to the power oscillations of the reactor. The measurements are then normalized again by the maximum measured value.

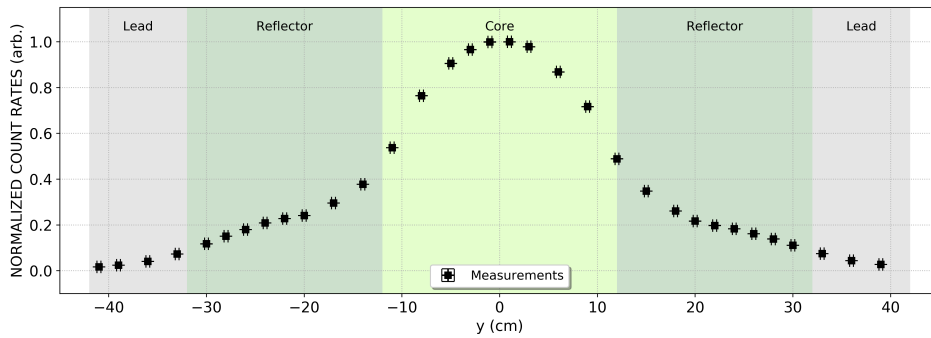


Figure 4.6: Count rate distribution measured by fiber 1 in experimental channel I.

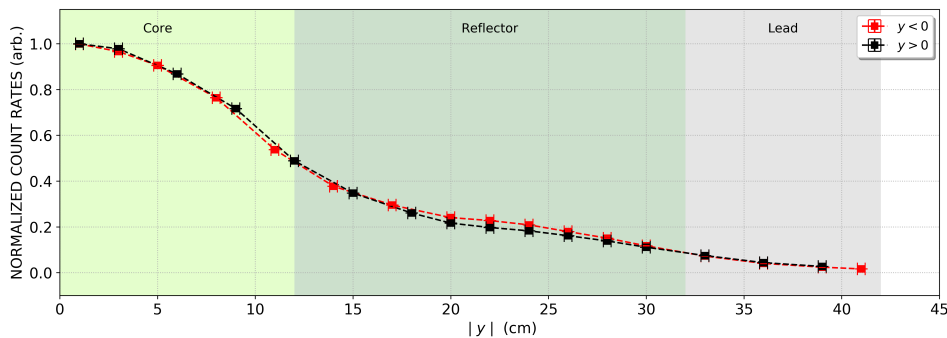


Figure 4.7: Symmetry check on the measured count rate profile along channel I.

As depicted in Fig. 4.7, the profile is symmetric with respect to the core center, given the overall agreement of the data measured on each side of the core. A slight difference is found to

exist between the points lying in the interval from 20 to 28 cm far from the core center, with a disagreement in the order of 10%.

Counting statistics To evaluate the statistical error on the count rates, a peculiar property of the Poisson distribution is used. As it is widely known in counting statistics, if the measurement time of a nuclear process is short compared to the half-life of the radioactive source, the Poisson distribution describes the expected variance of the data as if the identical measurement was repeated many times [12].

$$P(n) = \frac{[E(n)]^n}{n!} e^{-E(n)} \quad (4.1)$$

The analytical formula which describes the probability to observe a given number of counts n in a Poissonian process is given in Eq. 4.1. In this case, the expected value $E(n)$ represents the number of counts obtained during a single measurement. Considering that for a Poisson distribution the variance of the data coincides with the expected value, it is possible to retrieve the standard distribution as the square root of the number of counts (Eq. 4.2).

$$\sigma_{counts} = \sqrt{N_{counts}} \quad (4.2)$$

Thus, from Eq. 4.2 is possible to compute the necessary number of counts to achieve the desired level of accuracy.

4.4.2 Comparison with simulations

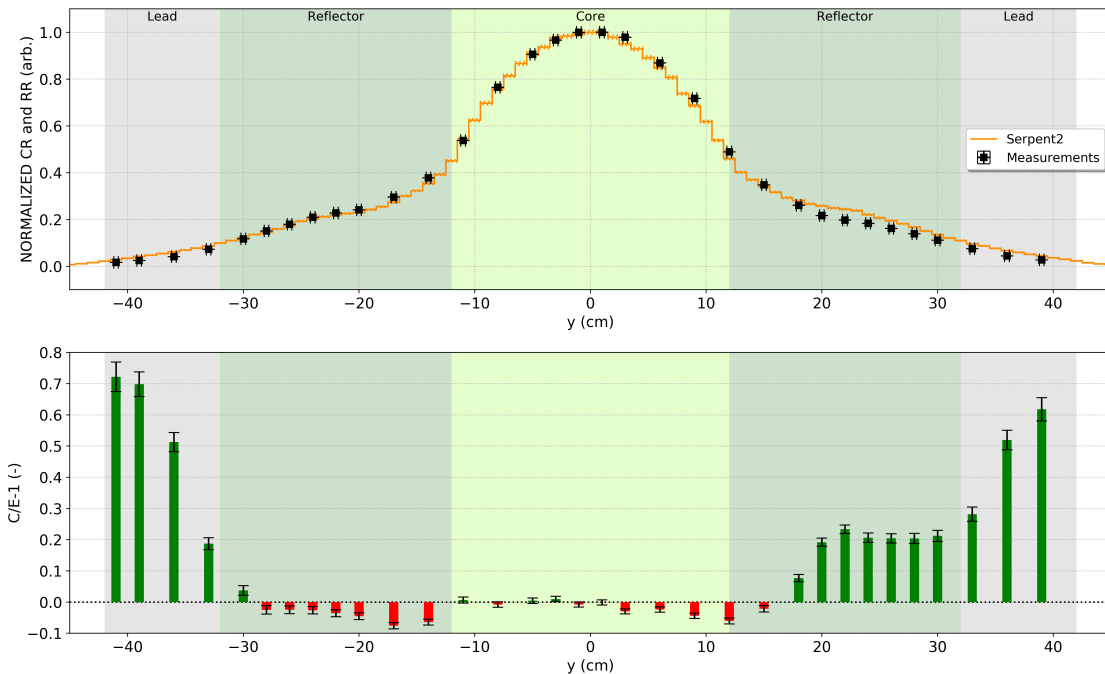


Figure 4.8: Comparison of experimental count rates against ${}^6\text{Li}$ reaction rates predicted by simulations along experimental channel I.

The measured data are then compared with computational results obtained through the Serpent2 model. The real configuration of the reactor (i.e. power level, control plates position and filling of experimental channels) of the day of the measurement is implemented in

the computational model, in order to reproduce the reality as faithfully as possible. Cylindrical virtual detectors with the same radius of the channel (26 mm) and a thickness of 1 cm are used to score the neutrons reaction rate with the Lithium of the scintillator in every cm of the experimental channel in the range [-45;45] cm. The modeling of real-size detectors, given the tiny dimensions of the scintillators, was deemed to be unnecessary for the scope of the work at hand. Indeed, simulating real-size scintillator would cause a significant increase in the computational cost of the simulations, given the lower occurrence of neutrons interaction with a much smaller volume. Despite this, the smearing of the detectors is expected to introduce a discrepancy with the measured data, since the Monte Carlo results are in this way averaged on larger volumes. A depiction of the comparison of experimental and simulated data is given in Fig. 4.8.

The experimental results are seen to be particularly in agreement with the simulated data in the spatial range [-30,18] cm, with a $C/E - 1$ value lower than 10%. An asymmetry in the radial profile is found in the zone of the graphite reflector between +20 and +30 cm away from the core, and it is not foreseen by the simulations. This discrepancy, which causes a disagreement of about 20%, could be caused by localized change in material composition or some geometric asymmetry not considered in the computational model. Further away from the core center, a higher discrepancy is found to exist symmetrically from 30 to 40 cm, with a $C/E - 1$ value that reaches about 70%. Given the presence of the lead shielding in the zone of highest disagreement, such a discrepancy could be motivated with the uncertainties in material composition or in its cross section.

4.4.3 Comparison with activation profile

An additional measurement of the thermal flux profile inside the central channel was obtained during the SUR 100 campaign with a neutron activation experiment. The flux profile was retrieved by measuring with a High-Purity Germanium (HPGe) semiconductor detector the gamma-radiation emitted by some Manganese samples irradiated in the reactor central channel for about 45 minutes.

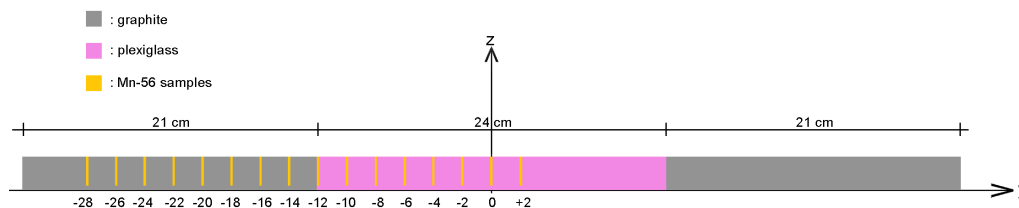


Figure 4.9: Scheme of the holder used for the activation experiment.

For the experiment, an apposite cylindrical holder (see Fig. 4.9) with the same radius of the experimental channel (13 mm) was used to position 16 samples of ^{55}Mn inside the reactor core. The used samples, consisting in tiny cylindrical rods of equal diameter with a length varying from 16.6 to 18.0 mm, were located in the 2 cm spaced housings of the holder. The stable ^{55}Mn isotopes interact with thermal neutrons because of the following neutron capture reaction:



which activates the samples. Of course, the activation of the sample is proportional to the thermal neutron flux which it has to withstand, and therefore the outermost samples will be weakly activated with respect to the one in the core center. The activity of the samples is due to the

decay of the ^{56}Mn nuclides, that are transformed into various excited states of ^{56}Fe according to the β^- reaction of Eq. 4.4.



The excited Iron nuclides arising from the decay, can assume three different energy levels before reaching ground state via γ -decay (see Fig. 4.10).

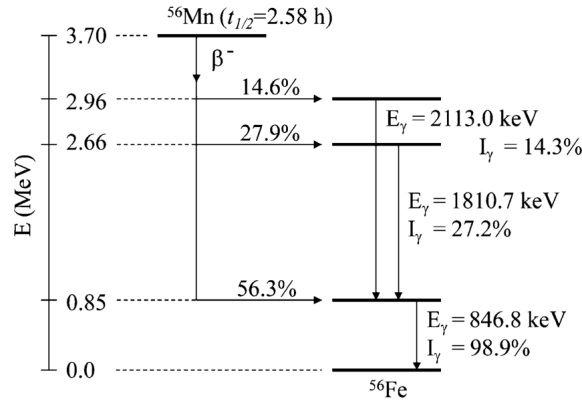


Figure 4.10: Decay path of the Mn-56 nuclides through different excited states of Fe-56 [23].

Thanks to the high resolution of the HPGe detector, an accurate gamma-spectroscopy of the samples is performed after the irradiation. Thus, the count rate produced by gamma radiation in a specific Region of Interest (ROI) of the spectrum (i.e. 846.8 keV) clearly indicates the level of activity of each sample. By means of the radioactive decay law (Eq. 4.5) is then possible to compute the activity at the moment in which the irradiation was interrupted, and therefore a qualitative evaluation of the thermal flux profile along the channel.

$$A(t) = A(0) \cdot e^{-\frac{\ln(2)}{T_{1/2}} t} \longrightarrow A(0) = A(t) \cdot e^{\frac{\ln(2)}{T_{1/2}} t} \quad (4.5)$$

The count rates obtained from the gamma spectroscopy at each measurement were then normalized by the length of the respective rod, in order to take into account the geometric discrepancies between the samples.

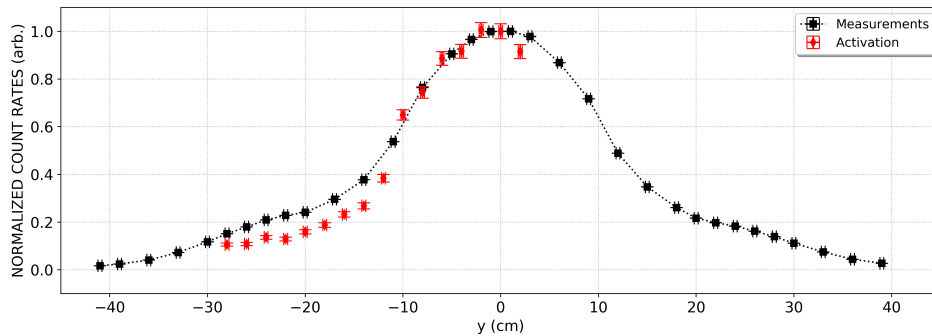


Figure 4.11: Comparison of the activation profile with measurements of miniature detector.

The result of the experiment are shown in in Fig. 4.11, where a substantial disagreement is found between the fiber measurements and the count rates retrieved with the activation technique. The two measured neutron flux distributions differs particularly in the region outside the core, where a discrepancy of about 30% is observed.

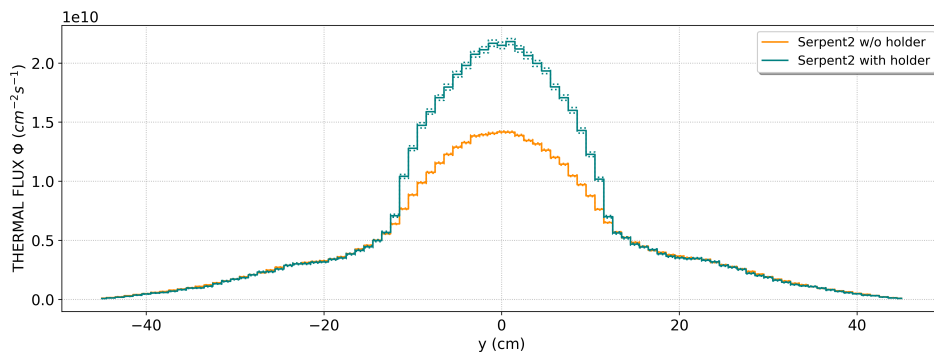


Figure 4.12: Comparison of the simulated results with and without activation holder.

The reason behind this relevant discrepancy is due to the presence of the plastic-graphite holder schematized in Fig. 4.9. The use of the activation holder causes a perturbation in the shape of the neutron flux distribution due to its constituent materials, which increase the thermal neutron flux in the core center. Indeed, the presence of plexiglass enhance the neutron moderation while the graphite promotes the neutrons reflection towards the inner core region. Therefore, if the two flux distributions are plotted by normalizing the measurements for their respective maximum value (as in Fig. 4.11), a meaningless comparison is obtained.

As can be observed in Fig. 4.12, if a comparison without normalization is performed between the neutron flux profiles with and without activation holder, differences up to 50% are recorded. This clearly shows the impact of the activation holder, which dramatically increases the thermal neutron flux for the aforementioned reasons. A fair comparison between the activation measurements and the Serpent2 results cannot be performed without including in the computational model the activation holder. The comparison is shown in Fig. 4.13, where a good agreement is found between experimental and computational data, with C/E-1 values lower than 20% (see Fig. 4.14).

The results of this experiments highlight one of the main drawbacks on the use of the activation technique, i.e. the heavy flux perturbation induced by the holder. Even though this effect could be partially eliminated by means of apposite correction factors, the use of miniature detectors is way preferable if perturbations on measurements wants to be minimized. Indeed, by looking at Fig. 4.8, it is clear that the flux perturbation induced by the miniature detectors is negligible, given the good agreement with Monte Carlo unperturbed results.

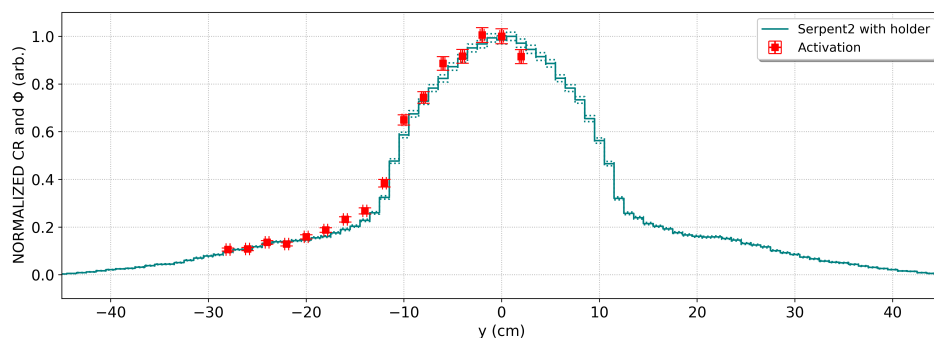


Figure 4.13: Comparison of the activation profile with Serpent2 computed results.

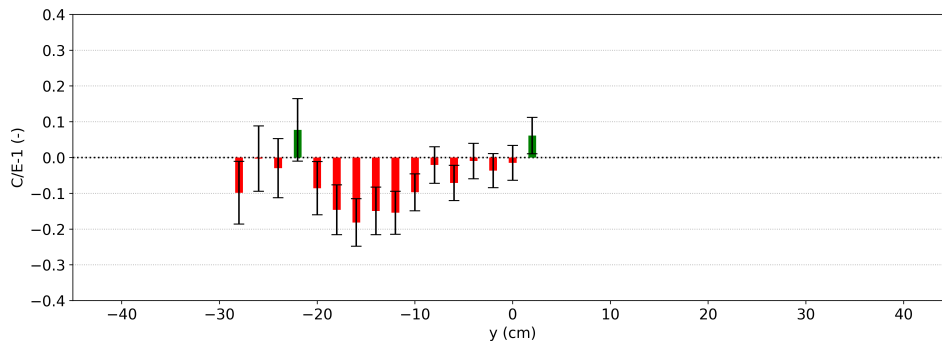


Figure 4.14: $C/E-1$ values for the comparison of the activation profile with Serpent2 computed results.

4.5 Neutron thermal flux profile along channel II

Similarly to the central channel case, also the upper tangential channel is deployed to characterize the thermal neutron flux distribution along its length for the first time. Indeed, no experimental data on the flux distribution were available beforehand, due to the difficulties to perform activation measurements in a region too far from the core center.

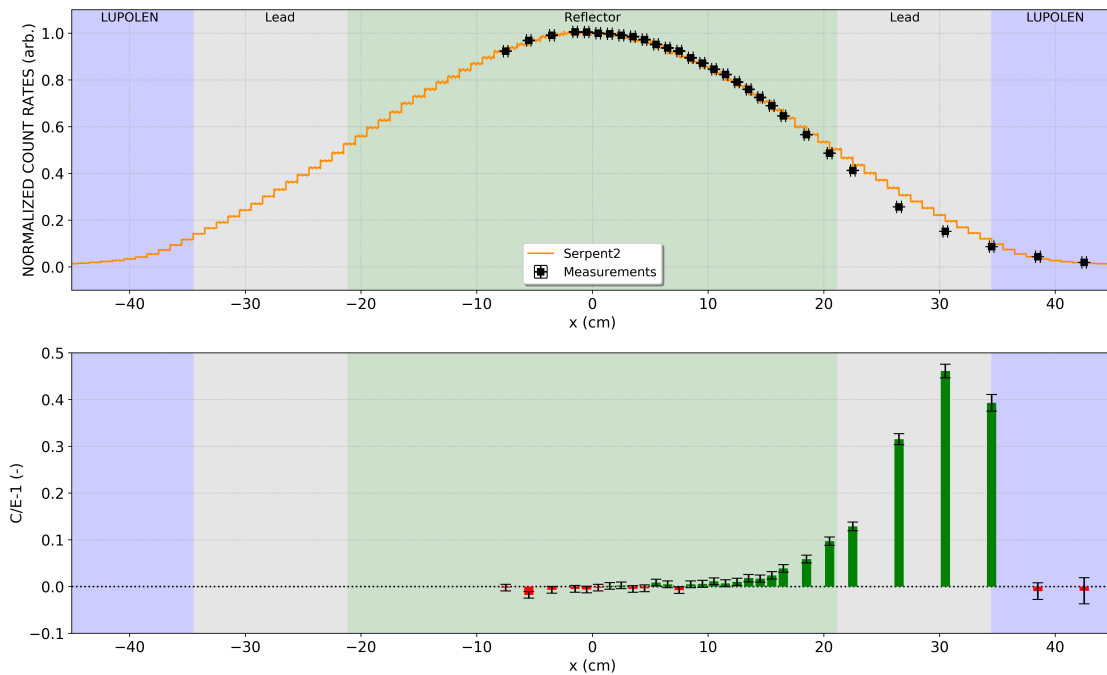


Figure 4.15: Comparison between experimental and simulated results for the thermal neutron flux distribution in tangential channel II.

Again, the miniature detector named “fiber 2” is used as a monitor and it is positioned in the experimental channel I, approximately in correspondence of the core center. The remaining two detectors are configured as shown in Fig. 4.2 (c). A schematic of how the measurement is performed, moving the aluminum tube with the two detectors along the channel, is given in Fig. 4.5. In addition, to fit the holder tube in a channel with larger diameter, opposite ring spacers made out of aluminum are used. The experimental results are shown in Fig. 4.15, together

with a comparison against simulated data. For the Serpent2 simulation, virtual track-length detector of cylindrical dimension as big as the channel (54 mm diameter) are used to characterize the thermal flux profile.

The experimental results show excellent agreement with most of the simulated points, exception made for the data lying in the interval [20;35] cm, where the disagreement reaches values of about 50 %. Again, the discrepancy is localized in the zone occupied by the lead shielding, which can have substantial differences in composition with respect to the modeled one.

Since the data series are normalized for their maximum values (which is located in the core center), the disagreement observed could not necessarily be attributed to the peripheral zones and therefore at the lead shielding region. Nevertheless, the main suspicions fall on the lead shielding area, as it is mechanically and chemically less known than the core center region.

4.6 Vertical gradient in thermal neutron flux across channel I diameter

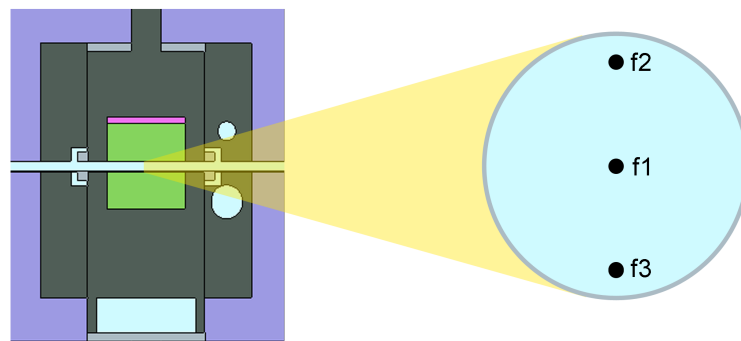


Figure 4.16: Detectors configuration for the vertical gradient measurement.

To assess the existence of a vertical gradient in neutron thermal flux within the experimental channel I, measurements are conducted. The interest of the experiment was directed to understand if the miniature detectors could capture the gradient in count rate at different axial positions in the central experimental channel. For the experiment, the detectors are positioned in the center of the channel according to the configuration (a) of Fig. 4.2 and then rotated of 180° to repeat the measurement (see Fig. 4.16). Only the data from the fiber 2 are used for this experiment, in order to avoid differences in count rates caused by the use of a different detector. For the power normalization, fiber 1 is used as a monitor, since its position remains unchanged even after the 180° rotation.

A Monte Carlo simulation was run after the measurements. A set of 52 virtual track-length detector are modeled along the vertical diameter of the experimental channel, with a y-length of 2 cm. The reaction rate of the scintillator screens with incoming neutrons is predicted by the simulation, with a certain level of approximation caused by the smearing of the real-size detectors on larger volumes for computational cost reasons. As it is seen in Fig. 4.17, the experimental data fall in the range of uncertainty of the simulated result. Both the results suggest for the absence of an axial gradient inside the experimental channel, being the reaction rate distribution almost flat. The oscillation of the reaction rate distribution computed with Serpent2 are not physical, but due to the low statistics of the results. Given the small spatial scale of the

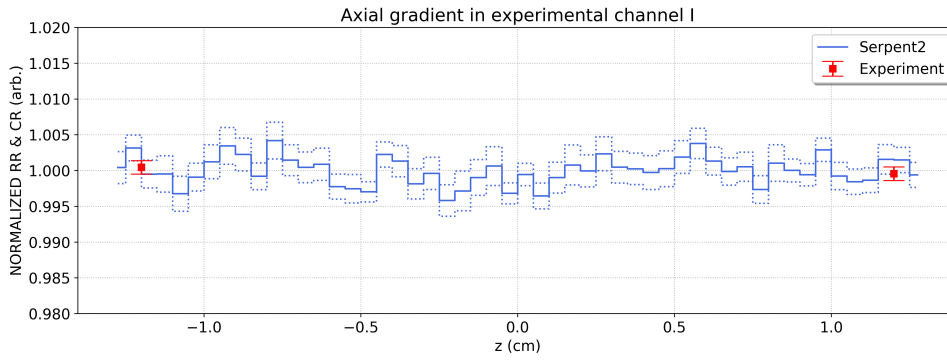


Figure 4.17: Simulated and experimental data for axial reaction rate gradient in experimental channel I.

modeled detectors, having simulated results with better statistic would be challenging with the computational resources used for the work at hand.

4.7 Radial gradient in thermal neutron flux across channel II diameter

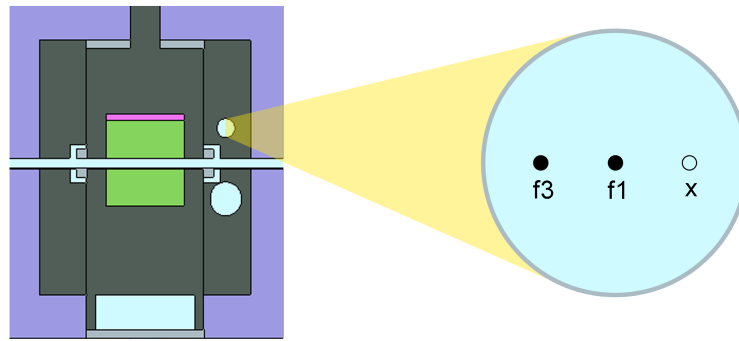


Figure 4.18: Detectors configuration for the radial gradient measurement.

To verify the presence of a gradient across the horizontal diameter of the experimental channel II, a set of measurements is carried out. To perform the measurements, the aluminum holding tube was inserted in the spacers rings to make its diameter suitable to the one of the experimental channel I, and then introduced inside the channel at the position identified with $x=-9$ cm (see Fig. 4.5). The holder was positioned before in the configuration (c) of Fig. 4.2, with fiber 3 towards the core center (see Fig. 4.18), and then it was rotated of 180° in order to have the third detector as far as possible from the core center. The fiber 2 was inserted in the center of the experimental channel I to be used as a power monitor.

The two measurements are performed for a time long enough to ensure a relative error on the count rate in the order of 0.1%. The experiment show the existence of a gradient of $(9.09 \pm 0.20)\%$ from the innermost to the outermost radial position measured with the miniature detectors. The experimental data are then compared with simulated results obtained through a Serpent2 calculation. For the simulation, 54 track-length virtual detectors are used. They were shaped as cylinders with the diameters along the y-direction and a x-thickness of 1 cm (see Fig. 4.5). Both experimental and simulated results are plotted together in Fig. 4.19 after the normalization by their respective mean value. Even though the experimental data are not included within the uncertainties of the simulated results, a similar steepness of the gradient is

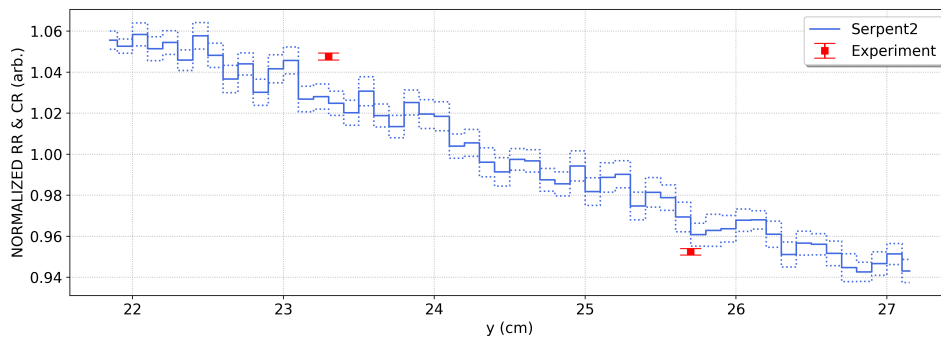


Figure 4.19: Simulated and experimental data for radial reaction rate gradient in experimental channel II.

predicted by Serpent2, with a C/E-1 in the order of 1%. The reason of this discrepancy could be explained by the smearing of the detector volume in the Serpent2 calculations, which is done to decrease the computational cost of the simulations. Such an approximation leads to results averaged over the whole volume of the virtual detector, which are only representative of the exact value recorded by the real-size detector during the measurements.

4.8 Control plate calibration

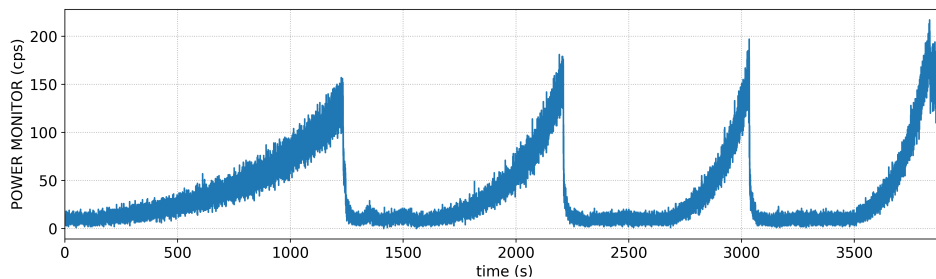


Figure 4.20: Counts recorded by fiber 2 during the reactor periods experiment. The detector is maintained in the center of channel II and used as a power monitor.

With the objective of testing the dynamic acquisition capabilities of the miniature detectors, experiments are carried over to study the reactivity insertion consequent to the extraction of the control plate 2 from the reactor. The power evolution of the SUR 100 reactor, as recorded by the miniature fiber coupled detector, is analyzed for different super-critical configurations. With this study, the reactivity insertion caused by the removal of the control plate 2 is characterized by means of the method of stable positive reactor period measurement.

The experiment is conducted by ramping the power of the SUR 100 reactor from a low-power critical level (~ 20 mW) to a power of about 180 mW by extracting the control plate 2. The power ramp, as shown in the power history recorded by the fiber 2 in Fig. 4.20, was repeated four times with increasing displacements of the Cadmium control plate. Given the critical configuration of the reactor on the experiment day, i.e. CP1 completely extracted (-249 mm) and CP2 at -201 mm, a maximum extraction of 34 mm is allowed to increase the reactor power. The configurations used to insert reactivity for the sake of the experiment at hand are summarized in Tab. 4.1.

Table 4.1: SUR 100 configurations for the reactor periods experiment.

n^o power ramp (-)	Δz_{CP2} (mm)
0	0 (critical)
1	-10
2	-20
3	-30
4	-34

4.8.1 Reactor dynamics

The reactor periods, i.e. the time required for the neutron density to change by a factor e [24], are measured by monitoring the power ramps with the "fiber 2" positioned in the center of the tangential channel II. To measure the stable reactor period, the evolution of neutron population according to the point-kinetics equations (Eq. 4.6 and 4.7) are used.

$$\frac{dn(t)}{dt} = \frac{\rho - \beta}{\Lambda} \cdot n(t) + \sum_{i=1}^6 \lambda_i \cdot C_i \quad (4.6)$$

$$\frac{dC_i(t)}{dt} = \frac{\beta_i}{\Lambda} \cdot n(t) - \lambda_i \cdot C_i(t) \quad (i = 1, \dots, 6) \quad (4.7)$$

with:

n : neutron population;

ρ : reactivity;

β : delayed neutron fraction;

Λ : average effective prompt neutron life-time;

C_i : Concentration of the delayed neutron precursor of the i -th group;

λ_i : Decay constant of the delayed neutron precursor of the i -th group.

Solving the system of equations represented by Eq. 4.6 and 4.7 for the neutron population, leads to a linear combination of 7 solutions corresponding to the 7 eigenvalues ω_i (see Eq. 4.8).

$$n(t) = n_1 \cdot e^{\omega_1 \cdot t} + n_2 \cdot e^{\omega_2 \cdot t} + \dots + n_7 \cdot e^{\omega_7 \cdot t} \quad (4.8)$$

The values of the ω_i are given by the roots of the Inhour Equation:

$$\rho = \Lambda \omega + \sum_{i=1}^6 \frac{\beta_i \omega}{\omega + \lambda_i} \quad (4.9)$$

which for a positive step change in reactivity has just one positive ω value, while all other roots are negative. Thus, the first term of Eq. 4.8 is the only one not decaying with time, while the other ones quickly die due to the negative exponent. Consequently, the growth in power of the reactor is dominated by the exponent ω_1 , which defines the stable reactor period as $T = 1/\omega_1$. The dynamic parameters used in the framework of this experiment, provided by the IKE laboratory, are summarized in Tab. 4.2. The total fraction of delayed neutrons β was assumed to account for 687 pcm, while the average prompt neutron lifetime is taken as $\Lambda = 2.5 \cdot 10^{-5}$ s.

4.8.2 Reactivity computation

The reactivity inserted with the movement of a control plate is determined experimentally through the Inhour equation (Eq. 4.9). Since the knowledge of the inverse stable reactor period

Table 4.2: Kinetic parameters used for the reactivity computations of the SUR 100 reactor.

Delayed group i	Half-life $t_{1/2}$ (s)	Decay constant λ_i (s ⁻¹)	Relative delayed fraction β_i/β (-)
1	55.90	0.0124	0.033
2	22.73	0.0305	0.209
3	6.24	0.111	0.196
4	2.30	0.301	0.395
5	0.61	1.14	0.115
6	0.23	3.01	0.042

ω is needed, it can be retrieved by considering the time-evolution of the neutron population as recorded by the monitor fiber during the experiment. Indeed, if the natural logarithm of the detector counts shown in Fig. 4.20 is plotted in time, the slope of the linear portion of the curve represent the value of ω for each power ramp. In Fig. 4.21 the linear fit used to evaluate the slope of the power ramps are shown together with the computed inverse stable reactor period ω .

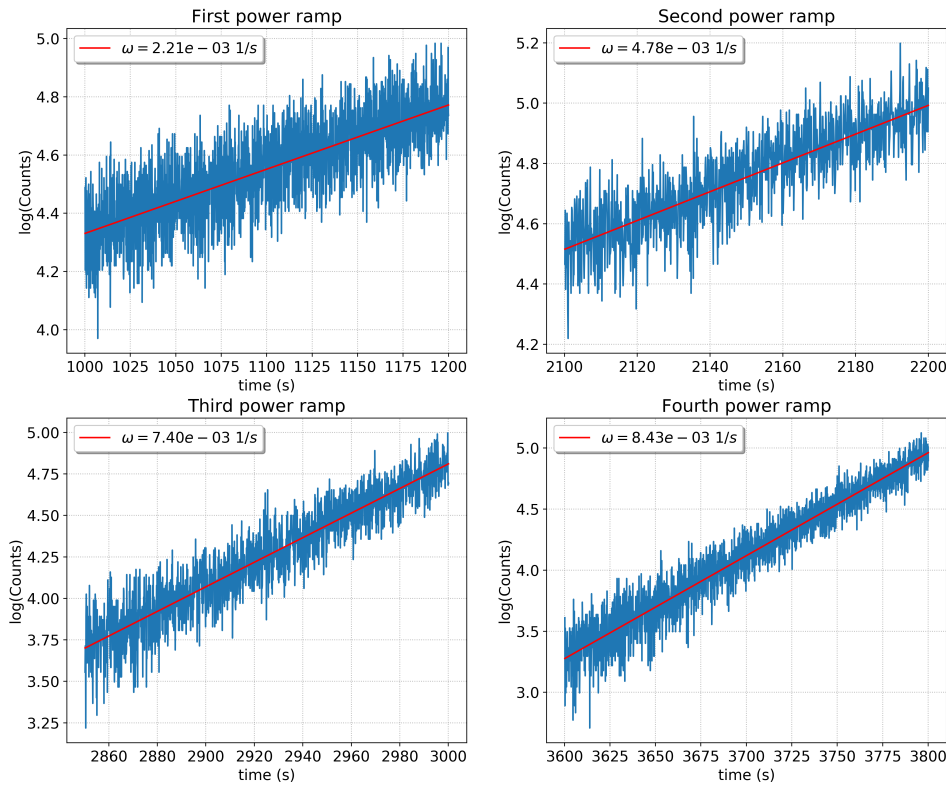


Figure 4.21: Linear fitting of the monitor data for the reactivity experiment.

By knowing the ω values for each power ramp, the corresponding inserted reactivity is computed through the Inhour equation (Eq. 4.9) using the dynamic parameters provided in Tab. 4.2. The experimental results are shown in Tab. 4.3.

Serpent2 simulations are then run to perform a comparison with the experimental data.

Multiple position of the control plate 2 are simulated starting from the critical position. The reactivity is retrieved from the multiplication factor k_{eff} obtained in output from the simulations. The comparison with experimental data is shown in Fig. 4.22. The comparison shows that the experimental data fall within the uncertainty range of the simulated results, demonstrating an overall agreement. Both the data series are normalized by subtracting to each point the reactivity value corresponding to criticality ($\Delta z_{CP2} = 0$).

Table 4.3: Summary table of the reactivity experiment in SUR 100.

CP2 displacement from criticality Δz_{CP2} (mm)	Experimental reactivity ρ (pcm)
-10 ± 1	$+18 \pm 6$
-20 ± 1	$+37 \pm 6$
-30 ± 1	$+53 \pm 5$
-34 ± 1	$+59 \pm 3$

The shape of the reactivity curve is seen to be almost linear, due to the limited displacement available for the removal of control plate 2. Indeed, the CP2 can be used to bring the reactor to a supercritical state only in the last 34 mm of its stroke. Thus, the mild gradient existing in the axial flux profile along 34 mm in the position where the control plate lies does not cause the S-shaped curve, typically produced when an absorbing rod is removed from a reactor core with an axial cosine-shaped flux distribution.

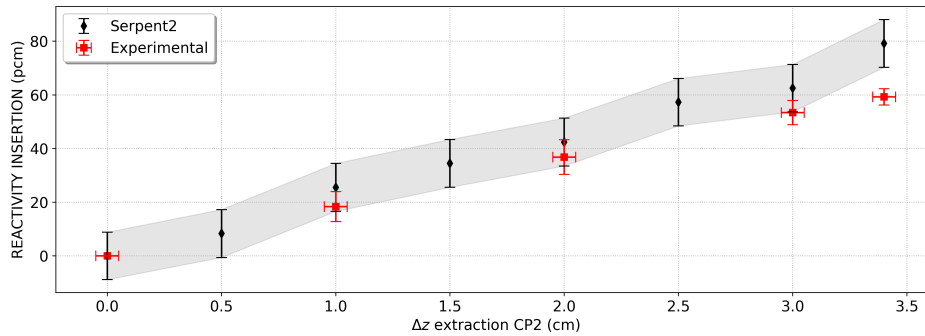


Figure 4.22: Comparison between simulation and experimental data for the control plate 2 reactivity calibration.

5 Conclusions

The main objective of the work carried over in the framework of this master thesis project was the characterization of the thermal neutron flux in experimental channels of the SUR-100 reactor. The task has been accomplished by means of innovative miniature fiber-coupled scintillators, that allowed for a high resolution description of the neutron flux profiles within the experimental channels of the reactor.

The experiments carried out on the SUR 100 reactor gave further proof of the good acquisition capabilities of the miniature detectors, that were tested before only in the CROCUS facility, at EPFL. The use of miniature detectors demonstrated multiple advantages in the flux profile characterization over the previously used activation techniques, eliminating the flux perturbation caused by the holder of the activation samples and enhancing the spatial discretization of the measurements. For the present work the detectors demonstrated their capability to capture very localized reaction rate gradients with innovative arrangements. A reaction rate gradient of $(9.09 \pm 0.20)\%$ is measured between the two extremities of the horizontal diameter of the experimental channel II. The miniature detectors proved also their goodness in describing dynamic phenomena, highlighting their potentiality to be used to monitor the power evolution of an experimental reactor.

In the context of this thesis, a preexisting MCNP model of SUR 100 was successfully converted and enhanced to be run with the particle transport code Serpent2. Before and after the experimental campaign, the use of Monte Carlo calculations has been paramount for the work at hand. During the planning phase of the campaign, preparatory simulations were run to evaluate the feasibility of the experiments. Once the campaign was carried over, the calculations were adapted to the real measurement conditions and repeated to be compared with the experimental results.

An overall good agreement has been found between the computational results produced by the converted Serpent2 model and the experimental data. For the reaction rates distributions along the experimental channels, C/E-1 values lower than 10% are obtained for most of the points. Some discrepancies are found to exist between the experimental data and the results produced by simulations in specific zones of the reactor. To solve these inconsistencies, mainly localized in the zone of the lead shielding of the reactor, further investigations on the level of approximation used for the Serpent2 model of SUR 100 are needed. In particular, additional information on the real composition of the materials and a better knowledge on the inner geometry of the reactor would be necessary to achieve more accurate results.

Future experiments are planned to fully explore the potentialities of the miniature detectors. In light of the demonstrated capabilities in capturing dynamic evolution of count rates on

a small spatial scale, further investigations on 3D neutron flux perturbations will be conducted in CROCUS with the use of multiple parallelized fiber-coupled detectors.

Appendices

A Radiation safety assessment

Evaluating the entity and the amount of radiations delivered in the surroundings of any nuclear reactor is fundamental to ensure the safety of the working personnel. In the present work, a rough estimation of the neutron and gamma dose rate delivery in the zone close to the concrete shielding of the reactor is made through Serpent2 calculations. The results are then compared with limits imposed by the regulatory authorities to assess whether they are exceeded or not.

A.1 Simulation setup

A set of Serpent2 calculations are run for the study at hand, using virtual detectors to tally the neutron and the gamma radiation outside the concrete shielding. The simulations have been carried over under a geometrical hypothesis concerning the concrete shielding. In fact, even though the SUR 100 reactor has an octagonal shielding, for simplicity in the simulations it has been modeled with a cylindrical shape. Despite relevant, this assumption is accepted given the nature of the study, which do not aim to obtain absolute results but only order of magnitude of the dose rate delivered by the neutrons and gamma radiation.

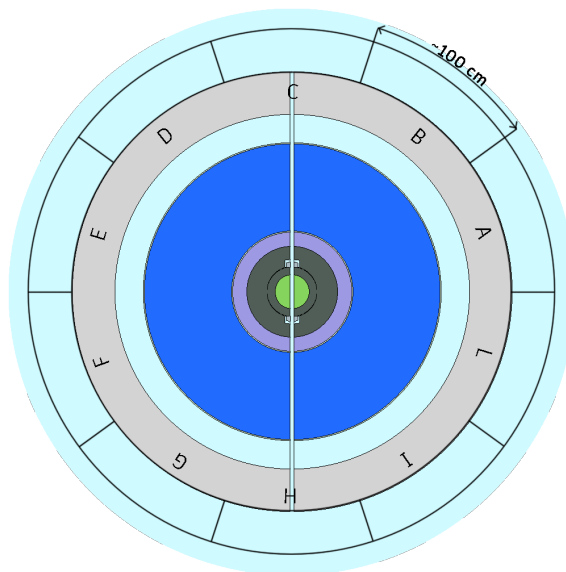


Figure A.1: Virtual detectors used for the dose rate assessment.

The virtual detectors used for the calculations consist of 10 segments of circular corona, as it is shown in Fig. A.1. With a height of 200 cm, they are chosen to be of anthropomorphic size, to simulate the presence of a human being very close to the concrete shielding of the reactor. The

virtual detectors are identified with an alphabetic character from A to L in a counter-clockwise direction.

A.2 Neutrons dose rate

The computation of the neutron dose rate delivered outside the reactor shielding is performed in two stages. A first stage consists in the computation of the neutron flux distribution around the reactor shielding, to assess which zone is the highest affected by neutron radiation. The second stage consists in the computation of the neutron dose rate through apposite flux-to-dose-rate conversion factors. The first stage, is carried over by using a variance reduction method for the neutron transport described in the following paragraph.

Weight window technique Weight window techniques are part of the variance reduction method used to increase Monte Carlo calculations efficiency. They are often used for shielding computations, where it can be very difficult to obtain accurate results with the standard method because of the relevant computational cost. The low efficiency of the standard method is indeed caused by the difficult penetration of the particles in depth through the geometrical surfaces meant to be shielding them.

This variance reduction technique, consists in dividing the domain of the simulation in several regions and in assigning them an importance accordingly to the aim of the calculation. In the calculation at hand, since the focus is shifted on the neutron flux computation around the concrete shielding, the highest-important zones are the ones corresponding to the detectors zones of Fig. A.1. Fig. A.2 shows the importance mesh used for the calculations, where the orange area correspond to a higher importance zone. The highest importance region is here in the zone of the virtual detectors, right outside of the concrete shielding. A detailed description of the method and on how the importance is computed by Serpent2 is outside of the scope of the work at hand, and it is provided in [25].

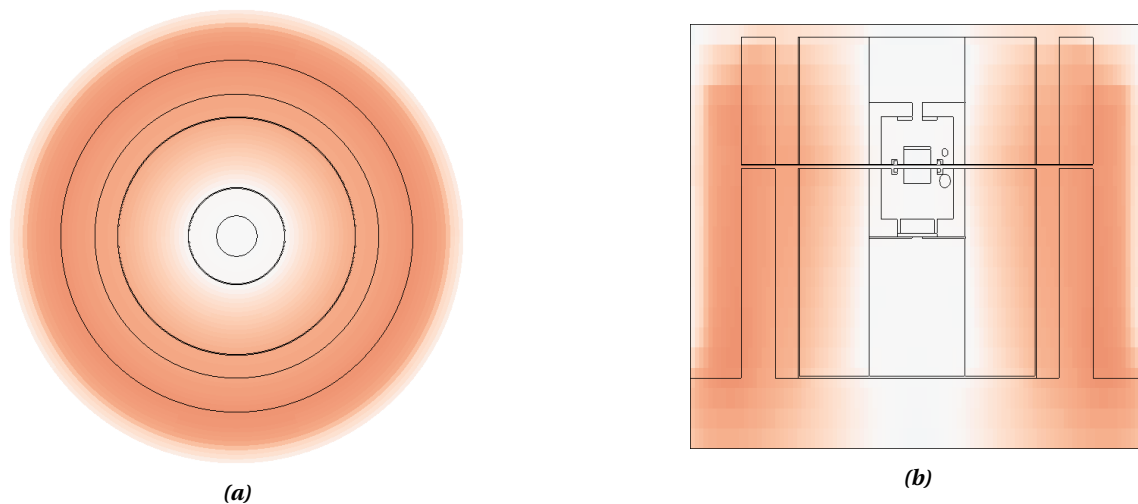


Figure A.2: Horizontal (a) and vertical (b) view of the importance mesh used for the calculations.

Neutron flux distribution The variance reduction technique described in the previous paragraph allowed to obtain an angular distribution of the neutron flux, both thermal and fast, around the reactor shielding. In Fig. A.3 are depicted the results of the calculation.

As expected, the neutron flux has two peaks in the zone directly facing the experimental channel I, namely zone “C” and zone “H”. These peaks are caused by the neutrons leakage



Figure A.3: Neutron flux distribution around the reactor concrete shielding.

through the central experimental channel, which occurs because of the presence of air as a filling material. Being the flux proportional to the delivered neutron dose, these two zones will be the most affected ones by neutron radiation.

Dose rate conversion factor To convert the angular neutron flux distribution in a dose rate angular distribution conversion factors from a previous work are used [26]. The factors used for the conversion, which are shown in Fig. A.4, are given as a function of the neutrons energy. For the sake of simplicity, two single values ($1 \cdot 10^{-11}$ and $6 \cdot 10^{-10}$) are selected to convert the thermal and the fast neutron flux into dose rates.

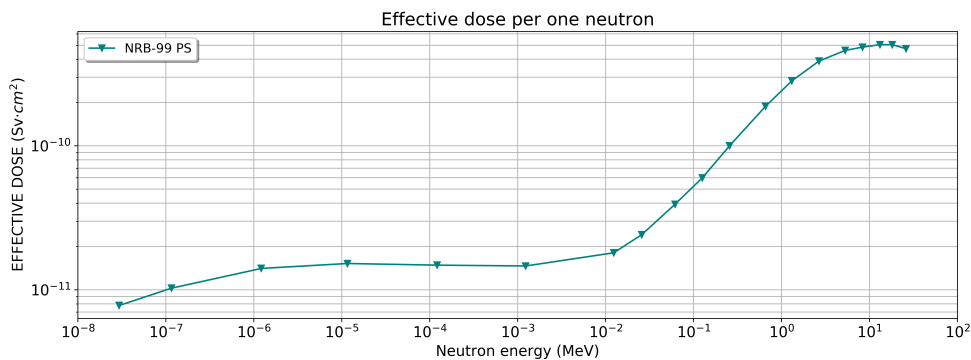


Figure A.4: Neutron flux to dose rate conversion factors [26]

Under the hypothesis of homogeneous irradiation all over the human body, the tissue weighting factor is assumed to be equal to 1, i.e. the effective and the equivalent dose are equal.

A.3 Gamma dose rate

The dose rate delivered from the gamma radiation outside the reactor shielding is computed with a photon-transport simulation run with Serpent2. ENDF/B-VI [27] has been used as cross section library for photoatomic data.

Unlike the neutron dose rate case, the gamma dose rate distribution is computed in a one-

step process. The same virtual detectors depicted in Fig. A.1 are used in the simulations, with an apposite response function to automatically convert the scored photons interactions into gamma dose rates. Therefore the gamma dose rate distribution is retrieved without the need of conversion factors, as the conversion itself has been performed through Serpent2.

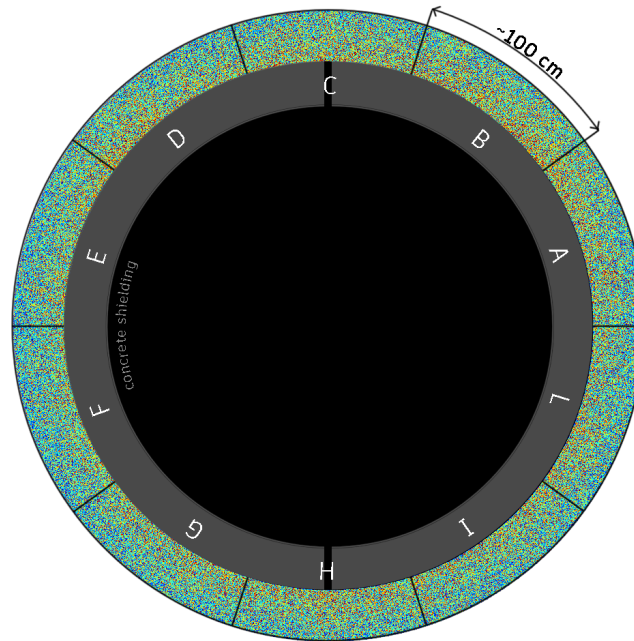


Figure A.5: Mesh plot for the Gamma dose rate distribution around the shielding of SUR 100.

The result of the computation (see Fig. A.5) is represented with a so-called mesh plot, which shows the intensity of the gamma dose rate spatially around the reactor. As can be noticed, the gamma radiation does not peak in specific zones, but it is homogeneously distributed azimuthally. This is caused by the higher penetration depth of the gamma radiation with respect to the neutrons, which are much more heavily shielded by the materials of SUR 100.

A.4 Results

By summing the results for the neutron dose rate and the gamma dose rate distribution, the total dose rate distribution around SUR 100 is obtained.

The results, depicted in Fig. A.6, show a delivered dose rate of $1.50 \mu\text{Sv/h}$ all around SUR 100, with peaks in the zone of the accesses of the experimental channel 1 caused by the neutrons leakage. The dose rate caused by the gamma-radiation, which accounts for the majority in the total dose rate distribution, is instead constant all around the concrete shielding.

In Fig. A.7 the results of the simulations are compared with the everyday exposure of a civil U.S. citizen provided by EPA [28] and with the exposure limit for workers given by NRC [29]. The comparison shows that the radiation is safely below the critical limit for workers in the nuclear field, being it around 30% of the maximum allowed dose rate. Nevertheless, the radiation is still relevant, being it twice the everyday exposure for a civil inhabitant of the United States.

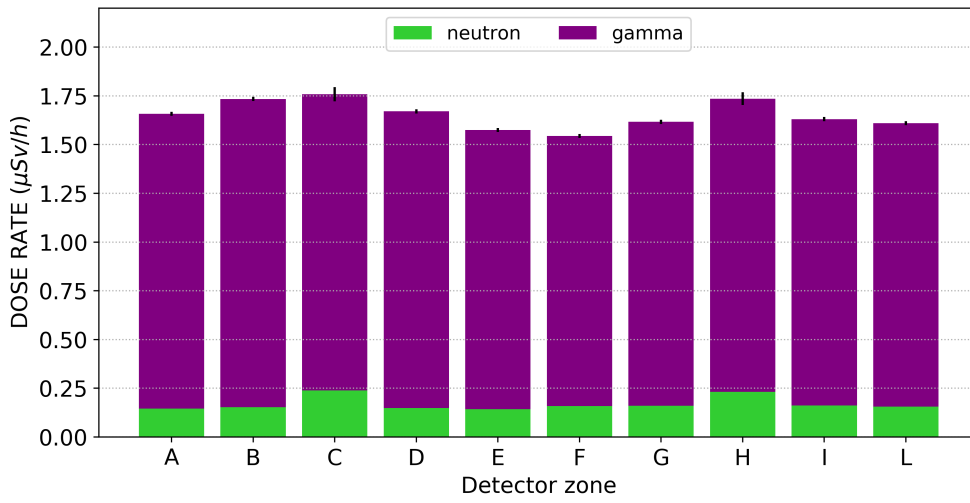


Figure A.6: Dose rate distribution around SUR 100.

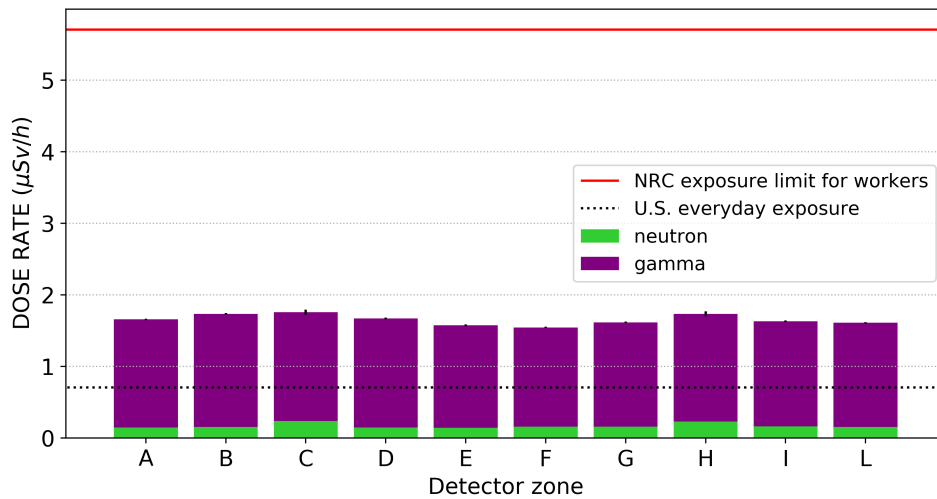


Figure A.7: Dose rate distribution around SUR 100 compared with legal limits.

B Serpent2 SUR 100 model

By way of example, it is hereafter shown the Serpent2 script used to model the SUR 100 reactor for the computational simulations. The model is here reported in his simplest configuration, without the addition of nuclear instrumentation or virtual detectors.

```
% SUR 100 - Serpent2 model
% Author : E.L.Brunetto
%*****
set title "SUR100"
%*****
% --- SUMMARY:
% | 1. XS libraries      | 2. Materials definition | 3. Surfaces definition |
% | 4. Cells definition | 5. Transformation cards | 6. Run parameters     |
% | 7. Plots            |
%*****
% --- 1. Cross section libraries:
set acelib "/sss_endfb7u.xsdata"      % endfb7
therm poly HCH2.71t                   % TSL polyethylene
therm grph gre6.00t                   % TSL graphite
%*****
% --- 2. Materials definition:
% m0 : Air
mat m0 -1.225e-3      rgb 207 250 255
  6000.03c      0.015 % C
  7014.03c      78.437 % N
  8016.03c      21.076 % O
  18040.03c     0.472 % Ar
% m1 : Core (1.23548 g/cm3)
mat m1 -1.23548      rgb 133 212 93 moder poly 1001
  1001.03c 7.9151e-2 % H
  6000.03c 3.9575771e-2 % C
  92235.03c 1.53728e-4 % U-235
  92238.03c 6.071447e-4 % U-238
  8016.03c 2.0289947e-3 % O
% m2 : Graphite (1.65 g/cm3)
mat m2 -1.65      rgb 80 94 87      moder grph 6000
  6000.03c 8.26307E-02 % C nat 100.000
  3006.03c 5.36843E-09 % Li 6 7.500 2
  3007.03c 6.62107E-08 % Li 7 92.500 2
  5010.03c 4.57257E-07 % B 10 19.900 2
  5011.03c 1.84052E-07 % B 11 80.100 2
  13027.03c 7.36543E-07 % Al 27 100.000 1
  20000.03c 1.23965E-05 % Ca nat 100.000
  22000.03c 2.07537E-06 % Ti nat 100.000
  26054.03c 2.07999E-08 % Fe 54 5.845 4
```

26056.03c	3.26514E-07	% Fe 56	91.754	4	42
26057.03c	7.54064E-09	% Fe 57	2.119	4	43
26058.03c	1.00352E-09	% Fe 58	0.282	4	44
23000.03c	1.46293E-06	% V nat	100.000		45
1001.03c	4.92821E-06	% H 1	99.985	2	46
% m3 : Aluminium					47
mat m3	-2.7	rgb 171 187 196			48
13027.03c	6.0265E-2	% Al 27			49
14028.03c	1.25E-4	% Si			50
26056.03c	1.1e-4	% Fe 56			51
5010.03c	2.e-7	% B 10			52
% m4 : Cadmium					53
mat m4	-8.65	rgb 255 233 33			54
48110.03c	12.49	% Cd 110			55
48111.03c	12.8	% Cd 111			56
48112.03c	24.13	% Cd 112			57
48113.03c	12.22	% Cd 113			58
48114.03c	28.73	% Cd 114			59
48116.03c	7.49	% Cd 116			60
% m6 : Boron rich plastic granulate					61
mat m6	-0.7	rgb 33 107 255			62
1001.03c	4.749092e-2	% H			63
6000.03c	2.374546e-2	% C			64
5010.03c	2.483006e-4	% B 10			65
5011.03c	9.932024e-4	% B 11			66
8016.03c	1.862255e-3	% O 16			67
% m7 : Lead					68
mat m7	-11.4	rgb 157 154 227			69
82206.03c	24.1	% Pb 206			70
82207.03c	22.1	% Pb 207			71
82208.03c	52.4	% Pb 208			72
% m8 : Stainless Steel :					73
mat m8	-7.8	rgb 218 240 211			74
% Fe density 6.0336642E-02					75
26054.03c	3.5598618E-03				76
26056.03c	5.5340771E-02				77
26057.03c	1.2670695E-03				78
26058.03c	1.6894258E-04				79
% Cr density 1.7428214E-02					80
24050.03c	7.5725594E-04				81
24052.03c	1.4603100E-02				82
24053.03c	1.6556802E-03				83
24054.03c	4.1217727E-04				84
% Ni density 8.1132147E-03					85
28058.03c	5.5232332E-03				86
28060.03c	2.1275284E-03				87
28061.03c	9.2490649E-05				88
28062.03c	2.9483420E-04				89
28064.03c	7.5128366E-05				90
% Mn density 1.6250288E-03					91
25055.03c	1.6250288E-03				92
% m9 : PE (Polyethylene)					93
mat m9	-0.92	rgb 240 115 240 moder poly	1001		94
1001.03c	2	% H			95
6000.03c	1	% C			96
% m11 : Regular concrete					97
mat m11	-2.3	rgb 211 211 211			98
1001.03c	1.68038E-01	% H			99
8016.03c	5.63183E-01	% O			100
11023.03c	2.13650E-02	% Na			101
13027.03c	2.13430E-02	% Al			102
14028.03c	2.03231E-01	% Si			103
20040.03c	1.85950E-02	% Ca			104

26056.03c	4.24600E-03 % Fe		105
%*****			106
% --- 3. Surfaces definition:			107
surf core		cylz 0.0 0.0 12.0 -12.0 12.2	108
surf core_up		cylz 0.0 0.0 12.0 0.0 12.2	109
surf core_low		cylz 0.0 0.0 12.0 -12.0 0.0	110
surf aa		cyly 0.0 0.0 1.50	111
surf 10I_out		cyly 0.0 0.0 1.50	112
surf 10I_in		cyly 0.0 0.0 1.30	113
surf core_bott		pz -12.0	114
surf inn_mov		cylz 0.0 0.0 12.0 -37.0 -12.0	115
surf plate_PE		cylz 0.0 0.0 12.0 12.2 14.0	116
surf top_plate_PE		pz 14.0	117
surf vess_in		cylz 0.0 0.0 17.5 -47.0 32.5	118
surf vess_out		cylz 0.0 0.0 17.8 -49.5 35.0	119
surf 10IV_out		cylz 0.0 0.0 4.55	120
surf 10IV_in		cylz 0.0 0.0 4.35	121
surf vess_bott		pz -49.5	122
surf vess_bott_in		pz -47.0	123
surf fla_outy		cyly 0.0 0.0 4.00	124
surf fla_outz		cylz 0.0 0.0 20.8	125
surf rec_outy		cyly 0.0 0.0 5.40	126
surf rec_outz		cylz 0.0 0.0 22.7	127
surf cavity		cylz 0.0 0.0 15.0 -47.0 -37.0	128
surf tank_out		cylz 0.0 0.0 105.0 -148.8 91.2	129
surf tank_in		cylz 0.0 0.0 104.2 -147.3 91.2	130
surf tank_B		cylz 0.0 0.0 42.8 -147.3 91.2	131
surf tank_a		cylz 0.0 0.0 42.0	132
surf splate_bott		pz -50.5	133
surf splate_top		pz -49.5	134
surf lead_top		pz 45.0	135
surf top		pz 91.2	136
surf 10II		cylx 24.5 10.0 2.7	137
surf 10III		cylx 24.5 -10.0 4.8	138
surf lead_in		cylz 0.0 0.0 32.0 -37.0 35.0	139
surf lead_out		cylz 0.0 0.0 42.0 -49.5 45.0	140
surf CPL		cuboid -18.2 -17.9 -12.5 12.5 -14.5 14.5	141
surf CPR		cuboid 17.9 18.2 -12.5 12.5 -14.5 14.5	142
surf conc_in		cylz 0.0 0.0 125.0 -148.8 91.2	143
surf conc_out		cylz 0.0 0.0 155.0 -148.8 91.2	144
surf floor		pz -148.8	145
surf boundary		cylz 0.0 0.0 160.0 -198.8 100	146
%*****			147
% --- 4. Cells definition:			148
cell clup	0	m1 -core_up #c1low 10I_out	149
cell c1low	0	m1 -core_low 10I_out aa	150
cell c2	0	m3 -vess_out vess_in 10I_out 10IV_out :	151
		-vess_bott_in vess_bott -10IV_out	152
cell c3	0	m9 -plate_PE	153
cell c4	0	m3 -fla_outz vess_out -fla_outy 10I_out	154
cell c5	0	m0 -rec_outz vess_out -rec_outy 10I_out #c4	155
cell c6	0	m8 -tank_B tank_a 10I_out #c12 #c13 :	156
		-splate_top splate_bott -tank_a 10IV_out vess_out :	157
		-tank_out tank_in 10I_out #c12 #c13	158
cell c7	0	m2 -10IV_in top_plate_PE -top	159
cell c8	0	m2 -tank_a lead_top -top 10IV_out	160
cell c9	0	m0 -cavity inn_mov	161
cell c10	0	m0 -tank_a -splate_bott -tank_in :	162
		-10IV_out -vess_bott splate_bott	163
cell c11	0	m2 -inn_mov : inn_mov cavity -vess_in core 10I_out	164
		plate_PE 10IV_out core_low	165
cell c12	0	m0 -10II -conc_out	166

```

cell c13      0      m0      -10III -conc_out      167
cell c14      0      m2      -lead_in 10I_out 10II 10III rec_outz :      168
                                rec_outy vess_out -lead_in -rec_outz 10II 10III      169
                                #c21 #c22      170
cell c15      0      m7      -lead_out lead_in vess_out 10IV_out 10I_out      10II      171
                                10III CPR CPL      172
cell c16      0      m6      -tank_in tank_B 10I_out 10II 10III      173
cell c17      0      m0      -10I_in -conc_out      174
cell c18      0      m3      -10I_out 10I_in -conc_out      175
cell c19      0      m3      -10IV_out 10IV_in -top top_plate_PE      176
cell c20      0      m0      -conc_in tank_out 10I_out #c12 #c13 : -boundary      177
                                conc_out floor      178
cell c21      0      m4      -CPR      179
cell c22      0      m4      -CPL      180
cell c26      0      m11     -conc_out conc_in 10I_out #c12 #c13 : -floor -boundary      181
cell c28      0      outside boundary      182
%*****      183
% --- 5. Transformation cards:      184
% control plates:      185
trans S CPL 0.0 0.0 -20.1      186
trans S CPR 0.0 0.0 -24.9      187
% lower core section:      188
trans S core_low 0.0 0.0 0      189
trans S inn_mov 0.0 0.0 0      190
trans S aa      0.0 0.0 0      191
%*****      192
% --- 6. Run parameters:      193
% boundary conditions:      194
set bc 1 % (1 = black, 2 = reflective, 3 = periodic)      195
% k-eigenvalue criticality source mode:      196
set pop      197
20000 % source neutrons per cycle      198
1000 % active cycles      199
150 % inactive cycles      200
set power 0.1 % source rate normalization      201
set outp 10 % cycles print interval      202
%*****      203
% --- 7. Plots      204
plot 1 1000 1000      205
plot 2 1000 1000      206
plot 3 1000 1000      207
plot 3 1000 1000 0.0 -50 +50 -50 +50 % channel I      208
plot 3 1000 1000 +10 -50 +50 -50 +50 % channel II      209
plot 3 1000 1000 -10 -50 +50 -50 +50 % channel III      210

```

Bibliography

- [1] H. Von Gunter and E. Schwartz. *Siemens-Unterrichts-Reaktor SUR Part 2: Reactor description*. Tech. rep. Siemens-schuckertwerke aktiengesellschaft, 1963.
- [2] F. Vitullo et al. “A mm3 Fiber-Coupled Scintillator for In-Core Thermal Neutron Detection in CROCUS”. In: *IEEE Transactions on Nuclear Science* 67.4 (Apr. 2020), pp. 625–635. ISSN: 15581578. DOI: 10.1109/TNS.2020.2977530.
- [3] F. Vitullo et al. “Highly Localized Azimuthal Measurements in the Crocus Reactor Towards the Validation of High-Fidelity Neutronics Codes”. In: *Physor 2020: Transition to a Scalable Nuclear Future* (2020).
- [4] C. J. Werner et al. *MCNP Version 6.2 Release Notes*. Tech. rep. Los Alamos National Laboratories, 2018.
- [5] J. Leppänen et al. “The Serpent Monte Carlo code: Status, development and applications in 2013”. In: *Annals of Nuclear Energy* 82 (2015), pp. 142–150. ISSN: 18732100. DOI: 10.1016/j.anucene.2014.08.024.
- [6] IKE-Laboratory. *Technological data of SUR-100 reactor*. Tech. rep. IKE laboratory, 2020.
- [7] F. Vitullo et al. “Developing and testing a miniature fiber-coupled scintillator for in-core neutron counting in CROCUS”. In: *EPJ Web of Conferences* 225 (2020), p. 04018. DOI: 10.1051/epjconf/202022504018.
- [8] Scintacor. *Neutron Screens*. Tech. rep. 2016. URL: www.scintacor.com.
- [9] M. B. Chadwick et al. “ENDF/B-VII.0: Next Generation Evaluated Nuclear Data Library for Nuclear Science and Technology”. In: *Nuclear Data Sheets* 107.12 (Dec. 2006), pp. 2931–3060. ISSN: 00903752. DOI: 10.1016/j.nds.2006.11.001.
- [10] Eska. *Industrial Fiber Optics*. 2020. URL: <https://i-fiberoptics.com/eska-fiber-cable.php>.
- [11] Saint-Gobain. “Safety data sheet BC-630 Silicone Grease”. In: 2008.1272 (2017), pp. 1–10. URL: <https://www.crystals.saint-gobain.com/sites/imdf.crystals.com/files/documents/bc-630.pdf>.
- [12] G. F. Knoll and H. W. Kraner. *Radiation Detection and Measurement*. Vol. 69. 4. 1981, p. 495. ISBN: 9780470131480. DOI: 10.1109/PROC.1981.12016.
- [13] Hamamatsu. *MPPC (SiPM) S13360-2050VE*. 2020. URL: <https://www.hamamatsu.com/eu/en/product/type/S13360-2050VE/index.html>.
- [14] J. Leppänen. *Serpent - A Monte Carlo Reactor Physics Burnup Calculation Code*. URL: <http://montecarlo.vtt.fi/>.
- [15] R.J. Mcconn et al. *Compendium of Material Composition Data for Radiation Transport Modeling*. Tech. rep. Pacific Northwest National Laboratory, 2011.

- [16] G. Kpisty and J. Cetnar. “Dominance ratio evolution in large thermal reactors”. In: *Annals of Nuclear Energy* (2017). ISSN: 18732100. DOI: 10.1016/j.anucene.2016.11.046.
- [17] F. B. Brown. “On the use of shannon entropy of the fission distribution for assessing convergence of Monte Carlo criticality calculations”. In: *PHYSOR-2006 - American Nuclear Society's Topical Meeting on Reactor Physics 2006* (2006).
- [18] A. Santamarina et al. *The JEFF-3.1.1 Nuclear Data Library Validation Results from JEF-2.2 to JEFF-3.1.1*. Nuclear Energy Agency Organisation for Economic Co-operation and Development, 2009. ISBN: 978-92-64-99074-6. URL: [www.nea.fr/html/dbdata/nds_jefreports/..](http://www.nea.fr/html/dbdata/nds_jefreports/)
- [19] Nuclear Energy Agency. *JEFF-3.2 Evaluated Data Library - Neutron data*. 2014. URL: https://www.oecd-nea.org/dbforms/data/eva/evatapex/jeff_32/.
- [20] CAEN. *V2495 - Tools for Discovery*. URL: <https://www.caen.it/products/v2495/>.
- [21] V. Lamirand et al. “Power calibration methodology at the CROCUS reactor”. In: *EPJ Web of Conferences* 225 (2020), p. 04022. DOI: 10.1051/epjconf/202022504022.
- [22] R. Pietra. *Neutron activation analysis of aluminum - Determination of gamma-emitting impurities with long half lives*. Tech. rep. Euratom, 1963.
- [23] M.D. Glascock. “Comparison and contrast between XRF and NAA: Used for characterization of obsidian sources in central Mexico”. In: *X-Ray Fluorescence Spectrometry (XRF) in Geoarchaeology*. Springer New York, 2011, pp. 161–192. ISBN: 9781441968852. DOI: 10.1007/978-1-4419-6886-9{_}8.
- [24] N. Connor. *Reactor Period*. 2019. URL: <https://www.reactor-physics.com/what-is-reactor-period-definition/>.
- [25] I. Lux and L. Koblinger. *Monte Carlo Particle Transport Methods: Neutron and Photon Calculations*. 2018. ISBN: 0849360749. DOI: 10.1201/9781351074834.
- [26] N. Xoubi. “Neutrons and gamma-ray dose calculations in subcritical reactor facility using MCNP”. In: *Atoms* 4.3 (2016). ISSN: 22182004. DOI: 10.3390/atoms4030020.
- [27] H. D. Lemmel. *Documentation series of the IAEA nuclear data section*. Tech. rep. International Atomic Energy Agency, 2002.
- [28] United States Environmental Protection Agency. *Radiation Sources and Doses*. URL: <https://www.epa.gov/radiation/radiation-sources-and-doses>.
- [29] Nuclear Regulatory Commission. *Information for Radiation Workers*. URL: <https://www.nrc.gov/about-nrc/radiation/health-effects/info.html>.